Studies on Designing and Optimization of Hot and Cold Deformation Process for a Two Phase Zr Based Alloy

By

N. SAIBABA

(ENGG0120094003)

Bhabha Atomic Research Centre

A thesis submitted to the
Board of Studies in Engineering Sciences
In partial fulfillment of requirements
for the Degree of

DOCTOR OF PHILOSOPHY

of

HOMI BHABHA NATIONAL INSTITUTE

February, 2015

STATEMENT BY AUTHOR

This dissertation has been submitted in partial fulfillment of requirements for an advanced degree at Homi Bhabha National Institute (HBNI) and is deposited in the Library to be made available to borrowers under rules of the HBNI.

Brief quotations from this dissertation are allowable without special permission, provided that accurate acknowledgement of source is made. Requests for permission for extended quotation from or reproduction of this manuscript in whole or in part may be granted by the Competent Authority of HBNI when in his or her judgment the proposed use of the material is in the interests of scholarship. In all other instances, however, permission must be obtained from the author.

Place: Signature:

Date: **Name: N. Saibaba**

DECLARATION

I, hereby declare that the investigation presented in the thesis has been carried out by me. The work is original and has not been submitted earlier as a whole or in part for a degree / diploma at this or any other Institution / University.

Place: Signature:

Date: **Name: N. Saibaba**

CERTIFICATE

I hereby certify that I have read this dissertation prepared under my direction and recommended that it may be accepted as fulfilling the dissertation requirement.

Place: Signature:

Date: **Name: G.K. Dey**

Thesis Supervisor

List of Publications arising from the thesis

1. N. Saibaba, S. K. Jha, S. Tonpe, Kumar Vaibhaw, V. Deshmukh, S. V. Ramana Rao, K .V. Mani Krishna, S. Neogy, D. Srivastava, G. K. Dey, R. V. Kulkarni, B. B. Rath, E. Ramadasan and S. A. Anantharaman, "Microstructural Studies of Heat Treated Zr-2.5 Nb Alloy for Pressure Tube Applications", Zirconium ASTM-STP-1529, Pages-349-369, 2011 .
2. N. Saibaba, Kumar Vaibhaw, S. Neogy, K.V. Mani Krishna, S.K. Jha, C. Phani Babu, S.V. Ramana Rao, D. Srivastava, G.K. Dey, "Study of microstructure, texture and mechanical properties of Zr–2.5Nb alloy pressure tubes fabricated with different processing routes", J. Nucl. Mater., Volume 440, pp. 319-331, 2013.
3. N. Saibaba, N. Keskar , K. V. Mani Krishna, V. Raizada , K. Vaibhaw , S. K. Jha, D. Srivastava , G. K. Dey, "A numerical study of the effect of extrusion parameters on the temperature distribution in Zr2.5Nb", Available Online, J. ASTM International, 2015.
4. N. Saibaba, N. Keskar , K. V. Mani Krishna, V. Raizada , K. Vaibhaw , S. K. Jha, D. Srivastava , G. K. Dey, "Minimizing variability in microstructure, texture and mechanical properties in pressure tube manufacturing", to be communicated, 2015

Publications coming out of related work in collaboration with others:

1. R. V. Kulkarni, S. Neogy, B. N. Rath, K. V. Manikrishna, D. Srivastava, N. Saibaba, I. Samajdar, E. Ramadasan, G. K. Dey and S. Anantharaman, "Microstructural and Textural Evolution in Heat Treated Zr-2.5% Nb Pressure Tube Material Subjected to Dilatometric Studies", Trans Indian Inst Met, available online, 2011.
2. K. V. Mani Krishna, D. G. Leo Prakash, D. Srivastava, N. Saibaba, J. Quinta da Fonseca, G. K. Dey, M. Preuss, "Influence of Sn on deformation mechanisms during room temperature compression of binary Zr-Sn alloys", J. ASTM International, available online, 2015.
3. K. V. Mani Krishna, S K Sahoo, I Samajdar, S Neogy, R Tewari, D Srivastava, G K Dey, Gaur Hari Das, N Saibaba, S Banerjee, "Microstructural and Textural Developments During Zircaloy -4 Fuel Tube Fabrication", J. Nuc.l Mater., 383, pp 78-85, 2008.
4. R. V. Kulkarni, S. Neogy, B. N. Rath, K. V. Mani Krishna, D. Srivastava, N. Saibaba, I. Samajdar, E. Ramadasan, G. K. Dey, S. Anantharaman, "Microstructural and textural evolution in heat treated Zr-2.5%Nb pressure tube material subjected to dilatometric studies", accepted IIM-Transcations, 2011
5. K. V. Mani Krishna , D. Srivastava, G. K. Dey, V. Hiwarkar, I. Samajdar, N. Saibaba, Comparative study of methods of the determination of Kearns Parameter in Zirconium, J. Nucl. Mater. 414, pp- 492-497, 2011.
6. S. Neogy, S. Achary, K. V. Mani Krishna, D. Srivastava, G. K. Dey, C. Phani Babu, Gourahari Das, B. Raut, R. K. Chaube, S. K. Jha, B. Prahlad, N. Saibaba, A. Kumar and I. Samajdar, "Texture And Microstructure Development During Swaging And Annealing Process Of Fabrication Of Zircaloy-4 Rod Products", Materials Science Forum Vols. 702-703, pp 830-833, 2012.

N. Saibaba

ACKNOWLEDGEMENTS

I express my sincere gratitude to my guide Dr G.K. Dey, Associate Director, Materials Group for his constant guidance. He has provided the constant direction and counseling, which helped in meeting the deadlines. I also thank him for his valuable suggestions and for sparing his valuable time for technical discussions from time to time.

I thank Dr Srikumar Banerjee and Dr A.K. Suri, for making critical suggestions and providing valuable guidance during the course of my thesis.

The scope of this research involved working not only at laboratory scale but also at industrial scale. This would not have been possible but for the solid support and help provided by my colleagues from BARC and NFC. I am extremely thankful to Dr Dinesh Srivastava of Material Science Division, who has been involved throughout my doctoral studies and I am thankful for his constructive suggestions, discussions and useful criticism. I am thankful to every individual, who has been of help to me in carrying out my thesis work from both the institutes. I would like to place on record the special contributions from my colleagues from NFC: Shri S.K. Jha, Shri Kumar Vaibhaw and Shri Vikram Raizada for helping in hot forging and hot extrusion of the pressure tubes; Shri D. Pramanik for melting of Zr-Nb ingots; Shri C. Phani Babu and Shri G.N. Ganesha for pilgering of the pressure tubes; Shri J.K. Rout and his colleagues for heat treatment of tubes; Dr Komal Kapoor and Shri S.V. Ramana Rao for microstructure and textural characterization; Smt K.S. Lakshmi for mechanical testing and Shri R.K.. Chaube for inspection of pressure tubes.

I would like to thank Shri Suman Niyogi, Shri K.V. Mani Krishna and Shri N. Keskar of MSD, BARC for their contribution in TEM, Texture and microstuctural studies. I would also like to thank them for helping me in the preparation of manuscripts for publication as well as thesis. The help for conducting the dilatometer experiments from Shri R.V. Kulkarni, PIED, BARC is thankfully acknowledged.

I would like to place on record the useful discussions I had with Prof. I. Samajdar, IIT, Mumbai and several important inputs for my research work received from him. I also thank him for extending the support of his laboratory facilities for carrying out the characterization work.

I thank the Department of Atomic Energy and in particular Dr R.K. Sinha, Chairman, AEC and Secretary, DAE, for his encouragement in undertaking these doctoral studies.

I thank Mrs. Della Gabell for providing the secretarial assistance in preparing the manuscripts.

I sincerely thank my wife N. Sarada for her constant care, support and encouragement.

N. Saibaba

Contents

List of Figures

List of Tables

Abstract

The fabrication of Zr-2.5Nb alloy pressure tubes is quite complex and involves hot deformation (forging and extrusion), heat treatment (β quenching, annealing, autoclaving etc) and cold deformation (pilgering or drawing). In this research work, pressure tube material fabricated through two distinct routes which are generically known as cold work route and heat treated route, have been studied in detail. Hot extrusion stage is the most important step in the fabrication of the pressure tube manufacturing. In the present thesis FEM simulation of Hot extrusion process has been carried.

The influence of process parameters associated with hot deformation, heat treatments and cold deformation have been systematically studied. In the cold deformation route six distinct fabrication schedules were examined. These represented variations in (a) methodology of breaking cast structure (b) hot extrusion parameters (c) conditions of cold work and intermediate annealing. An optimized flow sheet could be developed on the basis of detailed characterization of the microstructure, texture and mechanical properties. The optimized process involved two stage forging followed by hot extrusion with higher extrusion ratio (12.75:1) and single stage of cold work without any intermediate annealing. This process resulted in desirable alpha morphology (1:10:70 aspect ratio) with a continuous fibrous beta morphology. The tube produced with this route had transverse basal texture component (f_t) above 0.6. Both this microstructure and texture are desirable for better creep resistance of the tube in reactor conditions. This route had also resulted in near elimination of end to end variation of the properties of the final tube.

On the basis of the present study on quenched microstructure, cold deformed and subsequent aged microstructure as a function of process parameters, optimized fabrication flowsheet to manufacture heat treated Zr-2.5 Nb alloy tube could be established. The optimized route included α+β quenching (840^{o}C) followed by cold deformation by pilgering and aging at 540^{o}C for 24 Hrs. The resulting microstructure consisted of primary α in conjunction with fine transformed lamellar α having dispersed equilibrium β globules inside it. The texture was also significantly different from that of the cold worked pressure tube. However the mechanical properties were comparable.

FEM simulation of hot extrusion process has been carried to understand role of extrusion temperature, extrusion ratio, ram velocity and profile of die on the extrusion process for obtaining desirable temperature, strain and strain rate distribution across the work piece. The model could be successfully validated against measured load data of the extrusion of actual pressure tube. The model could quantify the expected heterogeneity across thickness and length of the work piece as a function of various processing parameters.

Chapter 1

Introduction

1.1. Introduction

Pressurized Heavy Water Reactor (PHWR) also known as CANDU reactor uses natural uranium oxide as fuel and heavy water as a moderator and coolant [1-5]. A schematic diagram of the details of the reactor core is shown in Figure 1.1. The PHWR core essentially consists of a cylindrical shape calandria which contains heavy water moderator maintained at around 80°C. This has horizontal fuel channels whose numbers depends on the capacity of the reactor (e.g. 392 fuel channels for 540 MWe reactor). The fuel channels consists of thin wall seamless calandria tube, coolant or pressure tube separated by Zr-Nb-Cu garter springs [6]. The pressure tube contains natural Uranium fuel bundles and hot pressurized heavy water close to them. Thus the pressure tube, as shown in Fig. 1.2, which is nearly 6.4m long, 103mm inside diameter with 4.2mm wall thickness, acts as the pressure boundary. The cold moderator is insulated from hot pressure tube by filling the annular gap between pressure and calandria tubes with flowing CO_2. The presence of moisture in the annulus gas due to any leak in the pressure tube inside the reactor core is also detected. This enables detection of an early stage of the formation of a sub-critical, through-wall crack in the pressure tube in assuring leak-before-break of the tubes. The PHWR reactors have capability for online fuelling in the horizontal fuel channels. This is enabled by having cold rolled joint between pressure tubes and precipitation hardenable stainless steel end-fittings at each end of the channel. These channels are connected to the heat transport system by carbon steel feeders (Figure:1.2).

Zirconium base alloys are used as a structural material in the PHWR reactor because of their very low neutron absorption cross section and superior corrosion resistance in water at 300°C. They have excellent mechanical properties for the satisfactory performance of the component during their service in the reactor. Zircaloy-4 is used as fuel cladding material and calandria tube. Cold worked Zircaloy-2 or Zr-2.5Nb alloy is used as coolant or pressure tube material [6-8]. In recent times, the Zr-2.5 Nb alloy material is being used in PHWRs due to its better strength, creep properties, better corrosion properties and exceptionally low hydrogen pick up. The pressure tube in reactor is exposed to high temperature of 300^{o}C,

pressure of 110 MPa, bending stresses due to weight of coolant and fuel bundles and irradiation environment of high neutron flux. Thus integrity of the pressure tube material is of paramount importance for safe and long life of the reactor [6, 9]. Hydriding, corrosion and dimensional changes of the pressure tube are principle causes of its degradation limiting the life in the reactor. The former two degradation processes are critical for safety of the reactor but they are not life limiting factor in-service operation of pressure tubes [6, 10-13]. The dimensional changes of pressure tube occur due to the combined effect of irradiation creep, irradiation growth and thermal creep. However, contribution of thermal creep is not substantial. Irradiation growth may compensate to some extent effect of the irradiation creep due to a specific texture in pressure tube. Thus axial and diametral expansion of pressure tube occurs mainly due to irradiation creep [14,15].

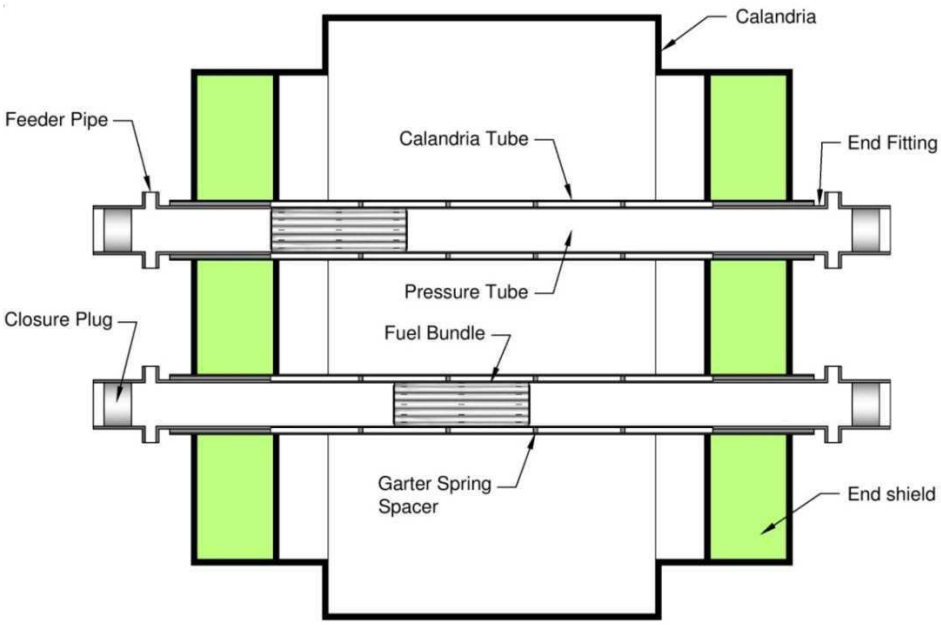

Figure 1.1Schematic showing the calandria vessel with important structural components of the PHWR.

The axial elongation is accommodated by providing the bellows at the end of the coolant channels. However, diametral strain beyond certain limits (~4%) results in unacceptable coolant bypass. Therefore, diametral creep is main factor dictating the life of the pressure tube. In recent times, there has been a greater interest towards increasing the life of

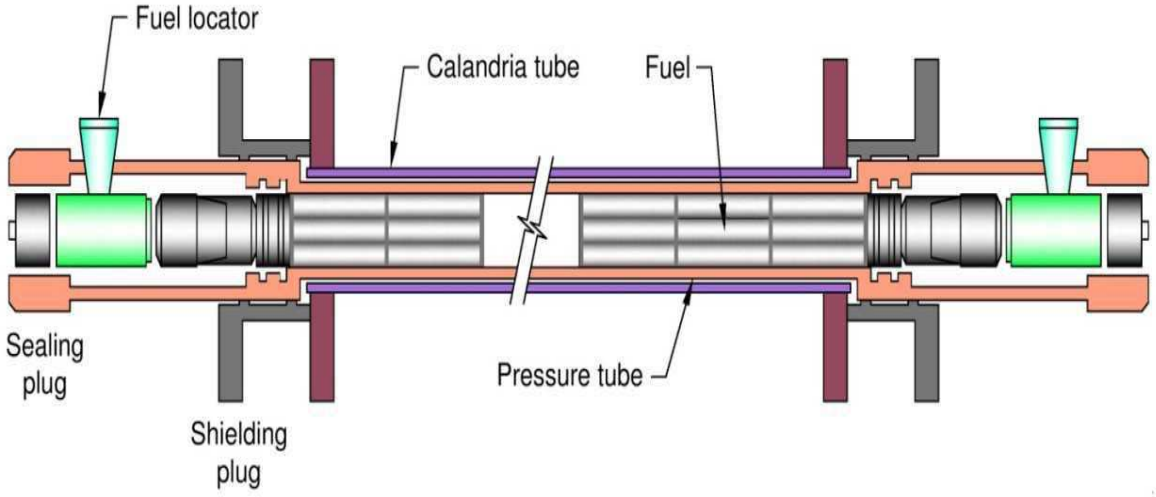

Figure 1.2: Schematic showing the coolant channel assembly depicting various important components

pressure tubes in advanced reactors. Several studies have shown that irradiation creep strongly depends on the microstructure and texture in addition to the operating environment i.e., temperature, pressure and neutron flux.

The microstructural features includes nature of phase, its distribution, morphology, grain shape and size, type of dislocations and dislocation density etc. [16,17]. The large operating experience of pressure tube performance in PHWR reactors has helped in establishing the correlation between the individual microstructural features with diametral and axial creep. It is now relatively understood that in the cold worked Zr-2.5Nb alloy pressure tube radial basal texture increases and transverse basal texture decreases the diametral strain. In the earlier studies it has been reported that pressure tubes having higher radial thickness of alpha grains, with large aspect ratio, and additionally consisting of larger circumferential basal pole texture have shown better diametral dimensional stability. The combined effect of these two is shown in a diagram in Figure 1.3. The alloy chemistry also plays important role in irradiation creep behavior. The elements such as oxygen and niobium which strengthens the material tend to modify the texture and hence their creep behavior [14]. Iron is an important alloying element which preferentially goes to the bcc beta phase and decreases axial creep to a greater extent. All the above factors affecting the creep

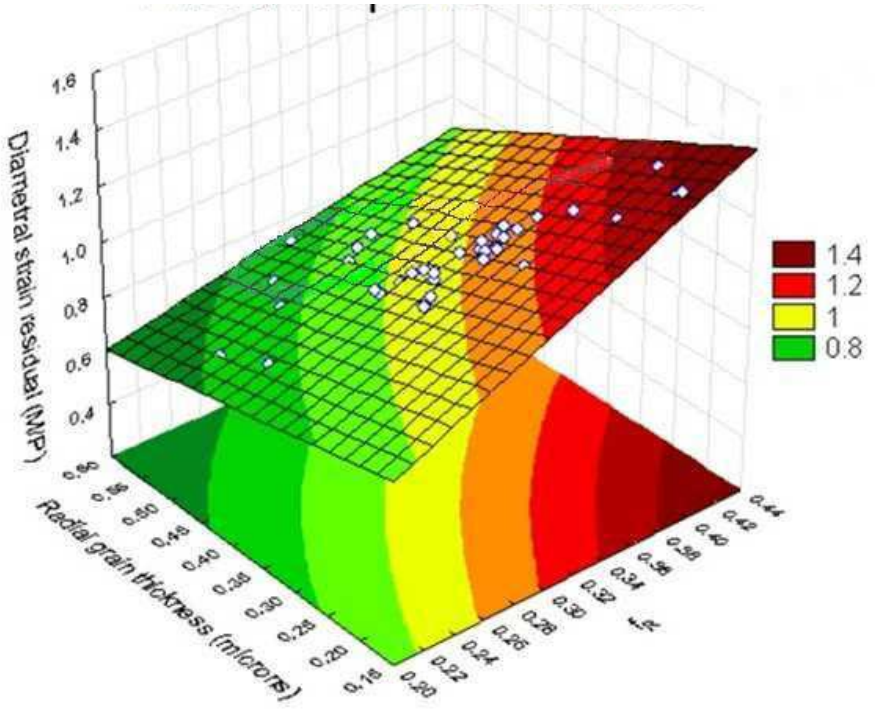

Figure 1.3: The effect of radial grain thickness and radial basl pole texture on diametral creep of the pressure tube in PHWR

behavior of the Zr-2.5Nb alloy to a large extent depends on the manufacturing route of the process tube. The fabrication of pressure tubes involves a large number of thermomechanical treatments, and the final microstructure and texture developed as a result of these fabrication steps determines the long-term and short-term properties of these tubes. For example the higher extrusion ratio during hot extrusion process results in higher transverse basal texture and higher aspect ratio of the grains. The variability in the microstructure, texture and mechanical properties introduced during fabrication also results in variable creep behaviour which is of great concern for the PHWR reactor operators [18,19]. There has been a continuous effort towards improving the resistance to irradiation induced creep and growth through the modification of the microstructure of the pressure tube material to achieve longer life of the pressure tube in next generation advanced reactors. In this study an effort has been made to understand the influence of each of these fabrication steps on microstructure and crystallographic texture in order to optimize the pressure tube fabrication. This forms the basis and is the motivation for the present study.

Zr-2.5Nb alloy is a two phase alloy and there can be variety of phase transformations produced from the high temperature beta phase by controlling the beta phase composition and cooling rate. Thus, it is possible to generate a range of microstructures and textures by suitable heat treatment methods. Many researchers have studied the change in microstructure and its effect on the properties by altering the conventional route of pressure tube fabrication. Generally, Zr-2.5Nb alloy pressure tubes in PHWR are used in cold drawn condition but they have been used in heat treated conditions as well as in RBMK and FUGEN type of reactors. Unlike cold worked pressure tube, in depth understanding about the mechanisms of microstructural evolution during heat treatment processing steps of the materials is not available. The objective of the present study is to optimize the fabrication processing parameters with special reference to the quenching and aging treatments. The aim has been to demonstrate a heat treatment route to produce pressure tube which is better than the cold-worked tube, and that will have enhanced microstructural stability during high temperature irradiation

Hot extrusion fabrication is the most critical stage in fabrication of pressure tube. The microstructural features, texture and mechanical properties of the finished tube to a large extent is determined by hot extrusion process [20]. The quality of the extruded product in terms of variation from leading end to tailing end, surface cracks, ovality dictates the finished tube quality. Hence a detailed knowledge of the role of process parameters such as billet preheat temperature, extrusion speed, extrusion ratio etc on the temperature and stress distribution during the hot extrusion process is desirable. However, to acquire such information through experiments during hot extrusion process is rather difficult [21, 22]. Application of computational/numerical analysis of the extrusion process is the only way to obtain the distribution of temperature, strain and strain rate throughout the work piece. Three-dimensional finite element analysis of Zr based alloys seems to be rather limited in the open literature, forming the motivation to present study. Some of the key parameters of the extrusion process such as ram velocity, billet pre-heat temperature, fillet radius and reduction ratio, have been studied for their role in determining the overall temperature distribution during hot extrusion, requirement of ram force etc.

The brief description of the individual chapters of the thesis is outlined below.

The overview of the literature relevant to the objectives of the present research work has been presented in the chapter 2. The chapter includes information with regard to microstructure,

phase transformation, deformation behaviour, texture and properties of zirconium and its alloys. This chapter also presents the knowledge on the effect of various thermo-mechanical treatments on microstructure and texture of Zr-2.5%Nb pressure tube material. The in-service performance in terms of irradiation creep, irradiation growth in particular dimensional stability in the reactor is reviewed in the present chapter.

The details of the experimental procedure adopted for various characterization techniques in this research study have been detailed in chapter 3. In the present study the industrial scale fabrication of pressure tube is also included. The details of the individual process are also presented in this chapter.

The chapter 4 presents the scheme of the study to enhance and optimize the presently followed fabrication route for cold worked tube. In this work, three major stages of the fabrication schedule which are expected to have significant effect on the pressure tube properties, in particular, its mechanical properties and microstructure have been studied. These are mainly primary breakdown of the cast ingot, extrusion to tubular blank and cold work subsequent to the extrusion to achieve final dimension of the pressure tube. The results on full industrial scale (used for manufacturing 6.4m long pressure tube) are also presented. The results on evolution of microstructure, texture and mechanical properties as a function of the process parameters of different fabrication stages is presented in this chapter. Detailed microstructural characterization was carried out at each step in all these trials to ascertain the morphology of the alpha phase, distribution and composition of the beta phase and crystallographic texture. Mechanical property evaluation has also been done to establish structure-property relationship.

Chapter 5 describes studies related with development of the heat treated pressure tube. Quenching dilatometer study was performed to establish the transus temperature for the alloy used in this study. This chapter presents the optimization of fabrication parameters to manufacture heat treated Zr-2.5 Nb alloy tube. It presents the results obtained from controlled heat treatment in dilatometer on microstructure evolution at different soaking temperatures and cooling rates. The result is also presented for the heat treated real dimension tube on the basis of the results in quenching dilatometer. This chapter also presents results on the quenched microstructure and further cold deformed and subsequent aged microstructure. The results on mechanical properties of the finished heat treated pressure tube and bulk texture at

different stages of fabrication have been presented. The results have been compared with conventionally fabricated cold work route.

In Chapter 6, FEM simulation of hot extrusion of Zr-2.5Nb alloy pressure tube has been presented. The theoretical basis of hot extrusion model using 3D FEM method has been described in this chapter. Hot extrusion simulation study in this chapter has brought out the role of extrusion temperature, extrusion ratio, ram velocity and profile of die on the extrusion process. The effect of these process parameters on the overall temperature distribution and hence on the resulting microstructural and textural homogeneity has been discussed in this part of thesis. This FEM analysis has effectively shown quantification of the extent of differences in temperature distribution between leading and trailing ends and also across a given cross section.

Chapter 7 presents the summary of the important findings of the present research work. The results are compared with reference to knowledge available in the literature. The future scope of the work is also outlined in the thesis.

Chapter 2

Review of the Relevant Literature

The overview of the published literature relevant to the objectives of the present research work has been presented in this chapter. The chapter provides information available in the literature pertaining to metallurgy of zirconium alloys and in particular to Zr-2.5 Nb alloy which includes microstructure, phase transformation, deformation modes and basic properties [6], [10]. This chapter also presents the knowledge on the effect of various fabrication parameters on microstructure and texture of Zr-2.5%Nb pressure tube material. The various factors affecting the dimensional stability in the reactor is reviewed in the present chapter.

2.1. Zirconium and Zirconium alloys

Zirconium and its alloys are extensively used as structural materials in nuclear reactors, because of their unique combination of good corrosion resistance in water near 300° C, good mechanical properties and low capture cross section for thermal neutrons [1]. These components are mostly used in the form of tubes of different size ranges for applications such as fuel sheathing, guide tubes/calandria tubes, and pressure tubes [6, 10]. The designing of zirconium alloys for nuclear applications requires that thermal neutron absorption cross-section of pure zirconium does not increase significantly. Therefore, only relatively small amounts of alloying elements are added. The alloying elements were added in zirconium alloys primarily to improve the corrosion behaviour in water [10, 23-26]. For example tin was added to counteract the detrimental action of nitrogen on corrosion resistance. Small amounts of iron, chromium and nickel found to improve the corrosion resistance of zirconium-tin alloys due to the formation of intermetallic second phase particles (SPPs). The size and distribution of the SPPs is strongly correlated to the corrosion resistance. The zircaloys which contain about 1.5 wt% Sn and Fe, Ni, and O as alloying elements have two important derivatives; zircaloy-2 and zircaloy-4. Zircaloy-4 is a nickel-free variant of Zircaloy-2 with similar oxidation behaviour, but different level of affinity with hydrogen [23-24]. Zirconium-niobium alloys showing better strength and improved corrosion resistance have been used for reactor components, the zircaloys, are widely used in both pressurised water and boiling water reactors as fuel cladding

materials In PHWRs, they are used as fuel cladding, calandria tube in the early stages [27,28], cold-worked Zircaloy pressure tubes were used

Russians were the first one to report that an alloy of zirconium containing 1-5% niobium has superior mechanical strength and adequate corrosion resistance in comparison to Zircaloys. Subsequently Zr-2.5%Nb alloy as a pressure tube material and the Zr-1.0%Nb as a fuel cladding material have been found to be attractive because of their high strengths at the operating temperature [29]. This permits the use of thinner components, reducing the loss of neutrons by parasitic absorption with an accompanying improvement in corrosion resistance. Since 1967 CANDU reactor started using cold-worked Zr-2.5Nb as pressure tube material and subsequently all such PHWR reactors were using this material as pressure tube due to its higher strength, creep and fracture strength [1, 6, 7]. It was reported that in comparison to cold-worked Zircaloy-2, cold-worked Zr-2.5Nb has extraordinarily low deuterium absorption and good corrosion resistance [6, 9]. In the same study it was shown that the corrosion of Zr-2.5Nb tubes was about one-third of that in Zircaloy-2 under similar operating conditions, and the deuterium uptake was only 2%~4% of that measured for Zircaloy-2 [11]

2.2. Physical metallurgy of Zr alloys

Zirconium based alloys are stable in the alpha phase (α), zirconium, with a hexagonal close-packed (hcp) structure at temperatures below 800°C (Figure 2.1 (a)) [24, 30-32]. The typical values of the 'a' and 'c' parameters are ~3.232Å and ~5.147Å respectively. The main crystallographic planes in this structure are the basal (0002) and two types of prismatic planes (11-20) and (10-10) which are shown in Figure 2.1(b). In zirconium the c/a ratio is ~1.598, which is less than the ideal sphere packing (c/a=1.633).

Alloying elements in zirconium alloys can be classified into α-stabilisers and β-stabilisers. Aluminium, tin, hafnium, nitrogen and oxygen are important α stabilising elements. Phase diagrams for many of the binary alloy systems for α-stabilisers exhibit a peritectic or a peritectoid reaction at the zirconium-rich end [33-35]. β-stabilisers include iron, chromium, nickel, molybdenum and niobium. For binary alloys between zirconium and these elements, there is usually a eutectoid reaction, and often a eutectic reaction at the zirconium-rich end of the phase diagram. A number of β-stabilising elements such as iron, nickel, chromium, and molybdenum have very little solubility in the α phase and they form

ordered intermetallic phases which are readily precipitated even in very dilute zirconium alloys, resulting in precipitation hardening [33, 36].

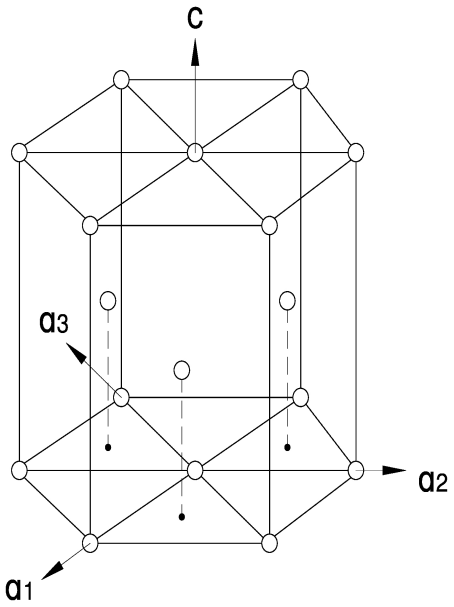

(a)

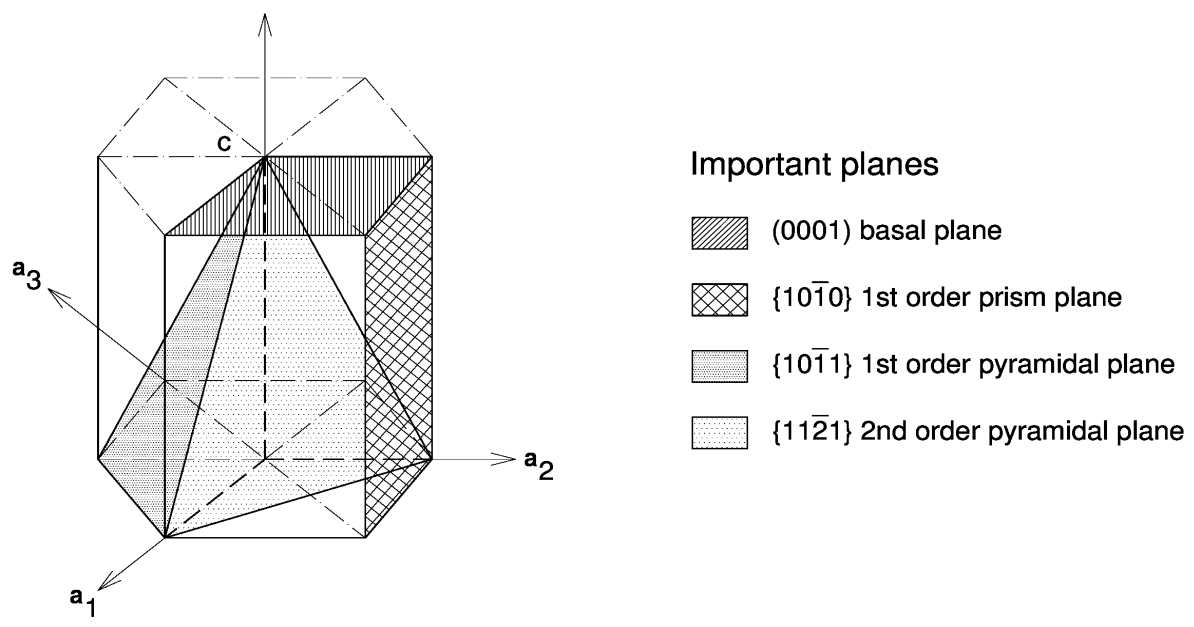

(b)

Figure 2.1: (a) Unit cell of hexagonal closed packed (hcp) crystal. (b) Some of the important planes and directions of the hcp crystals

Figure 2.2 shows the Zr-Nb equilibrium diagram which provides the basis for studying the equilibrium transformations. An analysis of the phase diagrams can be utilized in studying the metastable steps in the sequence of transformation events in this system. This system is characterized by complete solid solution in the β (bcc) phase at sufficiently high temperatures and a tendency for phase separation in the ß phase, as reflected in the miscibility gap, at temperatures below about 970°C ($\beta_{Zr} + \beta_{Nb}$ miscibility gap); the following monotectoid reaction occurring at 610°C:

$$\beta_{Zr} \rightarrow \alpha_{Zr} + \beta_{Nb}$$

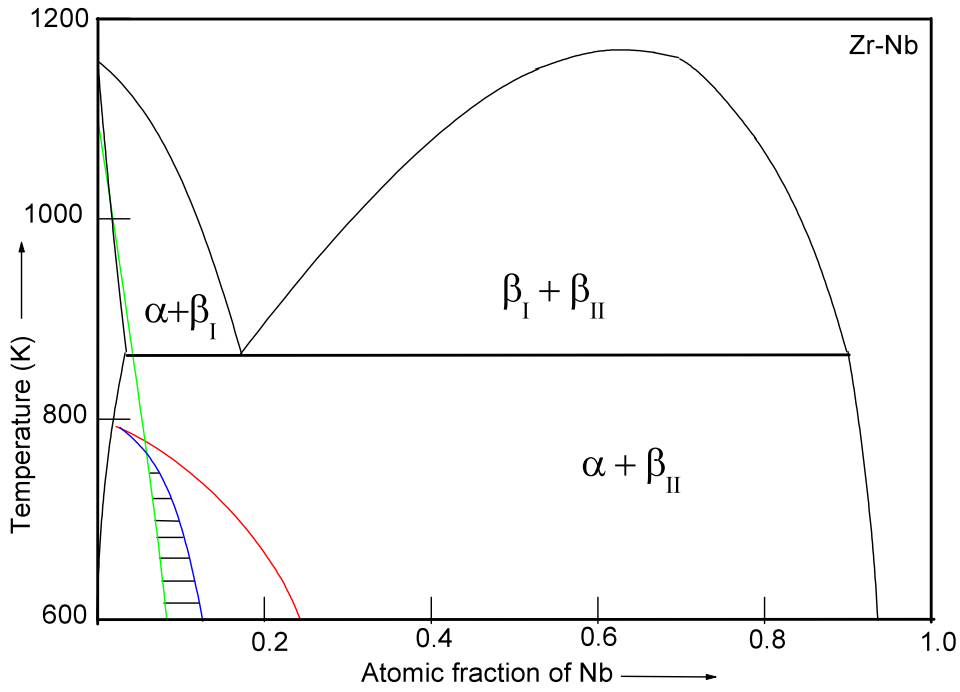

Figure 2.2: The phase daiagram of binary Zr-2.5Nb alloy also showing the metastable phase transformations.

A variety of equilibrium and metastable phases can be obtained from the high temperature β phase in zirconium rich Zr-Nb alloys. The β phase in the Zr-Nb system exhibits tendencies for the β→α martensitic transformation, the β →ω displacive transformation and the $\beta \rightarrow \beta_{Zr} + \beta_{Nb}$ phase separation reaction in different composition and temperature domains. This β phase instability is known to influence the sequence of phase transformations in

zirconium (and titanium) alloys. Various possible phase transformations from the high temperature beta phase is shown in a schematic diagram (Figure 2. 3). In dilute Zr-Nb alloys, it is well established that the β phase, having the same composition as that of the alloy cannot be retained at ambient temperatures even by very rapid quenching. In alloys containing upto 8% Nb quenching from the β phase field rapidly through the equilibrium α+ β region results in a martensitic structure. Beyond this composition and upto about 17% Nb, quenching from the β phase leads to the formation of an athermal ω phase dispersed in the β phase. The ω instability disappears beyond 20% Nb, where the β phase is fully stabilized [37]. Less rapid cooling of dilute Zr-Nb alloys from the ß phase field results in formation of characteristic Widmanstatten α plates by a nucleation and growth process. The approximate phase boundaries for the metastable

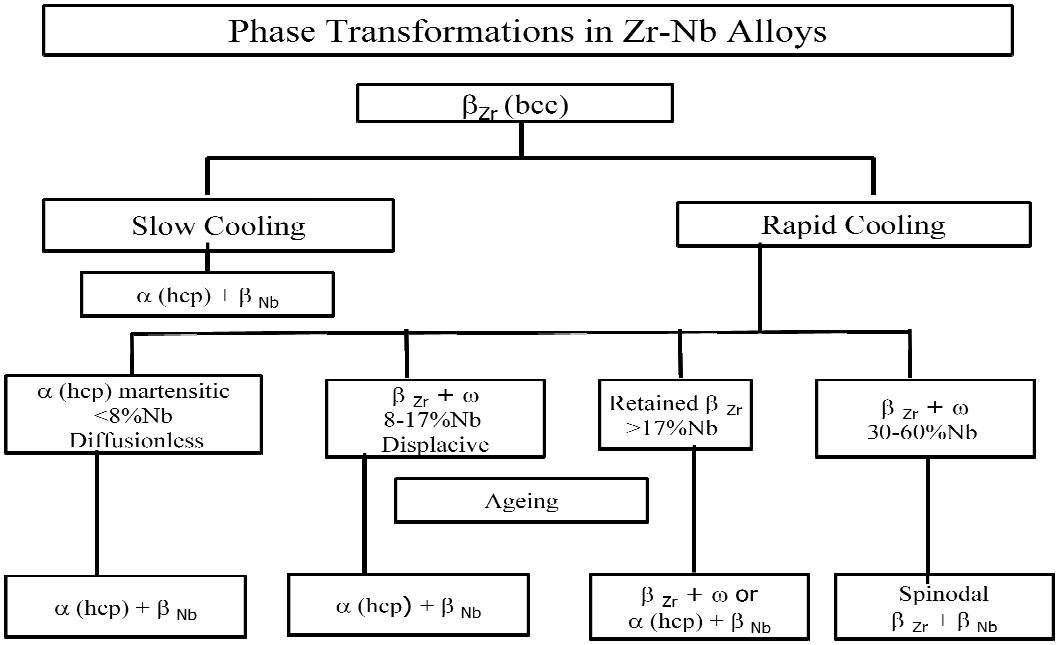

Figure 2.3:Phase transformations from the high temperature beta phase

phase transformations are shown in phase diagram. The stabilized β phase in Zr-Nb alloys with higher niobium contents can decompose on ageing either by α phase formation or by isothermal ω phase formation or by both these modes, depending upon the temperature of ageing and the composition of alloy. In the niobium lean alloys where the β phase transforms martensitically to α' phase, the β phase can reappear on tempering the martensite either on the martensite plate boundaries or within the martensite plates. In addition to the various possibilities of

transformation of the β phase to athermal ω, isothermal ω, α' and α phases, it can undergo hydride formation in alloys containing hydrogen [38-40].

2.3. Deformation of Zirconium and its alloys

Due to non symmetric hexagonal closed packed structure of Zirconium alloys they exhibit limited number of slip systems. The main slip planes in an HCP structure are basal {0001}, prism {101_0} and pyramidal {101-1}. The slip planes along with corresponding slip directions are shown in Figure 2. 4. In zirconium alloys both slip and twinning mechanisms play equally important role in the deformation [24, 32, 41-42].

2.3.1. Slip Modes

Slip is the usual plastic deformation for most metallic materials. Slip occurs when shear stress exceeds a critical value for one definite slip plane. Slip occurs most readily in specific directions on certain crystallographic planes. Slip operates on a plane and direction for which critical resolved shear stress (CRSS) is the lowest. This is because of the fact that the slip plane is the plane with highest atomic density and the slip direction is the direction that contains the shortest Burgers vector. The slip plane together with the slip direction establishes the slip system. Lattice constant ratio c/a varies from one HCP material to another. Ratio c/a is one important parameter to describe the deformation behavior of HCP material and determines the dominance of any particular slip system at a given temperature and stress conditions [43]. The c/a value of the ideal sphere packing is 1.633. For a given hcp material it can be larger than, equal to or smaller than ideal c/a value.

For HCP metal (Zn, Cd and Co) with c/a ratio equal to or greater than 1.633, slip occurs on the (0001) plane and in the $\langle 11\bar{2}\,0\rangle_{\alpha}$ direction. c/a for zirconium is 1.589 less than ideal value of 1.633, its primary slip system at room temperature has found to be prism slip on {1010} plane along $\langle 11\bar{2}\,0\rangle_{\alpha}$ direction. Slip has also been observed in the same direction on the (0001) basal plane. In the HCP metals, the only plane with high atomic density is the basal plane (0001) and it has three $\langle 11\bar{2}\,0\rangle_{\alpha}$ close-packed directions. The HCP crystal possesses three slip systems compared with possible 12 slip systems for FCC and 48 possible slip systems for BCC, The limited number of slip systems is the reason for the ductility being strong function of orientation in HCP materials. It is reported that that prism slip is more

commonly observed in recrystallized zircaloy and basal slip in cold-worked zircaloy materials.

This has been explained on the basis that dislocation hardening makes the slip on basal plane easier in comparison to prism slip. The higher value of ductility of zirconium alloys have been attributed to observation of prism slip with (c+a) type Burgers [44-46]. The slip mode has been observed to change with temperature and slip on pyramidal planes {10-11} and {11-21} in (c+a) directions is also observed.

2.3.2. Twinning

The second important deformation mechanism is the process known as twinning. Twinning is one process during which a portion of the crystal moves with respect to the adjacent zone. The interface between the twinning area and untwined area is called twinning plane [47-50]. In a simple lattice, each atom in the twinned region moves by a homogeneous shear and the distance is proportional to its distance from the twin plane. The lattice strains produced by twinning configuration in a crystal are small, so that the amount of gross deformation due to twinning is small. The important role of twinning is not only the deformation coming from the twinning process, but also the orientation changes resulting from twinning, which may place new slip system in a favorable orientation and additional slips can take place [48, 51]. Thus, twinning is important in the overall deformation of metals with a low number of slip systems, such as HCP materials. Grewen found that activation of twinning system depends on the orientation of basal plane. At room temperature following tension twins {10-12}<10-11>,and {11-21}<11-26> compression twin {11-22}<11-23> are reported.

2.4. Texture in Zirconium alloys

In a polycrystalline material if all the crystals are randomly oriented with respect to each other, then one would expect an isotropic nature of the product. The grain orientation in polycrystals is usually different from that of its neighbors and certain grains (orientations) prefer to cluster and orient in a specific direction this tendency is called preferred orientation or crystallographic texture [43, 52-54]. Zirconium base alloys being anisotropic in nature it results into preferential orientation of certain plane normals in certain direction during thermo mechanical treatments which gives rise to the texture.

Texture is measured for certain crystallographic directions aligned toward certain specific direction of the sample geometry as shown in figure 2.5. Texture results in the anisotropy in the properties of the product. This anisotropy can be seen in the mechanical properties, irradiation creep, irradiation growth, hydriding behavior, oxidation and corrosion behavior [13, 14, 55, 56]. Therefore it becomes important to understand the mechanism of texture development as a function of thermo-mechanical parameters to obtain desired texture in the product.

2.4.1 Texture Characterization

There are different techniques which are available to quantify textures, but mostly diffraction based techniques such as X-ray diffraction, EBSD and neutron diffraction techniques [57-62] are used for texture characterization. But texture evaluation by X-ray diffraction techniques is the most widely used techniques as it is the most reliable and easily available technique for the quantitative analysis of the texture.

Neutron diffraction is used to measure crystallographic texture in a similar way to that of x-rays. Compared to the x-ray diffraction there are much lower absorption and much higher penetration depth for neutron in the material. However, the low availability of the neutron source is the biggest disadvantage. In case of electron diffraction, as electrons are charged particles, its penetration depth is small so it allows diffraction only from individual grains rather than bigger volume as in the case of x-ray and neutron diffraction. Electron diffraction can be obtained in Transmission electron microscope (TEM) and scanning electron microscope (SEM) [63-65]. The advantage here is that both diffraction as well as image of the same region can be obtained concurrently. In X-ray diffraction bulk texture of a volume of materials is obtained by measuring the intensities of diffraction of individual diffracting planes.

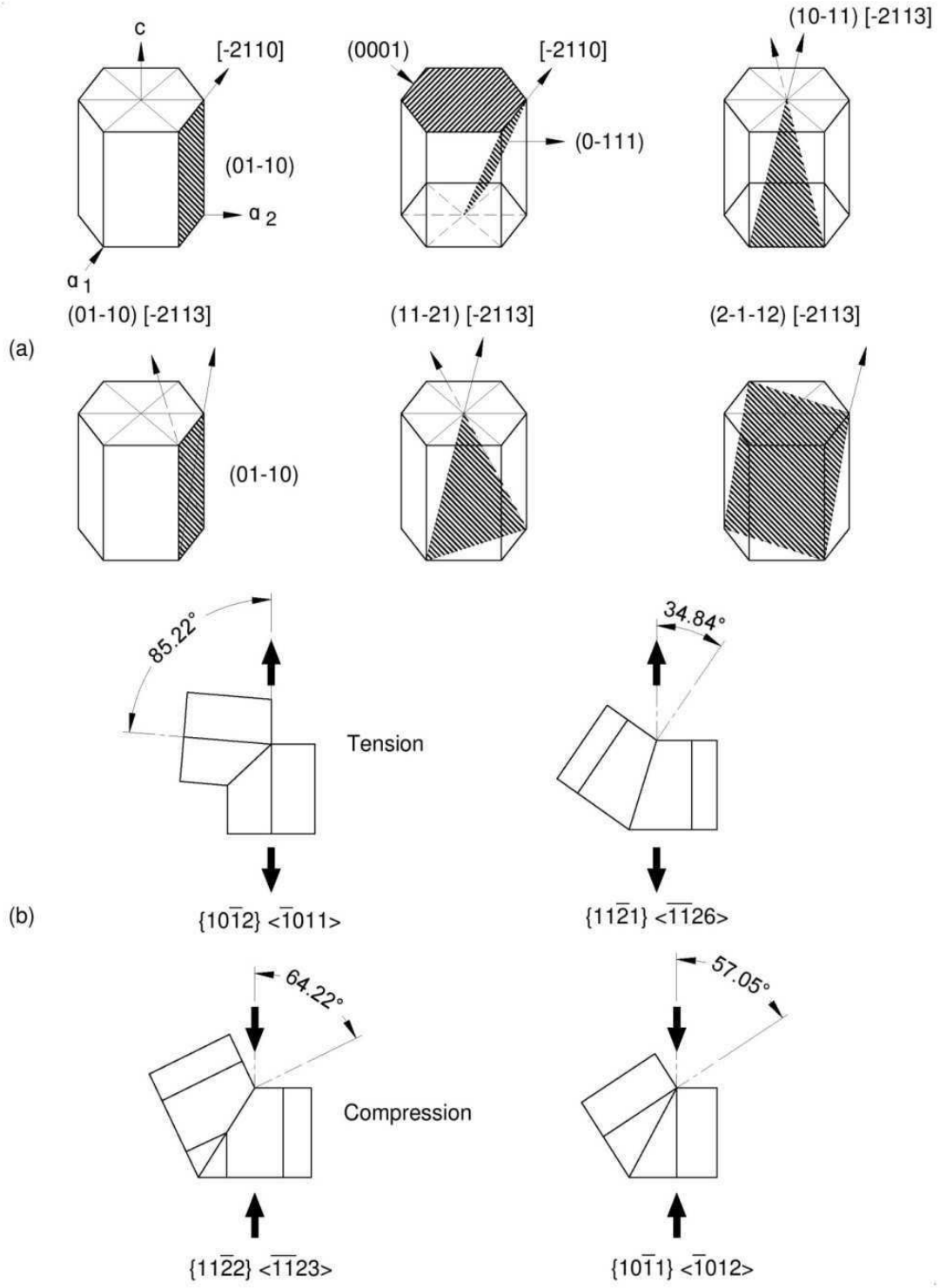

Figure 2.4: The various deformation modes observed in the hcp zirconium alloys.

EBSD is a technique based on measurement of local crystallographic orientation [57]. In these technique very small volumes of material at specific points on the surface of a sample is probed by using electron diffraction in an electron microscope. This technique enables us to relate the crystal orientation to the microstructure. The orientation of a single point in a sample can be distinguished and orientation distribution as a function of sample location can be obtained. In EBSD orientation maps can be constructed with spatial resolution, in most modern systems as small as 0.05μm. In one of the report Manikrishna et al have compared these texture characterization techniques for Zirconium alloy products.

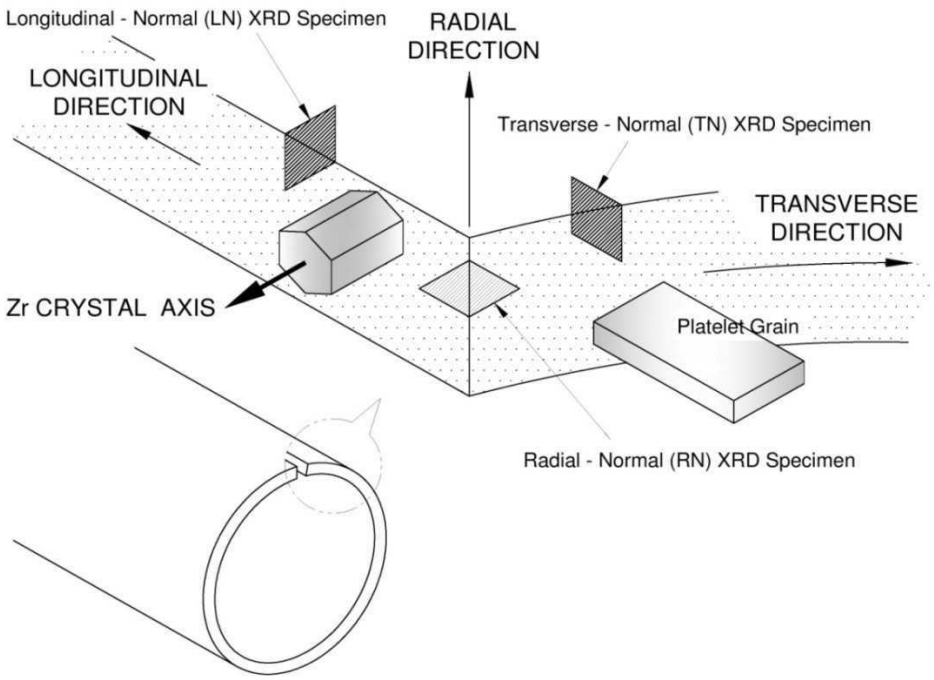

Figure 2.5: The three principle direction of relevant for the texture and mechanical properties the zirconium alloy tubular product

The crystallographic texture is normally presented as orientation distribution of crystallographic planes either in specimen reference frame or in crystal reference frame. Pole figures, inverse pole figures and orientation distribution functions (ODF) are normally used to represent crystallographic. Both direct and inverse pole figures are the representation of crystallographic texture on two dimensional scales, and ODF describes the three dimensional distribution of the grain orientations [66]. In the specimen reference frame, it is called direct pole figure (DPF), which shows the relative intensity of all diffracting planes along a

particular sample direction such as basal pole figure (0001), prismatic pole figure (01-10) and pyramidal pole figure (101-2) respectively. In the crystal reference frame, the distribution of the crystallographic intensity is called inverse pole figure, which shows the variation in pole density of one particular set of crystallographic planes in axial direction, hoop direction or radial direction of the sample. Complete quantitative description of the texture is obtained in crystallite orientation distribution function (CODF) [25], this gives the probability that a grain lies within a certain range of orientations with respect to a coordinate system (e.g. three orthogonal specimen directions rolling direction, transverse direction and normal direction are chosen as the specified coordinate system (Figure 2. 5). Normally for zirconium alloys ODF is created using basal (0002), pyramidal {10-11} and prismatic {10-10} pole figures [25].

2.4.2. Kearns Factor

Other numerical parameters have been developed, such as the Kearns factor [67]. However, within the zirconium community, the Kearns factor has become widely used and accepted. The Kearns factor describes the effective fraction of hexagonal crystals with the basal pole aligned along a particular sample axes. The value is given by [68]:

$$f_1 = \frac{1}{N}\int_0^{\pi/22}\int_0^{\pi} I(\alpha,\beta)\sin^3(\alpha)\cos^2(\beta)d\beta d\alpha$$

2.4.3. Development of texture in Zirconium alloys during thermo mechanical processing

Apart from materials variables such as crystal structure and associated phase transformation, the processing variables which affect the development of texture include the temperature and stress system applied during mechanical deformation. This include amount of deformation area-reduction, strain ratio Q, strain path, deformation temperature, intermediate and final annealing conditions.

During cold rolling HCP materials show strong tendency for basal poles to be oriented around the normal direction. The tilt of the basal poles from the normal direction depends on the c/a ratio of the materials. For materials like zirconium base alloys (c/a <

1.633), the basal poles tilt of 20 to 40° from normal direction toward transverse direction is observed with [10-10] direction lying parallel to the rolling direction.

The process stress and strain vary according to the different fabrication techniques used for shaping of material. In the tube reduction process such as Pilger milling it involves triaxial stresses and strains. During cold deformation the two major factor i.e. the initial texture and the area reduction, wall thickness reduction, and the applied strain path decides the final texture as shown in the schematic diagram by Tenkohoff [24] (Figure 2.6). The first one is determined by the previous thermomechanical process, and the second one depends on the characteristics of deformation process. The two parameters area-reduction factor, R_a, and the other strain ratio factor Q-factor gives rise to different deformation texture after a given deformation pass. In a schematic in the figure Technoff, have described development of texture as a function of above two parameters during tube reduction process.

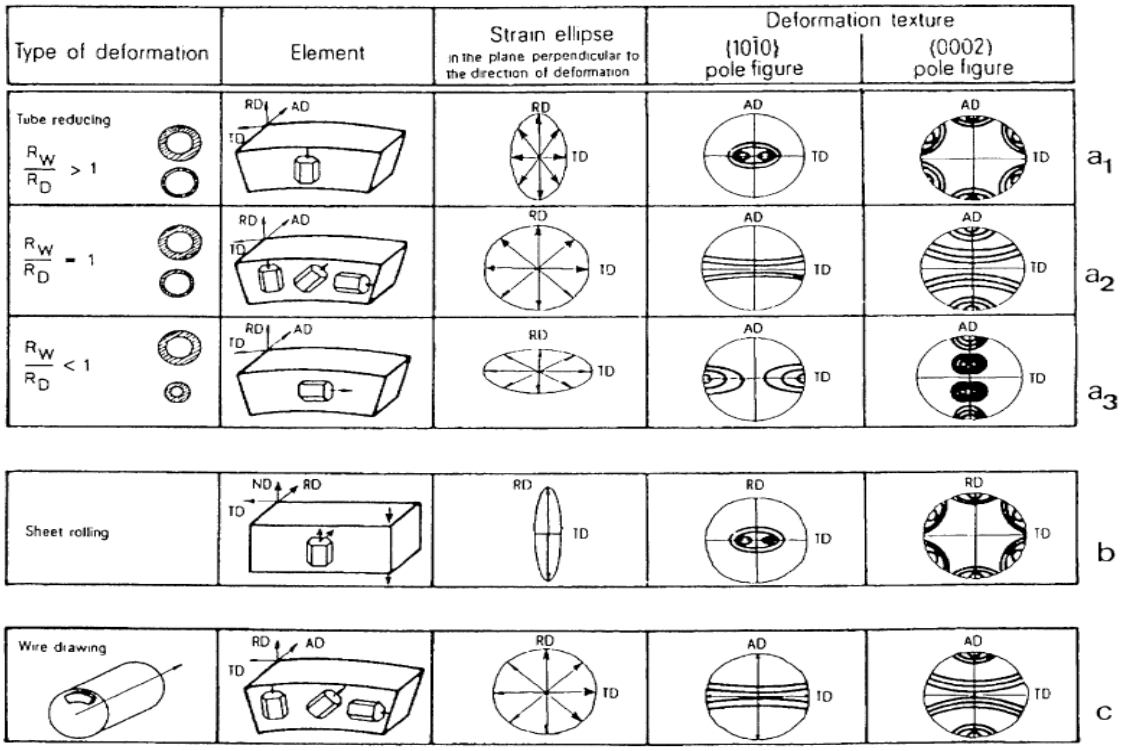

Figure 2.6: Development of texture during different deformation experienced for various forming process

2.5. Material degradation

The pressure tube is exposed to the coolant having temperature 520-580K and coolant pressure of 10 MPa. It also bears the weight of coolant and fuel bundles. The pressure tubes experiences a biaxial stress state condition corresponding to thin-wall condition. This load and the water pressure results in the hoop stress of approximately 65 Mpa in circumferential (transverse) direction and approximately 122 Mpa in axial (longitudinal) direction. Pressure tubes also experiences irradiation damage due to irradiation by fast neutron flux. A typical distribution of temperature and neutron flux from inlet to the outlet of the pressure tube is shown in Figure.2.7. This results in irradiation induced deformation by both irradiation creep and irradiation growth. As a result, during in service reactor operation, the combined effects of temperature, stress and irradiation the dimensions of the pressure tubes changes. The dimensional changes are observed due to the net effect of thermal creep, irradiation creep and irradiation growth [14-16]. However, the contribution of thermal creep is of much lesser extent. Dimensional change in the pressure tube is the principle factor for restricting their reactor life to typical 25-30 years.

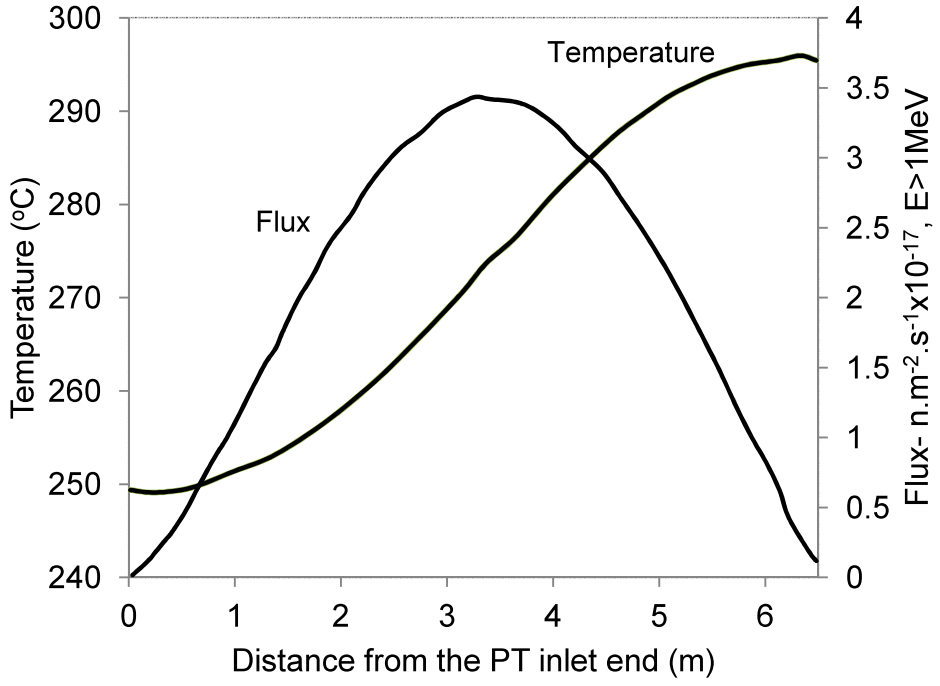

Figure 2.7: A typical distribution of temperature and neutron flux from inlet to the outlet of the pressure tube in a PHWR reactor

The various dimension changes in pressure tube that happen are:

i) Diametral expansion: The diameter of the pressure tube increases with time mainly due to irradiation creep under the action of the hoop stress resulting from the pressurized coolant. The irradiation growth contribution is mostly restricted to the central region of the pressure tube where the neutron flux is high. The reported diametral strain observed along the length of the pressure tube is shown in Figure 2. 8. However, it is reported that due to a specific texture and microtexture of pressure tube irradiation growth has a negative component and this decrease the total amount of diametral expansion.

ii) Axial elongation: Due to a combination effect of irradiation creep and irradiation growth the pressure tube elongates. Total elongation increases with accumulated fast neutron fluence.

iii) Sag: The pressure tube undergoes sag mainly by irradiation creep from the weight of the fuel bundles and the heavy water. A typical observed value of the sag along the length of the pressure tube is shown in Figure 2. 9.

iv) Wall thinning: As creep and growth occurs at constant volume, the increase in diameter and length result in a reduction in the wall thickness of the pressure tube.

The service life of the pressure tube in the reactor is managed by controlling the different degradation processes such as dimensional changes, irradiation induced material property changes, corrosion and hydrogen ingress [14, 68-69]. However, hydrogen pick up in Zr-2.5Nb alloy being significantly low, it is the deformation of pressure tubes mainly determines fuel channel life.

The irradiation enhanced changes in shape and dimensions in cold-worked Zr-2.5Nb pressure tubes in service in PHWR reactors due to the irradiation creep and irradiation growth has been reviewed extensively [16]. The effect of microstructure and texture of the tubes on irradiation creep and growth has been especially investigated in detail. Both irradiation creep and growth are strong functions of microstructural features which include the shape, the size and the size distribution of the grains, the distribution of various phases, the interfacial structure, dislocation density, and the crystallographic texture. In the earlier studies it has been reported that pressure tubes having higher radial thickness of alpha grains, with large

aspect ratio, and additionally consisting of larger circumferential basal pole texture have

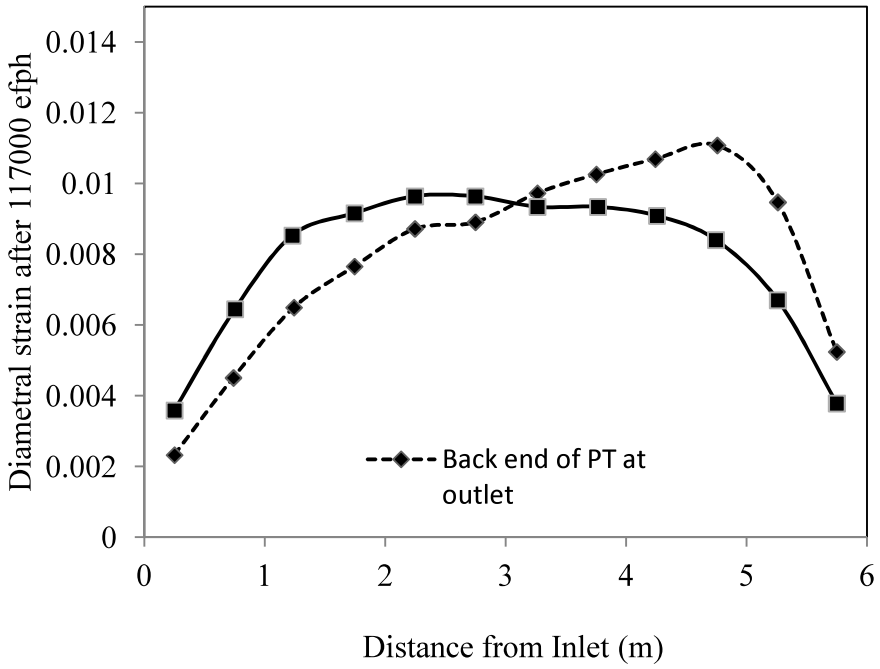

Figure 2.8: Diametral strain observed along the length of the pressure tube in a PHWR reactor for two conditions (i) backend of PT at outlet (ii) backend of PT at intlet

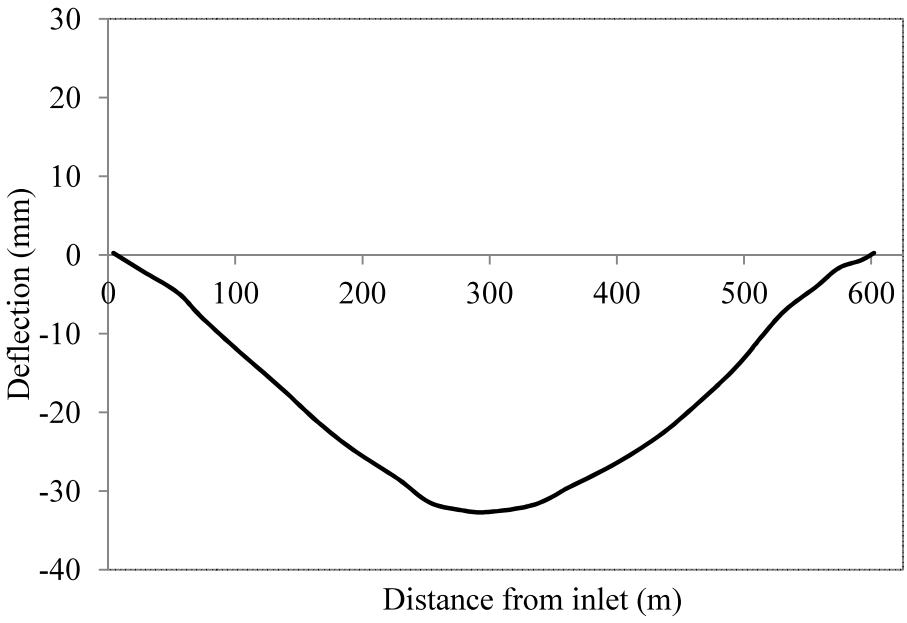

Figure 2.9: A typical observed value of the sag along the length of the pressure tube.

shown better diametral dimensional stability. The strain rate measured during in service operation of pressure tube having different Ft-Fr value is shown in Figure 2. 10. Higher the Ft-Fr value lower is the diametral creep rate. From the reactor operations it is found with increase in the grain thickness the diametral strain was found to decrease as shown in Figure 2. 11. The combined effect of the grain thickness along with the texture on diametral starin is shown in the Figure 2.12. It can be seen that diametral strain is considerably lower for the pressure tubes which have higher grain thickness and lower Fr values. These microstructural and textural features essentially depend on the manufacturing process of the alloy. The variability in the microstructure and texture along the length of the pressure tube introduced during their fabrication leads to the variability in the dimensional change during service of the tube [7, 9, 16].

It is also reported that thermal decomposition of the β_{Zr} phase is a key factor in total dimensional change in the pressure tube. The alloy chemistry and trace elements content have been also found to play important role on the mechanical properties and life of the tube. In Zr-2,5 Nb alloy, Nb has low diffusivity rate and high solubility which is expected to enhances the creep resistance of the alloy. Oxygen and iron are two important elements in the alloy. Oxygen segregates in the β phase and increases the hardness of the material and improves the creep resistance. It was reported that Fe was largely associated with the β-phase and it influences significantly self-diffusion coefficients in α zirconium matrix. It I s observed that Fe decreases the axial creep rate.

The variability of irradiation creep and irradiation growth during the service of the pressure tube has been also a major subject of interest due to its immense effect on the operational limitations. The effect of this variability can be seen in the figure 2. 8. The corrosion resistance of the pressure tube, mainly hydriding and oxidation rate, also depends strongly on the microstructure and texture of the tube [10, 69].

The individual effect of the three deformation mechanism has been relatively understood. However, study of the combined effect of stress, neutron flux and fluence, temperature, and the microstructure of the material is much more complex. There have been several efforts to model the dimensional changes of the pressure tube. Some of the earlier work has predicted the in-reactor behaviors for irradiation creep and growth [14]. However,

this model could not predict accurately as with aging the material properties and stress conditions changes continuously in the reactor. These models have been shown to be accurate for narrow range of textures and microstructures corresponding to certain stage of the pressure tubes presently in reactor.

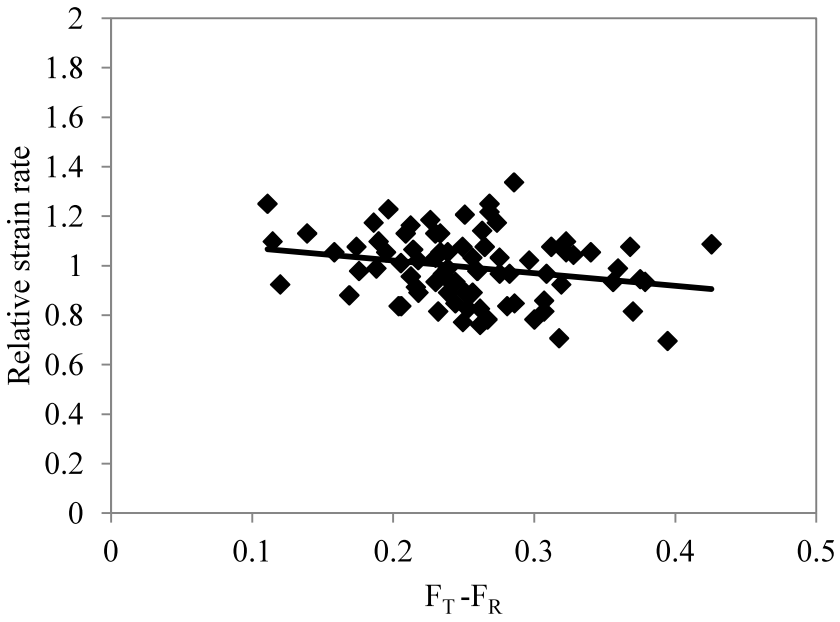

Figure 2.10: The strain rate measured during in service operation of pressure tube having different Ft-Fr value.

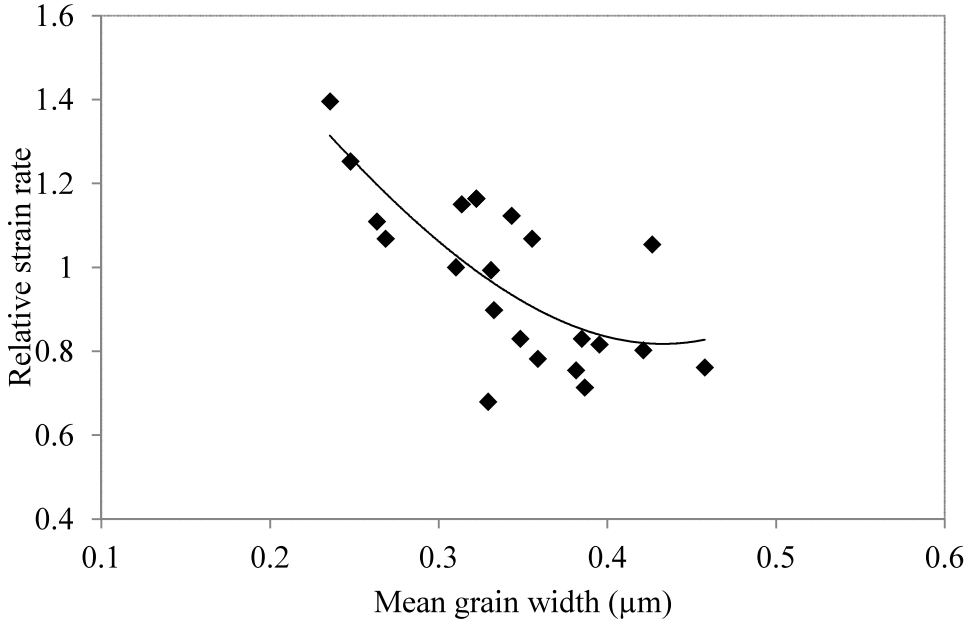

Figure 2.11: Variation of diametral strain with grain thickness of the alpha phase.

There has been continuous efforts towards improving the resistance to irradiation induced creep and growth through the modification of the microstructure of the pressure tube material to achieve longer life of the pressure tube in next generation reactors. Many researchers have studied the change in microstructure and its effect on the properties by altering the conventional route of pressure tube fabrication.

2.6. Fabrication of Zr-2.5Nb alloy Pressure tube

Generally, Zr-2.5 Nb alloy is used in cold worked condition in CANDU type pressurized heavy water reactor. However, in RBMK and FUGEN type reactors, Zr-2.5Nb alloy pressure tube is used in heat treated condition [8].

The typical fabrication routes employed by Canadian and Indian pressure tube manufactures are shown in a schematic Figures 2.13. and figure 2.14 respectively. Zr-2.5Nb

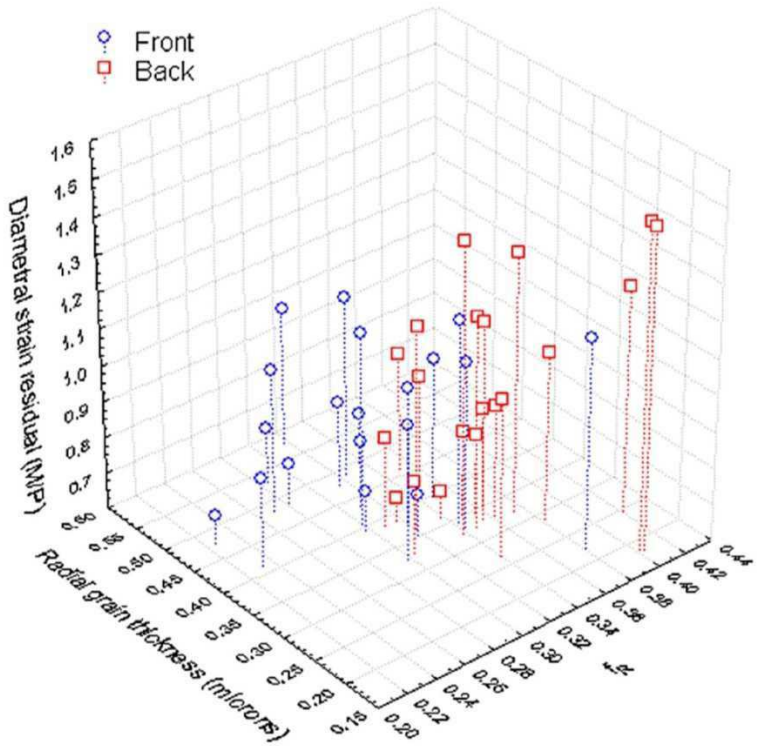

Figure 2.12: The combines effect of the grain thickness alongwith the texture on diametral strain

alloy ingots are made by a quadruple arc-melting process from Zr sponge and master alloys by vacuum arc melting. In Canadian route the cast structure is broken by two steps forging process first press forging is carried out after preheating ingot in beta phase at 1015°C temperature from 590mm dia to 360mm dia and Second rotary forging is carried out in two phase region by preheating to 800°C to 210mm dia billet size. The Indian route was following single stage extrusion process in two phase region (800°C) from 360mm dia cast ingot to 210 mm dia billet. These billets are machined to make hollow billets which are subsequently water quenched from the temperature 1015°C. The beta quenching is done to obtain homogenization with respect to composition, texture and microstructure. In Canadian route the quenched billets are hot extruded with an extrusion ratio of 10.5:1 at about 815°C where as Indian route was following lower extrusion ratio of 7.5:1 at about 815°C. In the CANDU route the tubes are cold drawn in two stages giving 25-30% cold work to achieve the final dimensions [6]. In Indian route instead of cold drawing, two stage pilgering with intermediate annealing was carried out to achieve the final dimensions. In the first stage of pilgering 55% cold work is given and after annealing at 550^{o}C for 3h in the second stage of pilgering 20-25% cold work is given. In the final stage of fabrication autoclaving at 400^{o}C for 24 h is carried out to form an adherent oxide layer and also to relieve residual stresses.

In these reactors it was shown that desired properties could be achieved through proper heat treatment of Zr-2.5Nb alloy tubes. However, it generally involves a relatively complex heat treatment process (Figure 2.14) which some time makes them difficult to achieve specified properties uniformally. It requires precise control of solute temperature and cooling rate during quenching or ageing process. Therefore, the heat treated pressure tubes have not been used extensively in PHWR reactors. TMT-2 material also had good diametral creep resistance in-reactor, attributed to both its texture and grain structure. The other three materials had similar creep resistance controlled mostly by their texture.

The typical manufacturing process of heat treated pressure tubes of the RBMK and Fugen reactor is shown in Figure 2.15. RBMK 1500, Ignalina 1 had used process (TMT-1) where material was quenched from the (α+β)-Zr phase into water follow by cold-working consists of α'-phase and between 10 and 20 % of untransformed α-phase where as RBMK 1500, Ignalina 2 used process (TMT-2) where material quenched from the (α + β)-phase into argon-helium gas mixture followed by cold-working consists of Widmanstätten α-phase and untransformed α-phase.

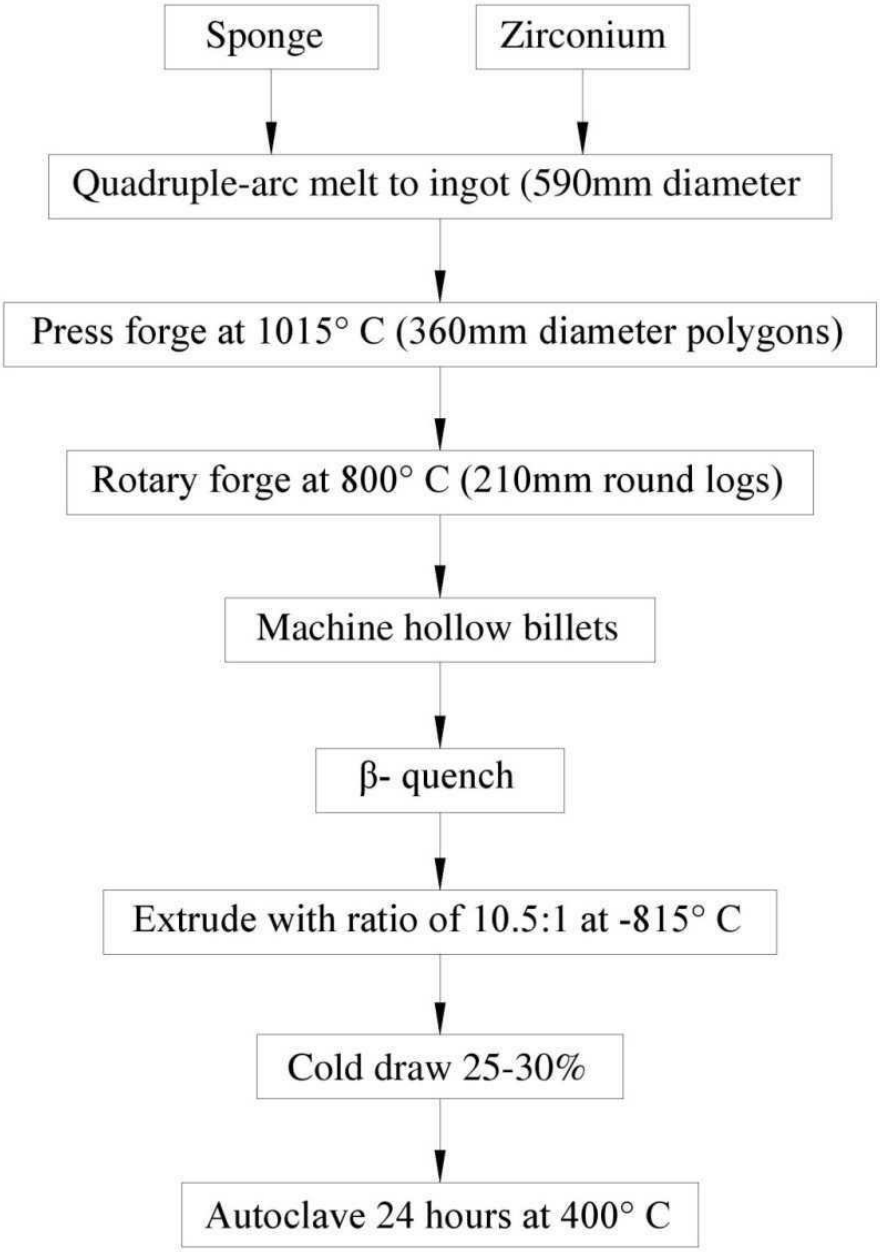

Figure 2.13: The fabrication flowsheet for manufacturing of CANDU PHWR pressure tubes

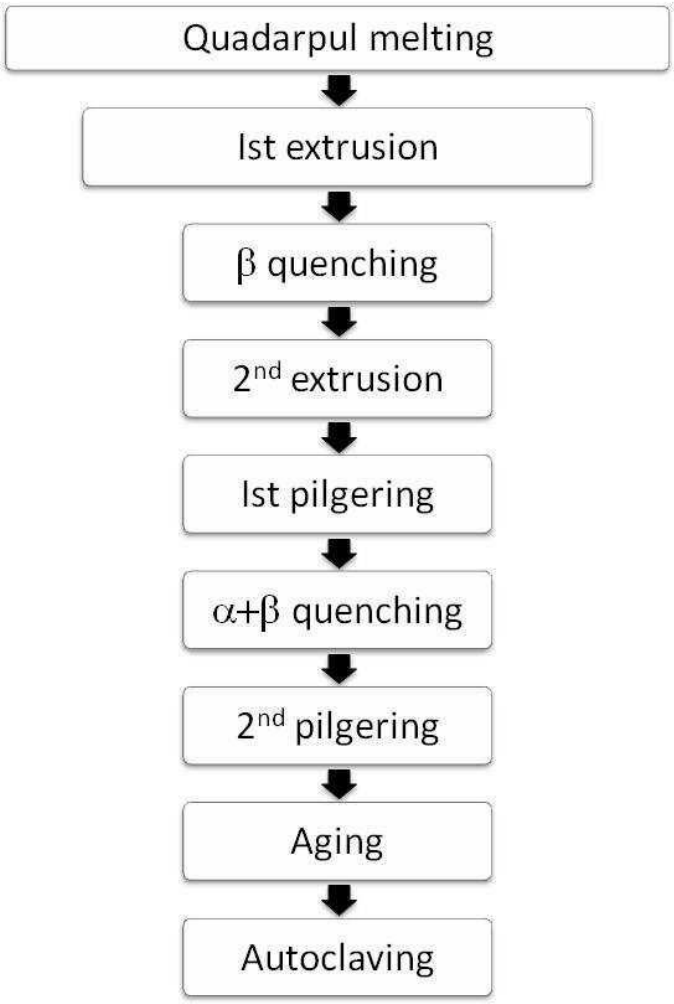

Figure 2.14: The fabrication flowsheet for manufacturing of Indian PHWR pressure tubes

The billet of Zr-2.5 wt% Nb is extruded in a horizontal extrusion press, cold-drawn and then solution-heat treated by quenching the material from the heating furnace (887^{o}C) into water. This solution heat treated pressure tubes are called heat-treated (HT) pressure tubes. After the solution heat treatment the material is cold drawn up to the cold working degree of 5-15%. Then the material is aged in a vacuum furnace at 500^{o}C for 24 h. The typical dimension of the Fugen pressure tube is with inner diameter of 117.8 mm, thickness 4.3 mm and length about 5500 mm.

The chemical composition of HT Zr-2.5 wt% Nb pressure tube is given in Table 2.1.

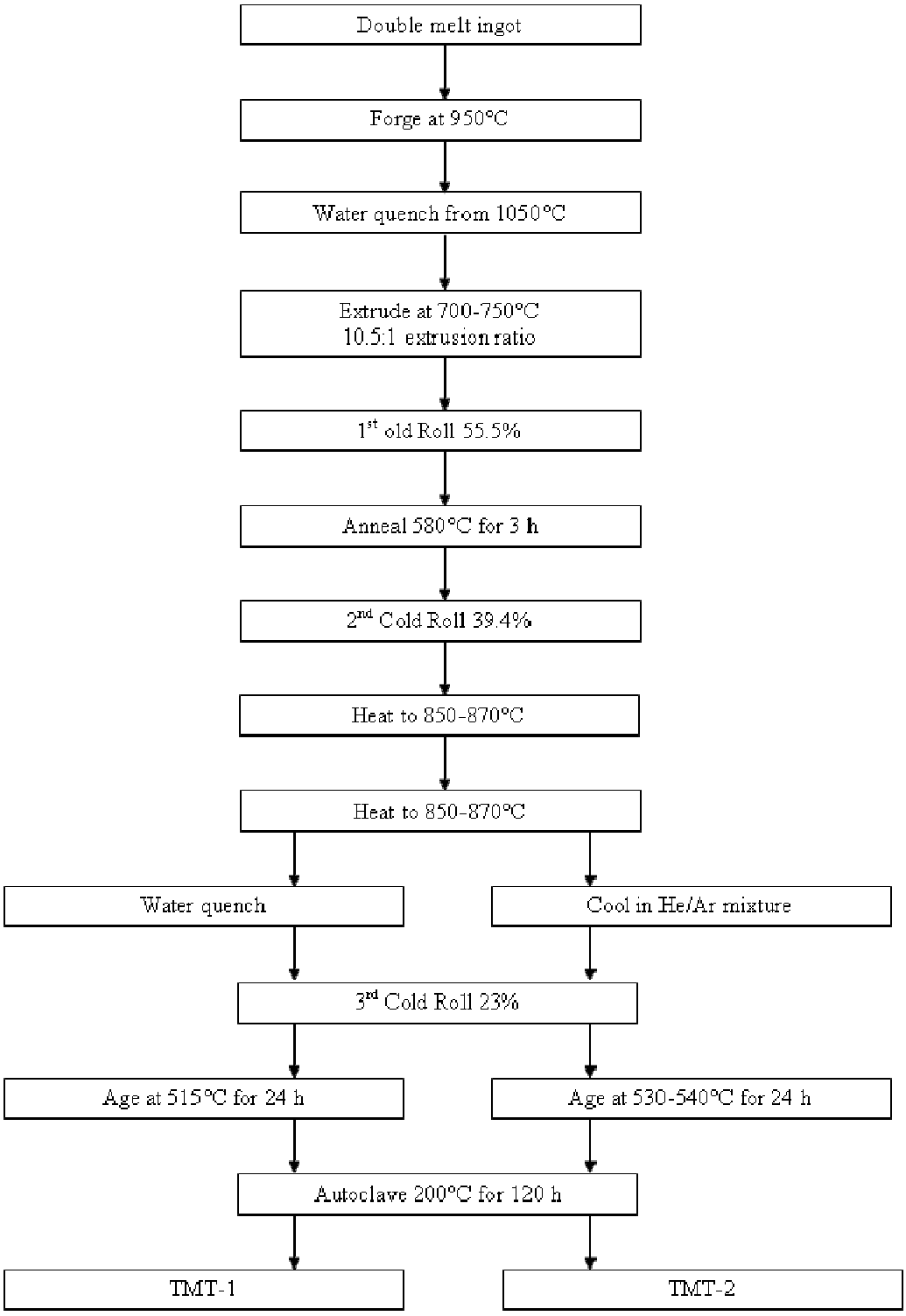

Figure 2.15: Fabrication flow sheet for manufacturing of pressure tube by heat treatment route(a) TMT1 (b) TMT2.

2.6.1. Evolution of microstructure during manufacture of Zr-2.5Nb pressure tubes

The fabrication of pressure tubes involves a large number of thermo-mechanical treatments, and the final microstructure thus developed determines the long-term and short-term properties of these tubes [6, 7, 70-72]. The evolution of microstructure and texture in Zr-2.5 Nb alloy pressure tube as a function of thermo-mechanical treatment and during their fabrication has been studied by several workers in great detail [6, 30, 71]. Therefore, it is important to understand the influence of each of these fabrication steps on crystallographic texture and microstructure in order to optimize the pressure tube fabrication flow sheet. There has been continuous effort towards improving the resistance to irradiation induced creep and growth, through the modification of the microstructure of the pressure tube material [6, 16].

Table 2.1: Typical Composition of Zr-2,5Nb alloy pressure tube

Element	Composition (wt%)
Nb	2.5-2.8 %
O	1100-1400 ppm
Fe	900-1300 ppm (alloying element)
C	40-80 ppm (alloying element)

Microstructure of cold worked Zr-2.5Nb pressure tubes

The Specific detail of the evolution of microstructure during their fabrication has been presented in this section. The forged or extruded billet microstructure normally show coarse α widmanstatten type of microstructure in which β phase is present at α/α interfaces. The β-quenched structure in Zr-2.5 pct Nb tubes consists of lath as well as plate martensites in which three distinct types of morphologies exist. These are large primary martensite plates which are occasionally internally twinned, fine secondary martensite plates arranged in self-accommodating groups, and martensite laths stacked almost parallel within a packet. Similar microstructure is reported for both types of fabrication routes [6, 52, 73].

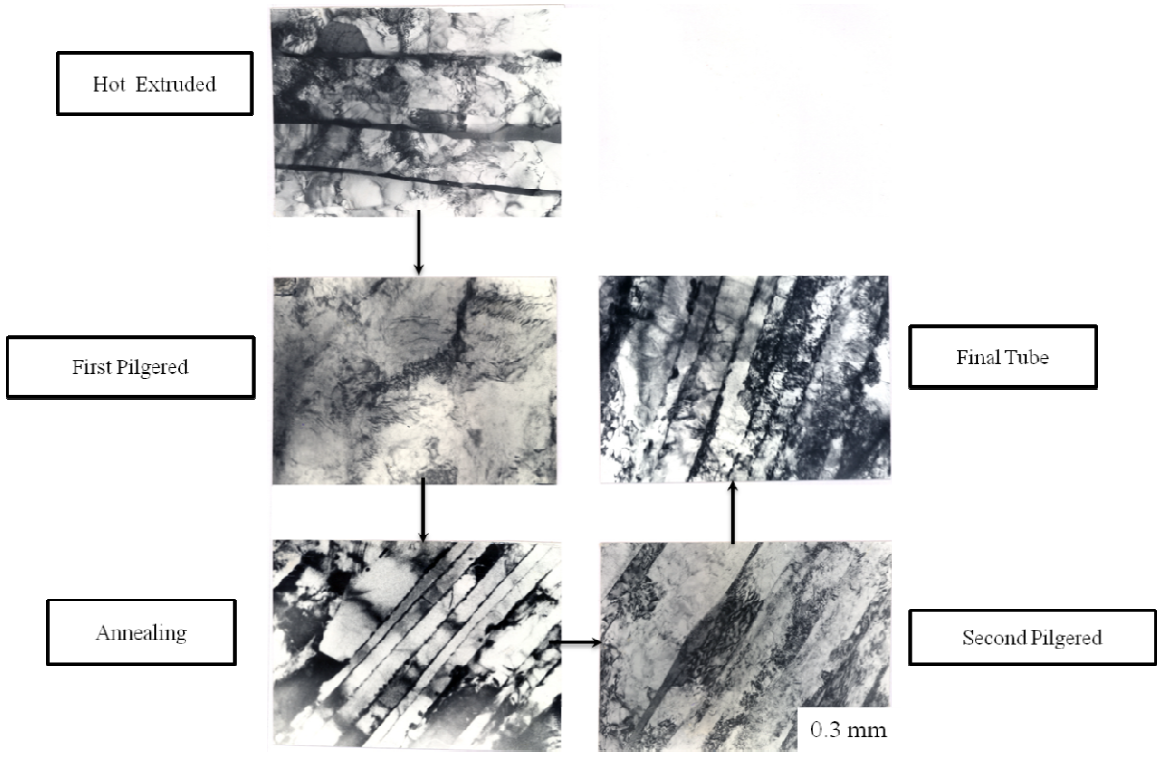

Figure 2.16: The evolution of microstructure during fabrication of Indian PHWR tube.

A typical microstructure of the extruded Zr-2.5Nb consists of about 90% α_{Zr} and ~10% β_{Zr}. Nb content is partitioned between the phases such that the predominant α phase has a Nb content less than 1wt%, while the β-phase contains ~20wt% Nb. The volume fraction of the β phase is higher and the niobium content is less in case of Indian route. During hot extrusion, the α and β phases dynamically recrystallizes and gives rise to thin and platelet-like shaped α grains that are mostly elongated in the axial direction and flattened in the radial direction with an aspect ratio in the range of 1:5-10:20-40 in the radial, transverse and axial axes of the tubes, respectively. The aspect ratios of both phases are much smaller in case of tubes produced by Indian fabrication route. The β phase is sandwiched between α stringers. The ω-phase precipitates within the β during cooling of the hot-extruded tubes following either processing route.

In Canadian route during cold drawing α grains gets further elongated and increases the dislocation densities substantially. <a>, <c> and <c+a> type have been reported. Griffiths et al. [7, 8] reported that the finished tubes produced by Canadian route usually contain a mixture of <a> and <c> component and dislocations density of the order of $1\times10^{14}m^{2}$, respectively.

In the Indian route the first pilgering operation further elongates both α and β microstructures and aspect ratio of the α grain increases marginally. Fragmentation of the β stringers also occurred due to the heavy cold deformation. TEM observations revealed a very high dislocation density within the α stringers. The purpose of the intermediate annealing treatment prior to the second pilgering in Indian route was to annihilate all the cold work introduced in the first pilgering step. During the annealing treatment, static recrystallization of the two phases occurs. Additionally, in several regions continuous stingers of β phase gets globulized. It is found that optimum annealing treatment (550°C ~ for 6 hours) retains the elongated morphology of the two phases produced in the hot extrusion step. 20 to 25% cold work introduced in the final stage of fabrication produces a dislocation density of about $2.5x10^{14}/m^2$. Figure 2.16 shows the evolution of microstructure during different stages of the fabrication of the pressure tube.

Autoclaving of the tube decomposes β_{Zr} further towards the equilibrium α_{Zr} and β_{Nb} increasing Nb content. In final pressure tube, the predominant α phase retains it lamellar shape while the β phase is distributed more or less continuously between the α microstructure of the pressure tube material grains [74].

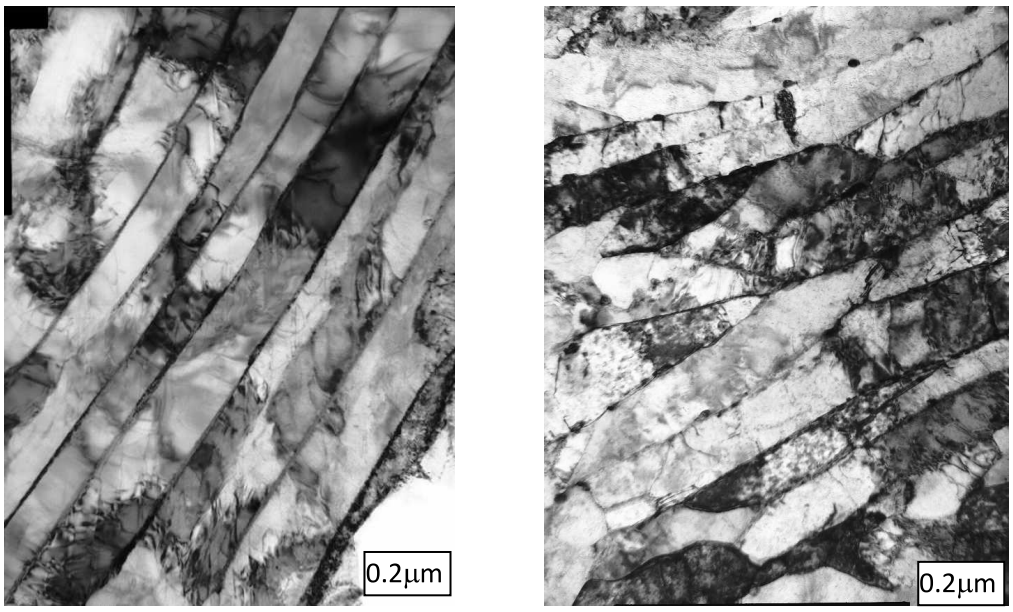

Figure 2.17: : The final microstructure of the Indian and CANDU pressure tube material

Similar observations have been made in the tube produced by Indian route however, β phase is discontinuous in many regions and spherical β phase is observed showing much higher Nb content. The α phase is also not as lamellar and aspect ratio is also smaller in the finished pressure microstructure. The final microstructure of the Indian and CANDU pressure tube is shown in Fig. 16. Formation of the ω phase within the β phase has also been reported in the final autoclaved tube.

Zr-2.5% Nb alloy heat treated Pressure Tube

Heat-treated 2r-2.5 Nb pressure tubes are water quenched from the α+β phase, cold worked about 12% and then aged at 500°C. This produces a microstructure that consists of about 90% martensitic α'and 10% equilibrium α grains. After the water quench, the martensitic α' is supersaturated in Nb. The subsequent cold work and aging treatment results in a small amount of recrystallization and small βNb precipitates are formed. The martensitic α' has a relatively random crystallographic texture and hence the properties of heat treated tubes are much more isotropic than cold worked tubes.

Compared to cold worked tubes, there is much less information on heat-treated pressure tubes that have been tested after service in reactors. In general, their tensile strength is higher, their ductility, corrosion and hydriding, fracture toughness and susceptibility to DHC are similar, their axial elongation is much less but their diametral expansion is slightly higher.

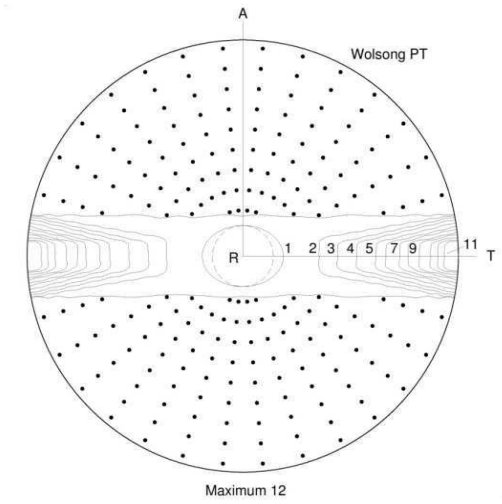

Figure 2.18: A typical basal pole texture obtained in the cold worked pressure tube

2.6.2. Evolution of crystallographic texture in Zr-2.5Nb pressure tubes

A typical basal plane (0002) pole figure of CANDU pressure tube is shown in Figure 2. 18. It shows majority of {0002}, {1120} and {1010} basal plane normals oriented in the

transverse, radial and axial direction respectively of the tube. The CW and TMT-2 tubes have a higher proportion of grains with basal plane normals in the transverse direction, F^T of 0.52 to 0.57, than in the radial direction, FR of 0.38, while quenched and annealed materials (TMT-1 and CW-A) have similar values of F^T and F^R, about 0.38 in quenched materials and 0.41 in annealed materials.

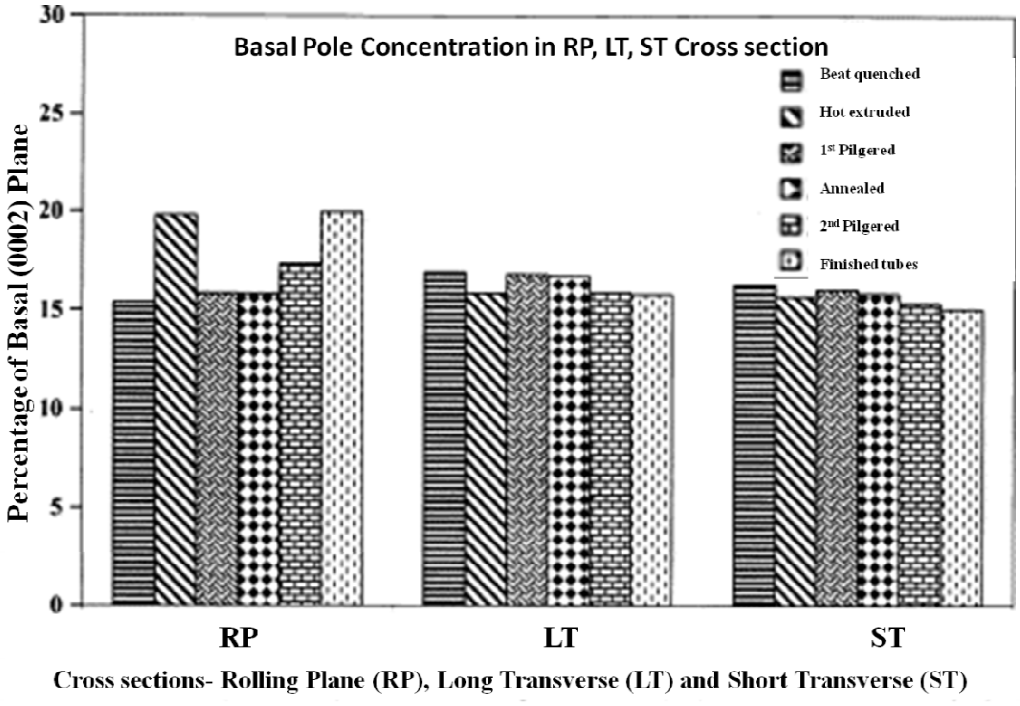

Figure 2.19: The evolution of texture during different stages of pressure tube fabrication (Cross sections Rolling Plane (RP), Long Transverse (LT) and Short Transverse (ST)

The strong (0002) texture of typical CANDU pressure tubes results in good transverse tensile strength and low circumferential strain due to irradiation creep [16]. It is reported that such texture however shows higher axial irradiation creep and growth and not favourable for delayed hydride cracking (DHC) [75-77].

The final crystallographic texture of cold work pressure tubes is predominantly established during extrusion [52, 78]. The subsequent cold drawing and stress relieving in the Canadian route does not modify texture significantly. Kiran Kumar et al have measured the texture at different stages of fabrication of the pressure tube and have shown that tubes produced by Indian route show marginal modification in texture both after pilgering as well as intermediate annealing [70, 79] (Figure 2.19). Earlier they have shown that in Zr-2.5Nb, two phase material, majority of deformation during cold working is experienced by the beta phase and no effective deformation occurs in the α phase Figure 2.20. The α plates experiences only in plane rigid body rotation align itself in the rolling direction [42].

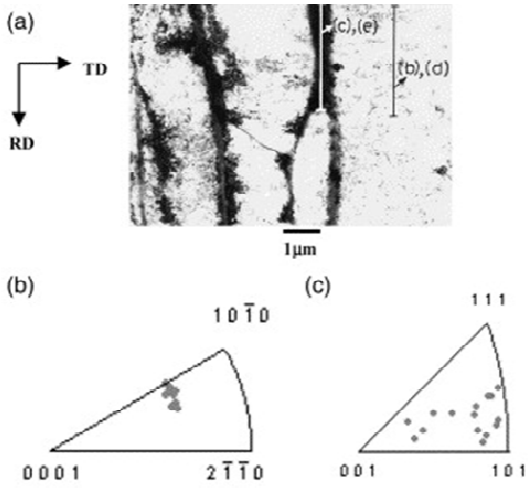

Figure 2.20: Development of lattice strain in the alpha in presence of beta phase

The influence of extrusion parameters on the development of texture of Zr-2.5Nb tubes Extruded in the α+β phase field has been reported by Holt et al [52], [80], [81].. There study has shown that increase in extrusion ratio decrease basal pole intensities in radial direction and increases in the transverse and axial direction (Figure 2.21(a)). The increase in extrusion temperature also results in increase in basal pole texture to larger extent in transverse direction and to lesser extent in the axial direction at the expense of the radial basal pole texture (Figure 2.21(b)).

Holt and co-workers have explained mechanism of texture development as a function of extrusion temperature and extrusion ratio [78]. The volume fraction of the α and β phase and the operating deformation mechanisms in different temperature regime and state of stresses influences development of texture in αZr and bulk textures of Zr-2.5Nb extruded tubes. This in turn decides the dominant texture in the extruded product.

During extrusion temperature drop occurs from the start to finish of the tube. The radial basal texture increases and axial basal texture decreases from the front end to the back end. As well, the grain size gradually decreases from the front to the back end. The variation in texture along the tube results in variation in properties and in-reactor performance of the tube [82]. There have been several efforts to modify the manufacturing process to eliminate or minimize the variation in texture in the tube.

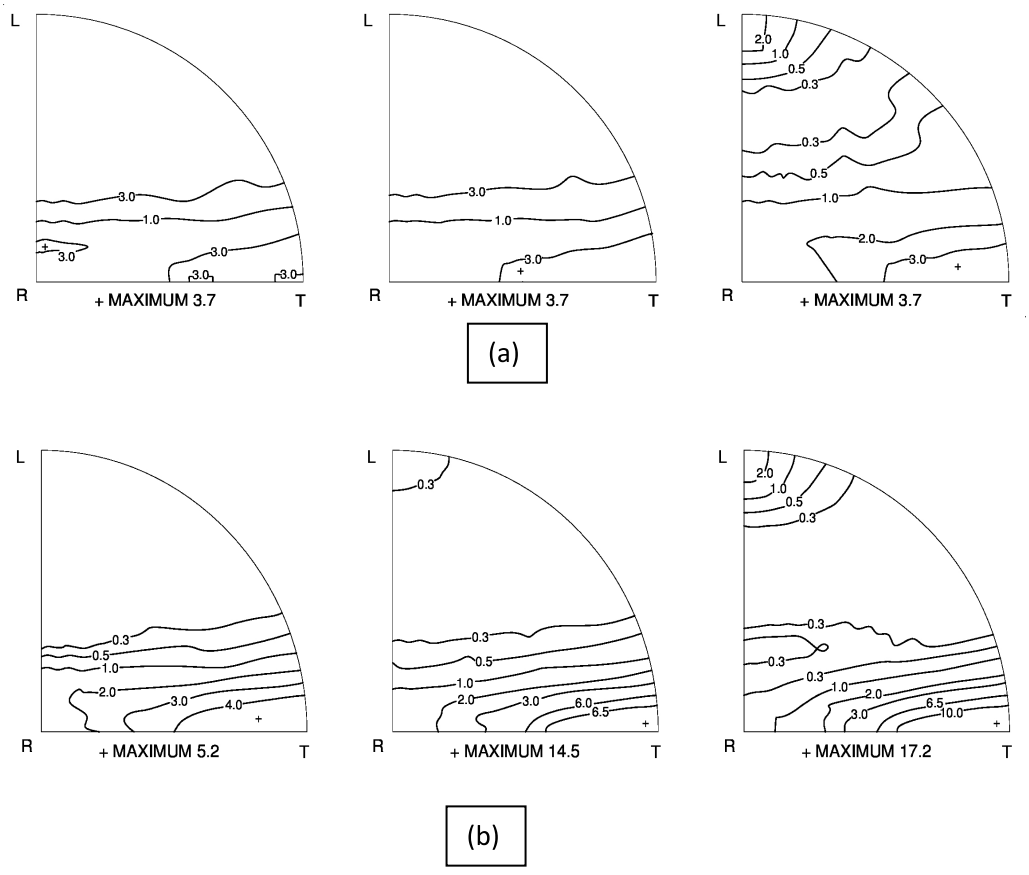

Figure 2.21: The change in the transverse texture with increase in (a) extrusion ratio (b) extrusion temperature

The microstructural features such as a grain morphology and the dislocation structure and density also plays important role in the development of the texture in Zr-2.5Nb alloy tubes.

2.7. FEM Simulation of Hot extrusion of Zr-2.5Nb alloy pressure tube

The morphology and distribution of the alpha and beta phase get greatly influenced during this hot extrusion stage [21, 22]. These microstructural and textural features are influenced by the actual temperature and stress distribution during the hot extrusion process. In addition, extruded product quality in terms of variation from leading end to tailing end, surface cracks, ovality, etc also depend on the presence of steep temperature gradients during the hot extrusion [78, 83]. Hence a detailed knowledge of the role of process parameters such as billet preheat temperature, extrusion speed, extrusion ratio etc on the temperature and stress distribution during the hot extrusion process can help tailor the process. However, the design and control of the experiments to acquire such information during hot extrusion process is rather difficult. An alternative approach could be application of computational / numerical analysis of the extrusion process for the process optimization. In the recent past the three-dimensional finite element analysis for hot extrusion is being pursued in case of aluminium based materials [84-86]. Such studies in case of the Zr based alloys seem to be rather limited in the open literature, forming the motivation to present study.

Arbitrary Lagrangian Eulerian FE formulation and 8 noded Hexahedron types of elements, which have shown great potential in the finite element methodology of metal forming, were used for the current study. Some of the key parameter of the extrusion process such as ram velocity, billet pre-heat temperature, fillet radius and reduction ratio, have been studied for their role in determining the overall temperature distribution during hot extrusion, requirement of ram force etc.

Chapter 3

Experimental Methods

3.1. Thermo-mechanical Process for Fabrication of Pressure Tubes

3.1.1 .Melting of Zr-2.5 Wt% Nb Alloy:

Zr-2.5 wt% Nb alloy ingots were prepared by consumable vacuum arc melting process (VAR) [87, 88]. The entire ingot making includes- compaction of sponge along with alloying elements in desired proportion, preparation of consumable electrodes using electron beam welding technique and finally vacuum arc melting. Zirconium sponge being the major input material for melting, desired chemistry of sponge was selected in terms of Hf, C and O content. Zirconium sponge was mixed with major and minor alloying elements as Nb and minor Fe respective in required proportion. Oxygen (1100-1400 ppm) being another major alloying element in the Zr-2.5 wt% Nb alloy was mainly achieved by selection of Zr- sponge itself with relatively high oxygen content.

Figure 3.1: Quadruple melted Ingot by VAR melting method

For better homogeneity, reduced surface and subsurface defects and most importantly to remove critical gaseous impurities particularly (H< 5 ppm, Cl< 0.5ppm, P<10 ppm) quadruple melting was carried out. The sufficient numbers of cylindrical compacts are made of sponge and alloying elements were stacked together and welded along the length and used as consumable electrode in the VAR. The primary melted electrodes were assembled, welded

together and remelted into bigger diameter crucible. Finally, the quadruple melted Zr-2.5wt% ingot of 350 Ø mm and 550Ø mm was produced (Figure 3.1). The ingots were subjected to ultrasonic testing on complete volume [89]. Also, the samples from ends of the ingot were collected in the form of turnings for comprehensive chemical analysis (table 3.1)

Table 3.1: Typical composition of the Zr-2.5Nb alloy ingot

Element	**350 Ø mm (Wt%)**	**550 Ø mm ingot (Wt%)**
Niobium	2.50	2.72
Oxygen	1126 ppm	1238
Iron	645 ppm	1130
C	60	71

3.1.2. Forging of Zr-2.5wt%Nb Ingots:

Forging process was used in primary breakdown of cast structure in the quadruple melted Ø350mm and 550mm ingots. Further two different forging methodologies [90] were employed for forging of ingots viz. press forging and radial forging. Both these processes are essentially open die forging however defer in state of applied stress due to application of single or multiple dies during forging. Forgings were carried out to achieve rods of final diameter of 230mm. the selection of final forging diameter was based on the possibility to produce hollow billets for pressure tube blank production. Ingots were preheated in a 70KW resistance heating furnace under the controlled atmosphere to minimize surface oxidation.

Press Forging

A PAHNKE make two pull down type 1500 T hydraulic forging press was used for press forging of starting ingots of Ø 350mm and 550mm. The forging process was essentially completed by holding the preheated work piece in a manipulator jaw and placing it on the stationary curved anvil. The upper die moves up and down at a predetermined speed imparting controlled deformation on outer diameter on each downward stroke. During the each upward stroke the manipulator rotates the ingot essentially to cover deformation the entire cross section.

The 350 mm dia was preheated at 950^{o} C and soaked for 4-5 Hrs before press forged to 230 mm dia with overall forging ratio of 2.3:1 in a number of forging passes without any intermediate reheating. The conversion of Ø550mm diameter to Ø 230 mm was carried out in two stages of forging with an intermediate reheating. The first stage press forging from Ø550mm to Ø 350mm with forging ratio of 2.5:1 was carried out on preheated ingot soaked at 1015^{o} C for 5-6 Hrs. In the second stage the same ingot was reheated to 815^{o}C for 4-5 h before forging to final diameter of 230mm.

The forging was carried out at a forging speed of about 100mm/sec with reduction per pass varying from 30 mm/pass in initial stages to 20 mm/pass in final stages of forging. The strain rate throughout the press forging was maintained in the range of 0.30 to 0.40 per sec.

Radial Forging

The present radial forging were carried out on a GFM SX-65 type machine with a capacity of 1540T as shown in figure 3.2. The deformation in radial forging results from a large number of short strokes at high speed by four hammer dies arranged radially around the work piece. In addition, during forging the work piece was rotated to obtain a forged product with good surface finish.

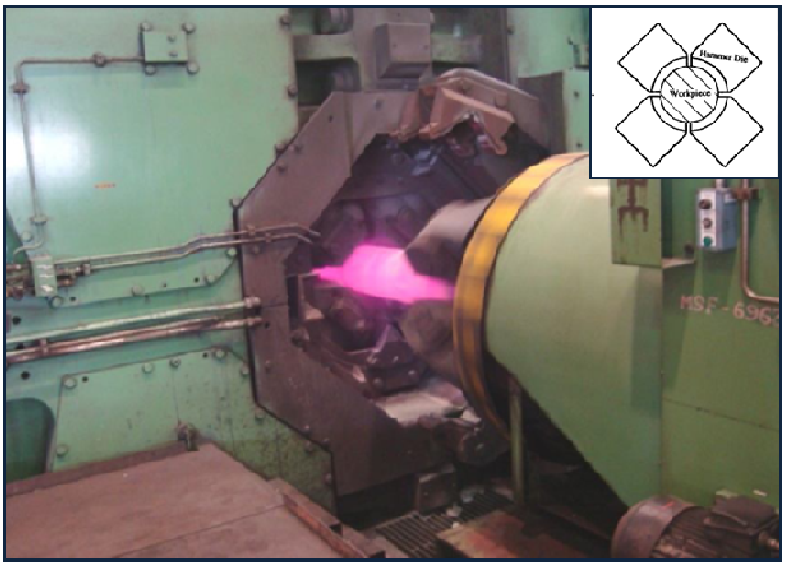

Figure 0.2: Radial forge press machine used to forge from (i) 550 dia to 330 mm dia and (ii) 350 dia to 230 dia billet

Radial forging were only carried out for ingots of Ø550mm. Similar to the press forging mentioned above, here also the two stages radial forging was carried out essentially maintaining the corresponding temperature for preheating and soaking time as well as

reduction ratio(i.e 1st stage forging to Ø350mm and 2nd stage forging to Ø 230 mm, figure 3.3). The overall forging ratio in case of double forging was equal to 5.7:1. The mean effective strain rate was varied from 0.2 to 0.85 per sec in the deformation zone of the dies based on the input diameter in each deformation pass.

Finally all the forged ingots of 230 mm diameter were cut into equal length and subjected to OD machining and deep hole drilling to provide inner diameter of 30mm followed by hot expansion to obtain requisite dimension of hollow billets. Expansion was carried out on 1200T vertical hydraulic expansion Press (VEP) where a preheated billet to 750 - 800^{o}C and moved inside vertical container. A nose cone tool was passed through the ID to enlarge to 104 mm. During the process the OD essentially remained constant while length increased in proportion to maintain the volume constancy. The schematic of the expansion process has been shown in fig 3.4.

Beta quenched billets were then machined on OD and ID surfaces upto Ø 217mm and Ø 112mm respectively to remove surface oxide and imperfections. This was followed by ultrasonic testing for flaw detection.

Figure 3.3: 230 mm diameter double stage radially forged zr-2.5Nb alloy ingots

3.1.3. Extrusion of Zr-2.5Nb alloys

In this study process of extrusion was used primarily for two purposes. First extrusion was employed as a primary breakdown of ingots and secondly for producing tubular blanks which were used as preform for fabrication of final Zr-2.5Nb pressure tubes.

The ingot was preheated at 800^{o} C for 3 h and extruded with an equivalent extrusion ratio of 2.3:1 and mean strain rate of 1.2 to 1.5 per sec. The copper coated ingots were placed into the preheated extrusion container and forced through the conical die (semi die angle 60^{o}) of 230mm ID. Primary breakdown of the ingot was carried out on 3780T hydraulic horizontal extrusion press shown in Figure. 3.5 (a) (HEP) [21, 22].

In case of hollow extrusion, the hollow beta quenched billets were jacketed in seamless Cu tube. These billets were preheated and soaked at 815^{o}C for 2.5 to 3 h before final extrusion to

blanks. In the present study extrusion into tubular blanks were carried out for two different extrusion ratios. Tubular extrusion of 133mm OD X 9mm Wall thick tube

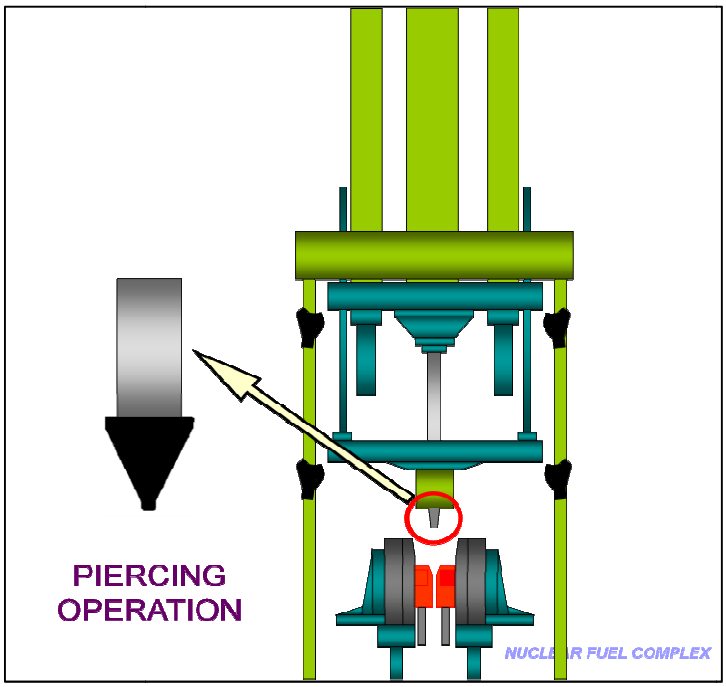

Figure 3.4: Schematic of Piercing Operation of the billet for extrusion of blanks

was carried out with extrusion ratio of 7.3:1 whereas ER of 12.75:1 was employed for extrusion to 119mm OD X 6mm Wall thick tube (Figure 3.5 (b). Extrusion ram speed was maintained in the range of 40-50mm/sec. Tubular extrusions were also carried out in a conical die with half die angle of 45^{o} to avoid the formation of dead metal zone in the container which could lead to shearing and tearing of Cu jacket. Cu -jacketing from the extruded tubular blanks were removed thoroughly by dissolving into 60% conc. HNO_3.

3.1.4. Heat Treatments

β Quenching

All the hollow billets prior to hot extrusion were subjected to *β* quenching. The billets were heated at 1000^{0}C temperature for 30 min followed by quenching into water.

Stress-Relief annealing

The hot extruded blanks were stress relieved in Horizontal Vacuum Annealing Furnace at 480^{0}C for 3 hrs (figure.3.6).

α+β quenching

During fabrication of heat treated pressure tube *α+β* quenching was performed on hot extruded blanks. The blanks were soaked in *α+β* region in vacuum at 860°C to 890°C for 30 min and subsequently they were either gas quenched or water quenched.

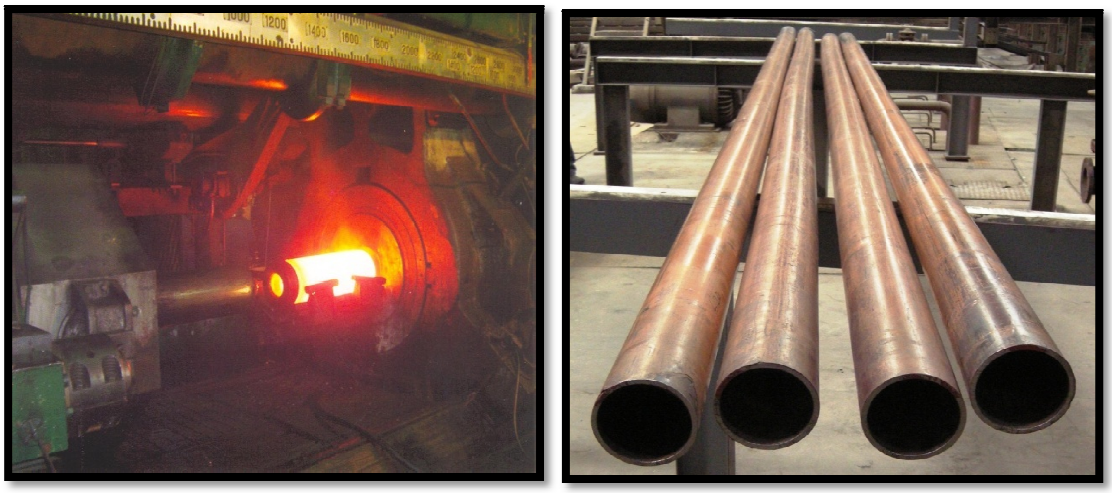

Figure 3.5: (a) Horizontal hot extrusion press (b) Hot extruded Zr-2.5Nb alloy blanks

Ageing treatment

The *α+β* quenched and further cold deformed samples were aged at 420°C and 450°C for different duration in a vacuum furnace.

Intermediate vacuum annealing

In the case of fabrication of cold worked pressure tube an intermediate vacuum annealing was performed at 550^{o}C/6h between the two successive pilgering passes. The aim of this annealing was to restore the ductility of the tube.

Autoclaving

Pilgered pressure tubes were autoclaved in an enclosed chamber having pure steam atmosphere completely free of air maintained at 400^{o}C (+/-15^{o}C) for a period of 36 h. The autoclaving of the tubes were aimed to achieve a continuously uniform black or dark gray impervious and adherent oxide layer.

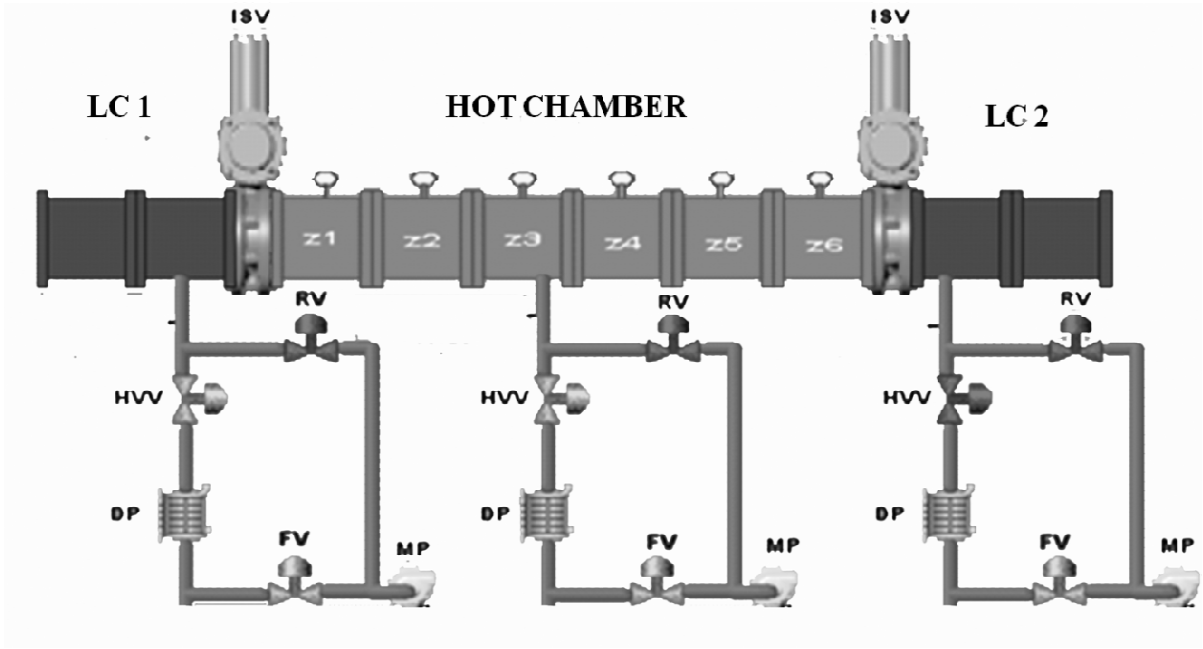

Figure 3.6: Horizontal Vacuum Annealing Furnace and its Schematic representation

3.1.5. Cold Pilgering

In the present study pilgering was employed as cold working method for reduction of OD and WT of tubular blank preforms produced by hot extrusion. These blanks after stress relieving were pilgered on 150 VMR pilger mill. The outside diameters, inside diameter and wall thickness of tubes were simultaneously reduced over the working length under a pair of dies with semi-circular tapered grooves cut on them. A tapered mandrel, with a matching contour with the dies, was placed centrally between the grooves, which determined the wall thickness of the reduced tube along the working length.

The effect of cold working was carried out with two different starting size of the extruded blanks and achieving the finished pressure tube dimension of 112.8 mm OD X 103.4 mm ID X4.7 mm Wt. Wherever the input tubular blanks of 133mm OD X 9mm Wt (ER=7.3:1) tubes were taken, final dimension of the pressure tube was achieved in two stage pilgering. The stage pilgering was employed with 55% cross sectional area reduction to achieve an intermediate tube of dimension of 119 mm OD x 6mm Wt. This intermediate tube was given a second and final stage pilgering of 20% cold sectional area reduction to manufacture the finished pressure tube. However an intermediates vacuum annealing at 550^{o} C/ 6h between the two successive pilgering passes was also done with the aim to restore the ductility of the tube.

3.2. Characterization techniques

3.2.1. Sample Preparation for Microscopy

Preparation of Specimens for Optical Microscopy

Appropriately heat treated specimens were first ground on successive grades of silicon carbides paper down to 600 grade. After cleaning the samples were chemically polished and/or etched in a solution containing 50 parts of water, 40 to 45 parts of nitric acid and 5 to 10 parts of hydrofluoric acid. It was noticed that the etching was very uniform with 6 to 7 parts of the hydrofluoric acid.

Samples prepared for optical microscopy could be used directly for X-ray diffraction investigations for phase identification and analysis [61]. The same samples could also be used for scanning electron microscopy studies using the back scattered electron and the secondary electron modes of imaging.

Preparation of Specimens for Scanning Electron Microscopy

Specimens for secondary electron imaging were prepared in a similar manner as that for the optical microscopy specimens. After mechanical polishing samples were chemically polished and/or etched in a solution containing 50 parts of water, 40 to 45 parts of nitric acid and 5 to 10 parts of hydrofluoric acid. In case of back scattered imaging specimens were only polished to the mirror finish by using both mechanical and chemical methods [65].

Preparation of Specimens for Orientation Imaging Microscopy

Coarse grinding was used to produce flat surface for examination and it started with 240 upto 1200 grit SiC. Polishing is used to remove any deformation introduced earlier during grinding and it is done by alumina abrasives and diamond solutions for harder materials. Alumina is used as final polishing medium, however for good EBSD pattern quality colloidal silica was used. Mechanical polishing alone is not enough to produce good EBSD patterns and subsequently electropolishing was used [58].

Preparation of Specimens for Transmission Electron Microscopy

For preparing specimens for transmission electron microscopy (TEM) [63] slices of thickness of about 0.5 mm were cut with a low speed diamond saw from appropriately treated specimens of different alloys. When required, theses slices were subjected to the desired heat treatments. These slices and strips were ultrasonically cleaned, ground on both sides with 320 grit silicon carbide abrasive paper until they were 100-150 μm thick, and then ultrasonically cleaned again. Disc specimens of 3 mm diameter were punched out from the sliced and ground material, followed by thinning by dual jet electropolishing in a Tenupol dual jet electropolisher, using an

electrolyte consisting of perchloric acid (30 parts), n butanol (170) parts, and methanol (300 parts). The thinning was carried out by maintaining the electrolyte temperature at around -40°C and using a voltage of 20 V. Immediately after perforation the discs were removed from the electrolyte and thoroughly rinsed with methanol.

3.2.2. Microscopy Examination of the Specimen

Optical microscopy investigations of the heat treated samples were performed using Carl zeiss and Leika microscopes. Bright field as well as polarized light images were examined.

SEM and OIM were carried out in FEI and JEOL microscopes [91]. Both secondary and back scattered images were obtained in SEM mode. The OIM patterns were obtained by EBSD technique and the patterns were analysed using HKL softwares.

Some of the TEM thin foils were examined in a JEOL 3010 microscope and some others JEOL-2000-FX microscopes operating at 200 kV and 300 kV respectively. Standard electron microscopy techniques like bright and high resolution dark field microscopy, selected area diffraction (SAD), weak beam imaging, etc. were employed. A series of reciprocal lattice sections and standard stereographic projections corresponding to the α(hcp, with a c/a ratio of 1.59) and the β(bcc) phases were prepared in order to facilitate the analysis of the observed diffraction patterns and microstructural features. In a limited number of specimens the composition analysis of the α and the ß phases was carried out by energy dispersive spectroscopy (EDS) in a JEOL microscope.

3.2.3. Quantitative metallography

The volume fractions of the α and the ß phases as well as the thicknesses and the aspect ratios of the crystals of the two phases were estimated by using a digital image processor. The micrographs obtained by various microscopy techniques were grabbed by a solid state video camera and subsequently these images were digitized. For a given micrograph each feature was then assigned a specific grey level. The line intercept method was used to count the different features. The volume fractions of the individual phases were determined on the basis of their differential grey levels.

3.2.4. Sample Preparation and texture analysis by X-ray diffraction technique

The specimens from three principal directions (transverse, radial and axial) of the pressure tube were obtained as shown in Figure.3.7 (a). As the wall thickness of the tube was < 4 mm composite samples were prepared, for the transverse and axial directions. For each direction a

specimen surface area of ~15 mm x 10 mm was prepared. It was ensured that the surfaces of the specimens extracted in three principal directions were perpendicular to the respective reference directions.

The sample pieces obtained from a selected direction were placed closely and mounted using araldite. These mounted specimens were then subjected to metallographic preparation upto the 1000 grit size emery paper using standard procedure and then mechanically polished using diamond paste of 3μm particle size. As a final step these specimen surfaces were chemically polished in 45% HNO_3, 5% HF and 50% H_2O which dissolved a thin layer of ~0.05 mm thickness to produce stress free sample surfaces for XRD studies.

X-ray diffraction [92] studies were conducted for phase identification and analysis by using a monochromated copper K_α radiation in conjunction with a Bruker and a JEOL models. In the present study the crystallographic texture measurements of Zr-2.5%Nb alloy pressure tube samples was determined by Kearns method. The diffraction scans were recorded from the sample surface with 2θ angles ranging from 30^o. The step size was kept at 0.05^o. X-ray diffraction scans for a α-zirconium powder sample (containing randomly oriented particles) was also recorded in the identical manner. Diffraction patterns were corrected for background using the software and the integrated intensity from the 19 reflecting planes as shown in Figure. 3.8 was recorded. The texture parameter $f_{[0002]}$ for the selected direction was determined all the three principal directions.

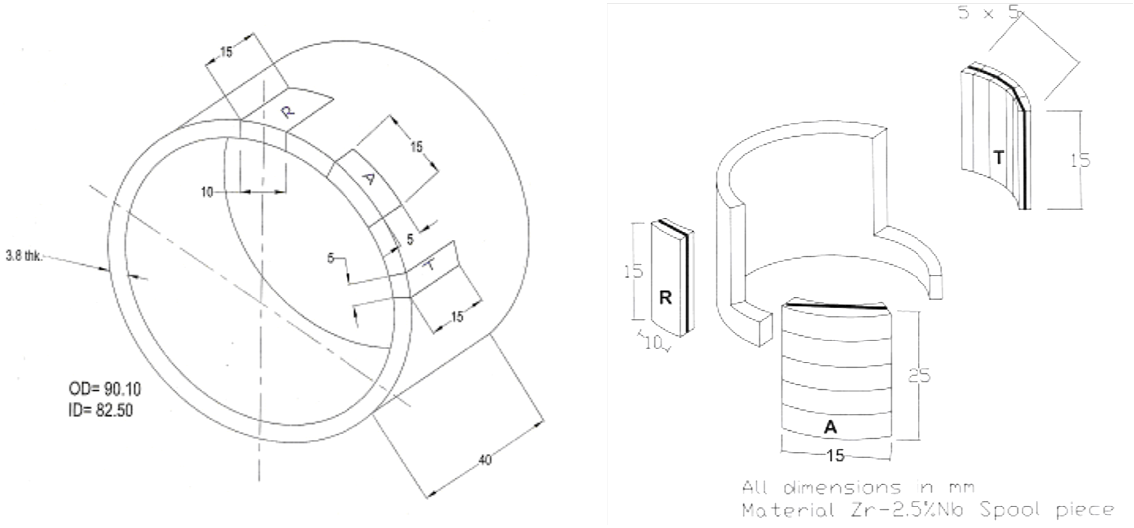

Figure 3.7: Specimen preparation for texture parameter determination by Kearns method. (a) Sample cutting plan to obtain samples from three principal directions from the pressure tube off cut. (b) method for obtaining rectangular flat samples

3.2.5. Mechanical Testing of Pressure Tube:

Samples were cut from leading end and also from trailing end for mechanical testing. The tensile properties of the pressure tubes from longitudinal sections were determined by using servo hydraulic Instron tensile testing machine.

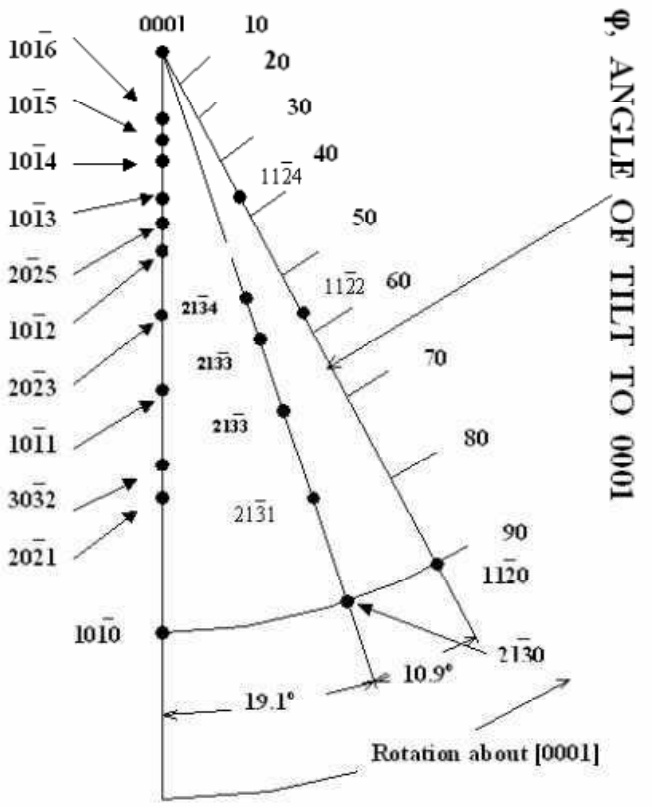

Figure 3.8: Standard Projection of Diffracting Planes of Alpha Zirconium, c/a = 1.59 showing 17 main peaks used for kearns parameter determinations

Chapter 4

Development of New Fabrication Process Route for Zr2.5% Nb Pressure Tube

Zr–2.5 wt.% Nb alloy pressure tubes for the Indian pressurized heavy water reactors (PHWRs) are currently fabricated by hot extrusion and two-stage pilgering [30, 79, 93, 94] with an intermediate annealing treatment. The pressure tubes undergo irradiation enhanced changes in shape and dimensions due to the irradiation creep and irradiation growth, which limits their in-service performance and life [14, 55, 56]. The dimensional instabilities viz., tube axial elongation, diametral creep, and creep sag in pressure tubes are strongly dependent on the tube microstructure, texture and mechanical properties. These microstructural and textural features are essentially governed by the manufacturing process of the pressure tube. Fabrication trials involving variation in three important stages of pressure tube manufacturing were undertaken with an objective of improving the resistance to irradiation induced creep and growth through microstructural and textural modifications [9, 14, 55]. The variations were with respect to the mode (forging versus extrusion) and steps of primary breakdown of the cast structure of the ingot, the hot extrusion ratio to produce tubular blank, and the number of subsequent cold work stages to achieve the specified dimension of the finished tube. The salient feature of this campaign is that, the reported fabrication trials are actually performed on full industrial scale (as used for manufacturing 6.4 meter long pressure tube). In-depth microstructural characterization through different techniques was carried out at each step of these trials to ascertain the morphology of the alpha phase, distribution and composition of the beta phase, and crystallographic texture. Mechanical property evaluation has also been done to establish the structure–property relationship [8]. This chapter presents a summary of the detailed characterization of each step of the various fabrication routes that were employed and reveals the role of each stage on the final microstructure and properties.

4.1. Fabrication methodologies

On the basis of the identified variables in each of the stages, a total of six processing routes (including the current route) have been selected for the present study keeping in mind the manufacturing resources available (Figure 4.1). The major variations in the manufacturing routes adopted were basically: (i) method (extrusion or forging) and number

of stages (single or double) for breaking the cast structure, (ii) tube blank production with two different extrusion ratios, and (iii) single or double pass pilgering with intermediate annealing. In all the above fabrication routes the extruded blank was stress relieved at 480 ^{o}C for 3 h.

<table>
<tr><th>Route A</th><th>Route B</th><th>Route C</th><th>Route D</th><th>Route E</th><th>Route F</th></tr>
<tr><td>Ingot (350mm)</td><td>Ingot (350mm)</td><td>Ingot (350mm)</td><td>Ingot (550mm)</td><td>Ingot (550mm)</td><td>Ingot (350mm)</td></tr>
<tr><td rowspan="2">Press forging (230mm)</td><td rowspan="2">Press forging (230mm)</td><td rowspan="2">Extrusion (230mm)</td><td>Press forging (350mm)</td><td>Radial forging (350mm)</td><td rowspan="2">Extrusion (230mm)</td></tr>
<tr><td>Press forging (230mm)</td><td>Radial forging (230mm)</td></tr>
<tr><td>β quenching</td><td>β quenching</td><td>β quenching</td><td>β quenching</td><td>β quenching</td><td>β quenching</td></tr>
<tr><td>Extrusion (7.3:1)</td><td>Extrusion (12.75:1)</td><td>Extrusion (12.75:1)</td><td>Extrusion (12.75:1)</td><td>Extrusion (12.75:1)</td><td>Extrusion (7.3:1)</td></tr>
<tr><td>Stress relieving</td><td>Stress relieving</td><td>Stress relieving</td><td>Stress relieving</td><td>Stress relieving</td><td>Stress relieving</td></tr>
<tr><td>Ist pilgering (55%)</td><td rowspan="3">Pilgering (20%)</td><td rowspan="3">Pilgering (20%)</td><td rowspan="3">Pilgering (20%)</td><td rowspan="3">Pilgering (20%)</td><td>Ist pilgering (55%)</td></tr>
<tr><td>Annealing</td><td>Annealing</td></tr>
<tr><td>IInd pilgering (20%)</td><td>IInd pilgering (20%)</td></tr>
<tr><td>Autoclaving</td><td>Autoclaving</td><td>Autoclaving</td><td>Autoclaving</td><td>Autoclaving</td><td>Autoclaving</td></tr>
</table>

Figure 4.1: Different fabrication trials

The composition of the starting ingots is given in table 4.1. For the single stage extrusion routes (routes C and F), the primary breakdown of the ingot was obtained at a temperature of 815^{o}C by employing an extrusion ratio of 2.3:1 and strain rate of 1.2–1.5 per sec using a 3780T horizontal extrusion press. For the single press forging routes (routes A and B), the same amount of reduction was obtained by open die forging of the ingot using a 1500T forging press. Forging for the single forging route was carried out at a temperature of 950^{o}C and a forging speed of about 100 mm/s. Conversion of the ingot from 350 mm Ø to the final 230 mm Ø was completed in a number of forging passes with reduction per pass varying from 30 mm/pass in the initial stages to 20 mm/pass in the final stages of forging. The strain rate throughout the press forging was estimated to be in the range of 0.30–0.40 per sec.

Table 4.1: Chemical compositions of Zr-2.5Nb alloy Pressure tube

Routes	Elements			
	Nb (wt%)	O (ppm)	Fe (ppm)	C (ppm)
Route(A,B,C&F) 350Ø mm Starting Ingot	2.5	1126	645	60
Route(D&E) 550Ø mm Starting Ingot	2.72	1238	1130	71

During the ingot processing campaign another variation in terms of the primary breakdown of the ingot was employed by carrying out forging in two stages starting with Ø550 mm arc melted ingot. Two different methods of forging were tried out, viz., press forging and radial forging [90, 95] (routes D and E respectively). In the latter case, deformation was imparted through closed die forging. The current radial forging trials were carried out on a GFM SX-65 type machine with a capacity of 1540T. The deformation in radial forging results from a large number of short strokes at high speed by 4 hammer dies arranged radially around the work piece. In addition, during forging the work piece is rotated to obtain a forged surface with an acceptable surface finish. In both the stages of forging the total deformation was achieved in multiple forging passes maintaining a mean effective strain rate of 0.2–0.85 per sec in the deformation zone of the dies.

4.2. Results and discussion

In essence the focus of the present study is to address the following issues pertaining to pressure tube fabrication:

- Forging versus extrusion during breaking of the cast structure and to reveal the effect of breaking the cast structure in single versus double step forging.
- Effect of high versus low extrusion ratio on the microstructure and texture.
- The effect of single pass pilgering against double pass pilgering with intermediate annealing.

Since the changes brought by a particular step are best understood by examining the microstructure immediately after it, the present investigation compares the different routes by studying the respective microstructures that results after each of the three major processing variables considered in the present study, viz., extrusion versus forging (single and double) for breaking the cast structure, high versus low extrusion ratio in the blank extrusion, single

vs double pilgering subsequent to extrusion. Since these variables cannot be studied in isolation, a holistic comparative analysis is presented by taking into account all the routes together at each stage as follows.

4.2.1. Microstructural characterization

The microstructures developed in the different processing routes (A–F) have been characterized through SEM and TEM at three distinct stages viz., (i) after breaking of the as-cast structure, (ii) after extrusion of β quenched-hollow billet, and (iii) after final cold work. These are described in detail in the following sections.

Microstructure subsequent to cast structure breaking

The SEM and TEM [65, 96] micrographs given in Figure 4. 2a–d and Figure 4. 3a–d respectively show the microstructures obtained after the final breakage of the as-cast structure in all the routes, i.e., in an ingot of 230 mm Ø. In case of all the forging routes viz., single press forging, double press forging and double radial forging, the microstructure was found to be coarser in comparison to that of extrusion. It may be noted that the term ‘‘coarseness’’ is being used in this work with respect to the width of the α lamellae (i.e., dimension along transverse direction of the tube).

Figure 4. 2 and 4.3, when seen in combination, clearly reveal that forging in general lead to coarse α grains, while double forging further enhanced the coarseness of the α phase (see Figure 4. 3 in particular). For example, the average width of the α lamellae was around 2–3 μm in case of double radial forged route (route E), whereas, in case of extrusion and single press forging routes the value of the same are in the range of 1.5–2 μm (for routes A, B, C and F). Similarly, TEM investigation revealed that the width of the β phase is higher in the double radial forged route (route E) as compared to extrusion and single press forge routes (routes A, B, C and F), compare Figure 4.3c with figure 4.3a and d. All of these observations could be attributed to the higher temperatures employed in the forging routes. For single press forging, the working was carried out at 950^{o}C, i.e., just in the β region. In double forging routes, the first stage reduction from 550 mm Ø ingot (forging ratio – 2.5:1) was carried out at 1015 ^{o}C and the second stage reduction from 350 mm Ø to 230 mm Ø was accomplished at a lower temperature of 815^{o}C in the two phase region consisting of both α and β phases. Since the starting diameter of the ingot was 550 mm (considerably larger than the 350 mm ingot

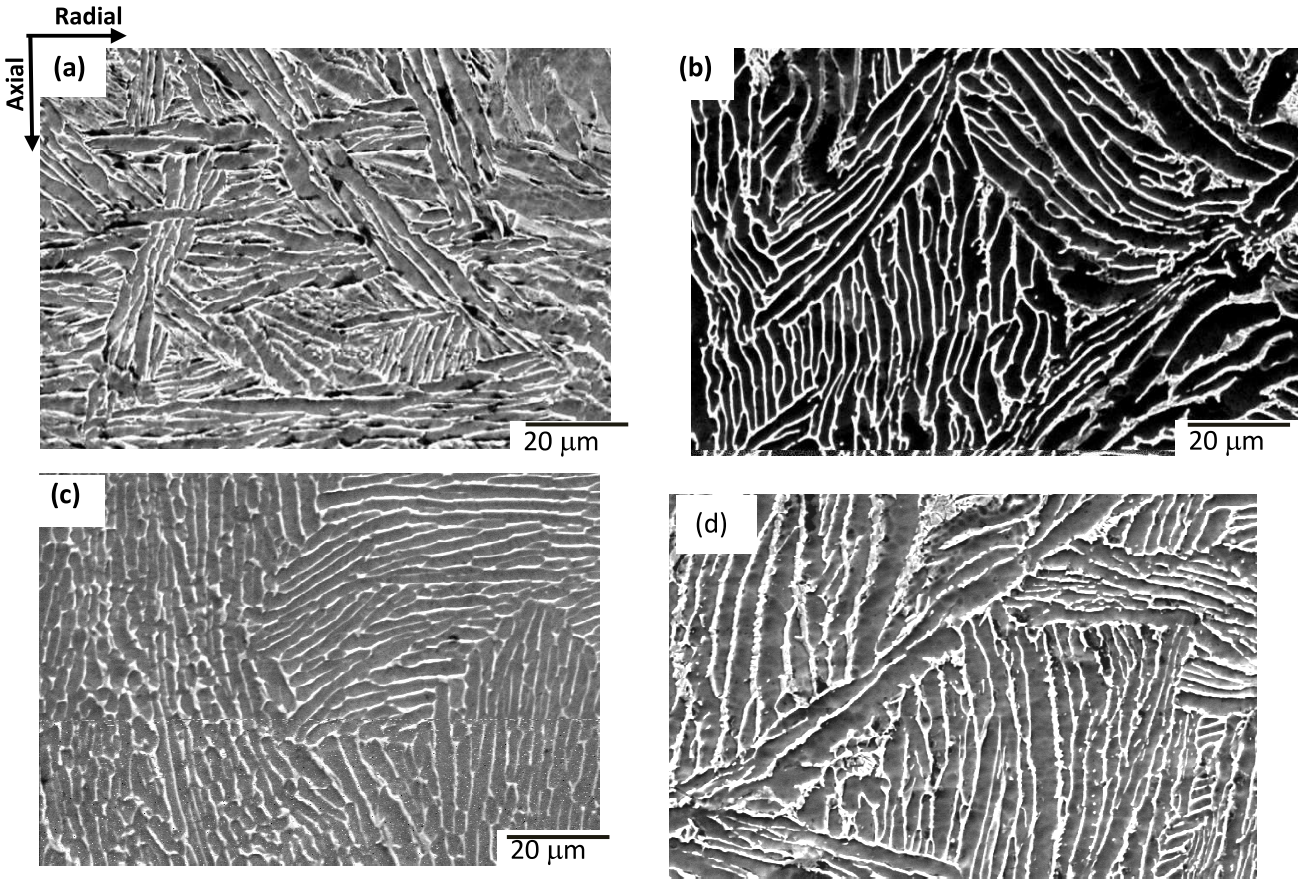

Figure 4.2: SEM micrographs after final breaking of cast structure (at 230 mm dia stage); (a) Single press forge routes (routes A and B), (b) Double press forge route (route D), (c) Double radial forge route (route E), (d) Single extrusion routes (routes C and F)

size in the single stage process routes), a higher temperature of 1050^{o}C, as employed elsewhere, was used for the first forging stage. This ensured processing of the ingot entirely in the β phase region of the Zr–2.5Nb alloy thereby lowering the deformation load along with the added advantage of homogeneous distribution of all the alloying elements. However, the coarseness introduced in the microstructure during the first forging stage seems to be retained even after further processing in the α + β region during the second forging step and this could be the reason for exhibiting coarser microstructure as compared to the single forged routes (A and B). However, for all forging routes the microstructure was more uniform in terms of the aspect ratio of the α phase and distribution of the β phase in between α/α filaments throughout the length of the tube. SEM and TEM micrographs of the forged ingots clearly show the higher width of β phase sandwiched between relatively longer α/α interfaces, which has been found to be desirable from a diametral creep point of view. Moreover, the final microstructure developed after radial forging, as observed in Figure 4. 2c and 4.3 c, clearly indicated the homogeneity of deformation, i.e., uniformity with respect to the extent of the

mechanical work both along the length and across the cross-section, as well as equal interspacing of the β phase in the α phase matrix as compared to microstructures developed by other trial routes. It may be noted that this particular observation regarding homogeneity of the microstructure is based more on the SEM micrographs (Figure 4. 2) which represent a much larger area compared to the TEM micrographs (Figure 4.3). Radial forging leading to an improvement in microstructural uniformity has also been reported elsewhere [97-99]. For breaking of the cast structure by extrusion, noticeable differences could be observed in the morphology (thickness, aspect ratio) of the α phase (Figure 4. 3 d) compared to that of forged microstructures. This suggests relatively higher deformation heterogeneity in the extrusion process in comparison to the forging mode of deformation.

Microstructure after hot extrusion of hollow billet

Once the cast structure was completely broken, the Zr–2.5Nb solid billets underwent deep hole drilling followed by expansion to obtain the desired size of hollows. The expansion is essentially a back extrusion process carried out at elevated temperature to expand a smaller hole in the billet made by deep hole drilling. Pre-heated billets are placed into a vertical container and the inner diameter is expanded by passing a nose cone tool under the hydraulic pressure. The diameter of the nose cone determines the final inner diameter of the hollows. Volume constancy is maintained by an increase in length of the actual preheated billet. Further, the hollows were β-quenched from 1000^{o}C to achieve randomization of texture and homogenization in terms of chemical composition. The β quenched samples showed fully martensitic microstructure consisting of both internally twinned (Figure 4. 4 a) as well as internally slipped martensites (Figure 4. 4 b) throughout the cross-section of the hollow billet as observed in other studies of Zr–2.5Nb alloy.

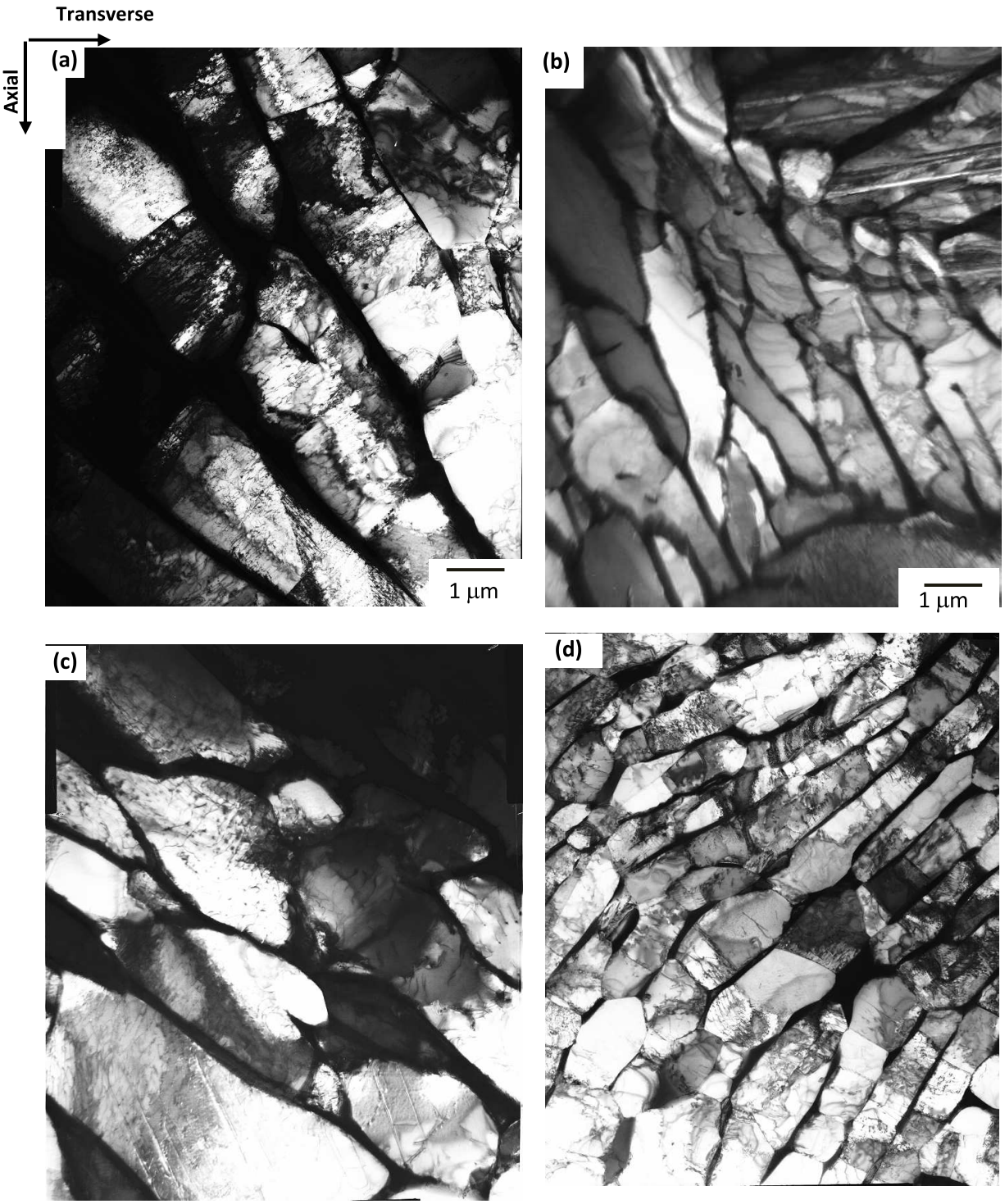

Figure 4.3:: TEM micrographs after final breaking of cast structure (at 230 mm dia stage) in transverse direction (centre); (a) Single forge routes (Route A and B), (b) Double press forge route (Route D), (c) Double radial forge route (Route E), (d) Single extrusion

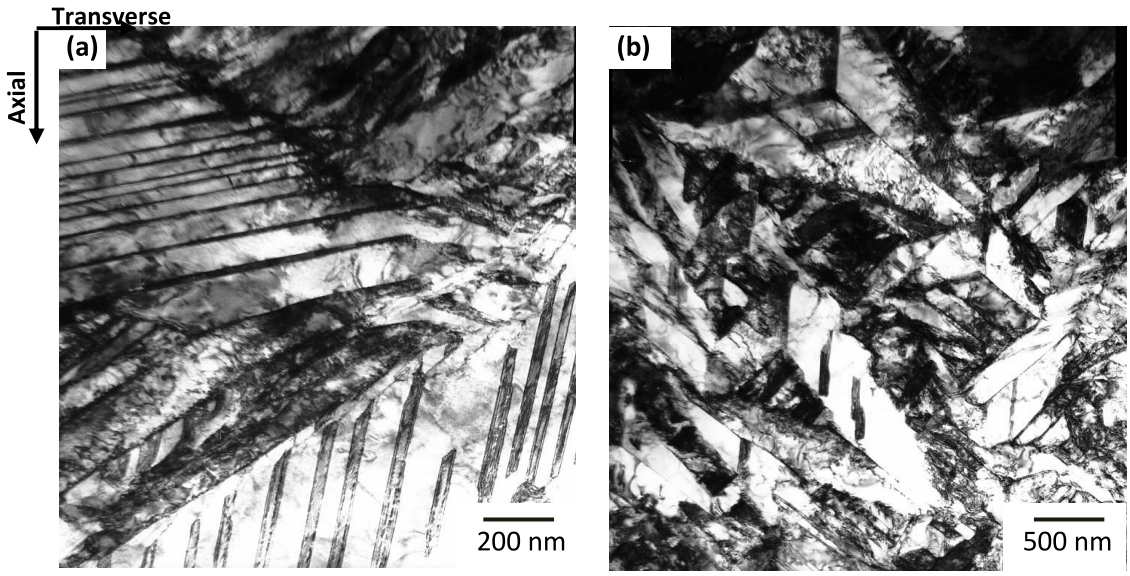

Figure 4.4: Bright field TEM micrographs of beta quenched hollow billets of Zr-2.5Nb alloy showing fully martensitic microstructures; (a) internally twinned martensites and (b) internally slipped martensites.

For routes A and F, extrusion was carried out in the two phase field ($\alpha + \beta$) at 800 ^{o}C and at the lower extrusion ratio (ER) of 7.3:1, whereas for routes B, C, D and E tube, extrusion was carried out at 815^{o}C and at a higher extrusion ratio of 12.75:1. The higher ER is expected to modify microstructure and texture strongly.

The SEM micrographs given in figure 4.5 represent the microstructures of the extruded blanks following the different fabrication trials. It may be observed that deformation imparted during the extrusion of hollow billets resulted in blanks with microstructures having dispersion of long and thin α and β phases in lamellar morphology. Air cooling of the blank after extrusion transforms the β phase to α phase by growth on the existing α grains and the remaining β phase becomes enriched in Nb. In general, extrusion of billet with the lower ER of 7.3:1 resulted in a variation of the microstructure in the blank from the leading to the trailing end (routes A and F) (Figure 4. 5a and b). The microstructure at the trailing end was found to be much finer, lamellar and homogeneous. This indicates that extrusion plays a major role in generating the tube microstructure. The primary cause of such grain size variation and/or texture variation (discussed in next section) along the length of the tube is the temperature change during the extrusion process [21, 22]. This can be rationalized by noting that billets are much hotter than the extrusion chamber and cool during the extrusion process.

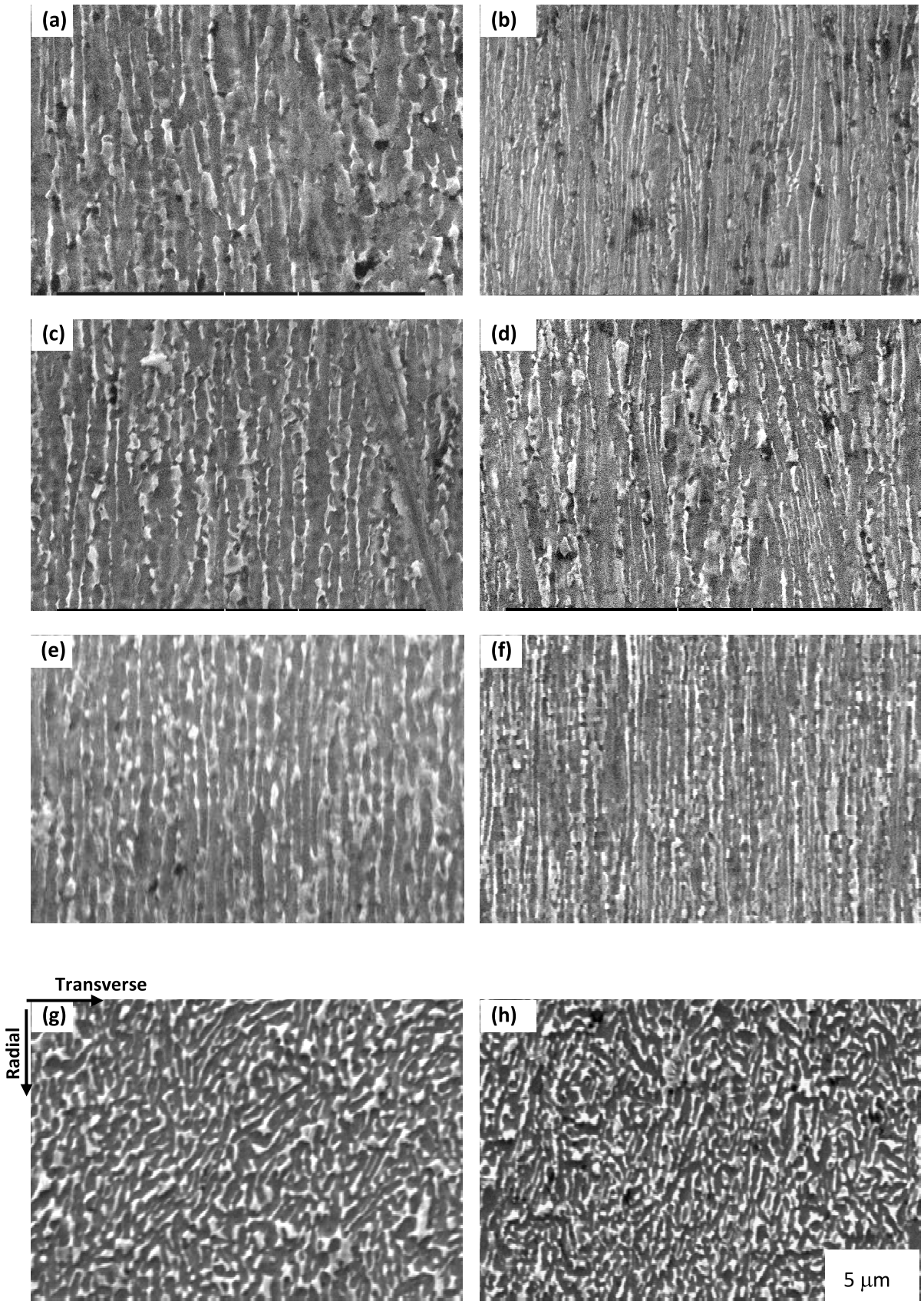

Figure 4.5: Secondary electron SEM micrographs of extruded blanks; (a) and (b) leading and trailing ends respectively of the longitudinal section of tube blank extruded with low ER (7.3:1) (cast structure broken by single extrusion, routes A and F), (c) and (d) leading and trailing ends respectively of the longitudinal section of tube blank extruded with high ER (12.75:1) (cast structure broken by double press forging, route D), (e) and (f)

leading and trailing ends respectively of the longitudinal section of tube blank extruded with high ER (12.75:1) (cast structure broken by double radial forging, route E), (g) and (h) transverse section of (e) and (f) respectively. The blanks extruded with low ER are showing larger variation along the tube length in comparison to the blanks extruded with higher ER value.

Hence the material that is coming out first (leading end) will have a lesser temperature drop on account of a shorter residence time in the extrusion chamber. On the other hand the trailing end experiences comparatively higher heat loss due to longer contact with the relatively cold extrusion chamber. This results in higher grain size in the leading end as compared to the trailing end [21]. This variation in as-fabricated microstructure could be responsible for the usually observed variation in the in-pile deformation behavior of pressure tubes [30, 71, 79]. For blanks extruded with the higher ER of 12.75:1 the variation in microstructure between the two ends was found to be lower (routes B–E) (Figure 4. 5 c–h); the leading and the trailing end samples from as extruded blank show nearly the same grain morphology and grain sizes. Since a higher ER implies a relatively larger amount of plastic work, the fraction of deformation heat generation also increases which can, to some extent, compensate the heat loss at trailing end. This can lower the temperature difference between the leading and the trailing ends and is evident from the results shown. Further, it may be observed that the higher ER resulted in α grains with larger aspect ratio, see Table 4. 2. The variation from leading to trailing end of the blank appears to have been further reduced in the case of double radial forging (Figure 4. 5e–h).

The β phase between two α lamellae, although apparently continuous in the SEM images from all routes, is actually discrete in nature when imaged with TEM (Figure 4. 6). The TEM micrographs of the extruded blanks indicated dynamic recrystallization of the α phase during hot extrusion in all of the routes (Figure 4. 6 a). Presence of equiaxed grains with high angle boundaries within the α lamallea showing very low dislocations densities in conjunction with few grains bearing significant signatures deformation is a clear indication of the process of dynamic recrystallization occurring during the hot extrusion step. All these features can be easily seen in Figure 4. 6a. The chemical composition of the α and β phases , as determined by TEM–EDS analysis, is ~ 1 wt.% Nb and 17 wt.% Nb respectively. In addition, TEM further corroborated the SEM finding with regard to the significance of ER in controlling the uniformity of the microstructure from the leading to the trailing end of the tube and also the aspect ratio of the α phase, see Figure 4. 7. Moreover, TEM micrographs indicated that higher ER lead to better continuity of the β phase in the extrusion direction.

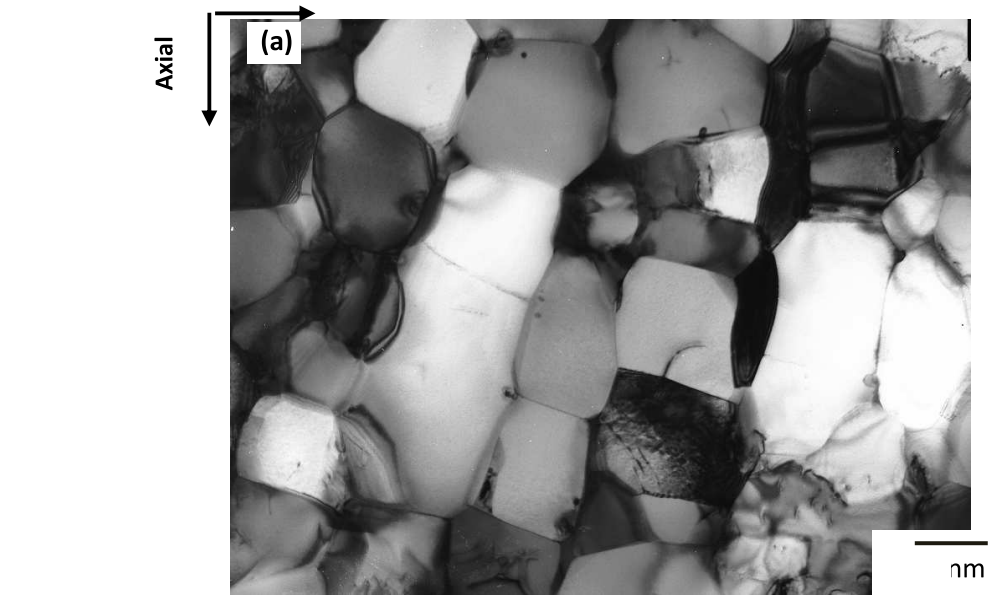

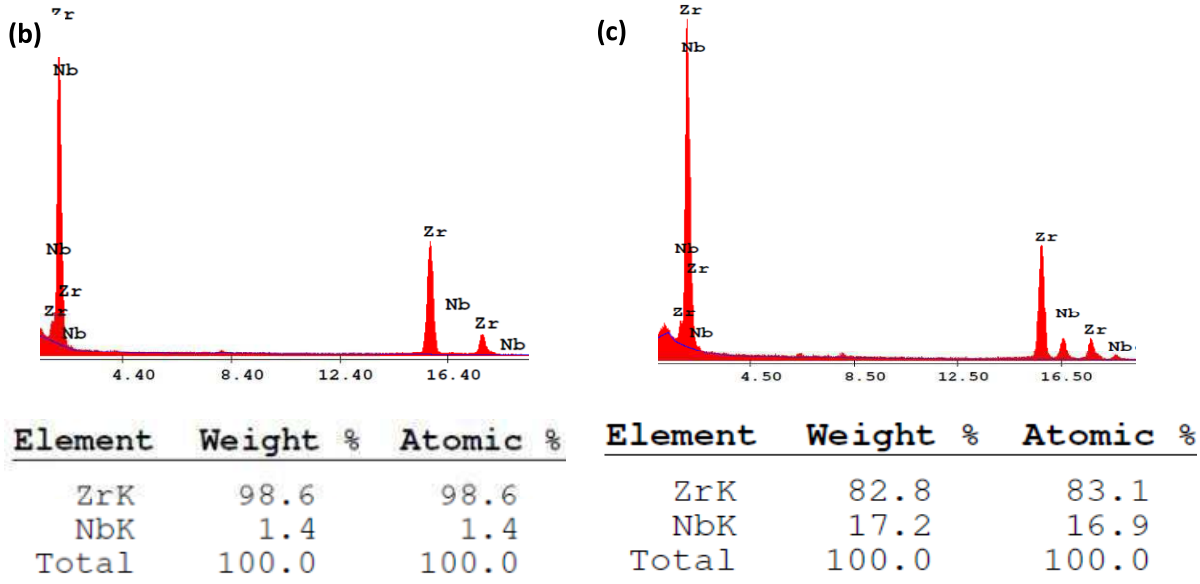

Element	Weight %	Atomic %
ZrK	98.6	98.6
NbK	1.4	1.4
Total	100.0	100.0

Element	Weight %	Atomic %
ZrK	82.8	83.1
NbK	17.2	16.9
Total	100.0	100.0

Figure 4.6: TEM analysis of the extruded pressure tube blank of Zr-2.5Nb alloy; (a) Bright field micrograph showing fully dynamically recrystallized α and β microstructure, (b)-(c) TEM-EDS analysis showing composition of α and β phases respectively.

This could be attributed to higher degree of deformation imparted during extrusion with higher ER.

The comparison of microstructures from all routes at the extruded blank stage clearly show that, the routes involving forging as the primary method of cast structure breaking yield relatively larger grain structures in comparison to those which employ extrusion. This

highlights the importance of the previous processing step in determining the microstructures at the blank stage.

Microstructure at final cold work stage

The extruded blanks in all the trials were subjected to a stress relieving operation at 480 ^{o}C for 3 h, which did not bring any significant changes except removing the thermal stresses introduced in the blanks during the quenching operation carried out after extrusion. Extruded and stress relieved blanks were cold pilgered in single or double pass to achieve final dimensions (i.e., outer diameter and wall thickness) of the pressure tube. Routes A and F include two stages of cross-sectional area reductions of 55% and 20% (with an annealing in between) starting from a tubular blank extruded with the low ER. Whereas for routes B, C, D and E final dimension of pressure tube was achieved by a single pass 20% cross sectional area reduction starting from a tubular blank extruded with the high ER.

The pilgering process, be it single pass or double pass, increased the dislocation density in the extruded microstructure and a complex network of dislocations could be seen within the α phase, typical of a heavily cold worked structure. However, the lamellar nature of the α and the β phase is largely unchanged by the pilgering process (see Figure 4. 8). The intermediate annealing carried out at 550 ^{o}C for 6 h between the first and second pass pilgering operations (routes A and F) resulted in recovery and/or partial recrystallization. Moreover, the β phase had undergone substantial modification during the annealing treatment and was present as globular precipitate in certain locations both within the α grain and at the α/α interfaces. TEM–EDS analysis showed niobium content in the β phase at the α/α interface of 14 and 44 wt.% respectively as stringers and as a globular precipitates (Figure 4. 8). This shows heterogeneity of the β phase both in terms of morphology as well as composition after intermediate annealing.

The SEM (Figure 4. 9 and 4.10) and TEM micrographs (Figure 4. 11) depict the typical microstructures obtained after the final pilgering operation in routes employing single and double pass pilgering. Aspect ratios of the α phase in final autoclaved pressure tube manufactured by different trial routes has been tabulated and presented in Table 4. 2. It can seen from Table 4. 2 that a substantial reduction in α grain thickness has occurred from that of the as-extruded blanks after the pilgering operation.

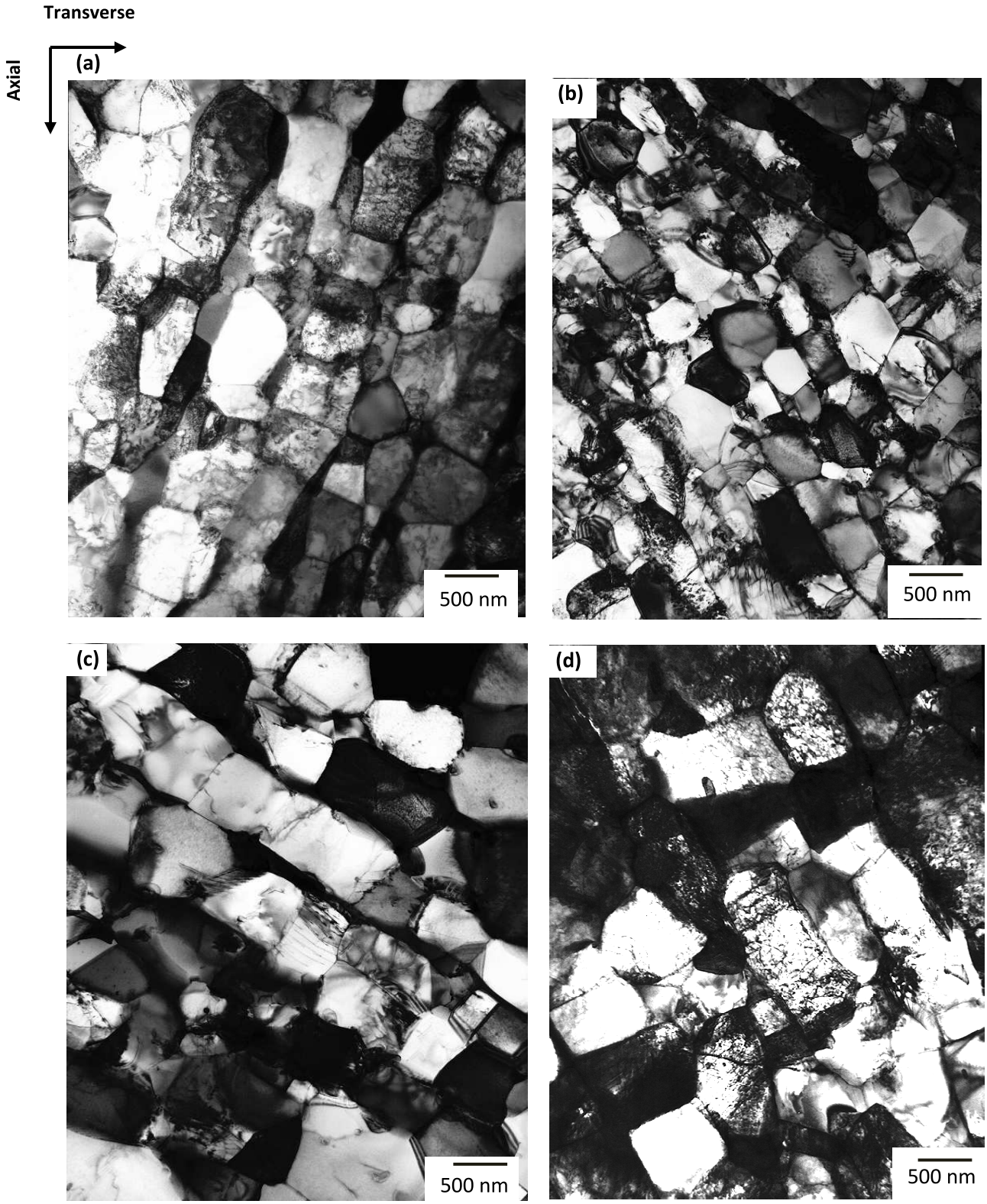

Figure 4.7: Bright field TEM micrographs of pressure tube blanks extruded with different extrusion ratios; (a) leading end and (b) trailing end of tube extruded with ER 7.3:1(route F), (c) leading end and (d) trailing end of tube extruded with ER 12.75:1(route E).

In general, all the single pass pilgered blanks, as compared to double pass pilgered blanks, exhibited a predominant increase in the length of the α filaments (Length of α filament in this paper refers to the dimension of α filament along the axial direction of the tube) together with a continuous β film along the α/α interfaces. Moreover, single pass pilgering resulted in more homogenous and predominantly lamellar microstructure from leading end to trailing end as compared to two-pass pilgering with intermediate annealing. In addition, the beta phase could be seen to be present in a more continuous manner at the α/α interfaces as opposed to a globular distribution noticed for the routes with two stages of cold work. Extrusion at a high ratio followed by single pass pilgering in routes D and E, where double stage press and radial forging were employed respectively for breaking of the as-cast structure, led to a significant increase in both the width and the length of the α grains thereby resulting in a very high aspect ratio. In fact, tubes produced using route E not only exhibited the highest aspect ratio of the alpha phase (~1:10:70) but also showed minimum microstructural variation along the length of the tube.

For route F, i.e., the route which is presently being followed at NFC for manufacturing of cold worked Zr–2.5Nb pressure tubes, α grains were not lamellar in all the regions. Moreover, the length and width of the α filaments were also found to be smaller amongst all the fabrication trials. The β phase was not found to be continuous in many regions; instead it had globulized both at the α/α interface as well as within the α grains. The Nb content in the β phase varied from 15 to 45 wt.%. It was noticed that the coarseness introduced during the forging step was carried forward through subsequent processing steps resulting in relatively coarser grain structure in the final cold worked state of the pressure tube. This is expected to be beneficial in terms of reducing diametrical creep strain [9, 100], particularly at the back end (or trailing end) of the pressure tube. This has been rationalized in terms of the non-linear effect of grain size, i.e., greater dependence of the diametrical creep at small grain thickness [17].

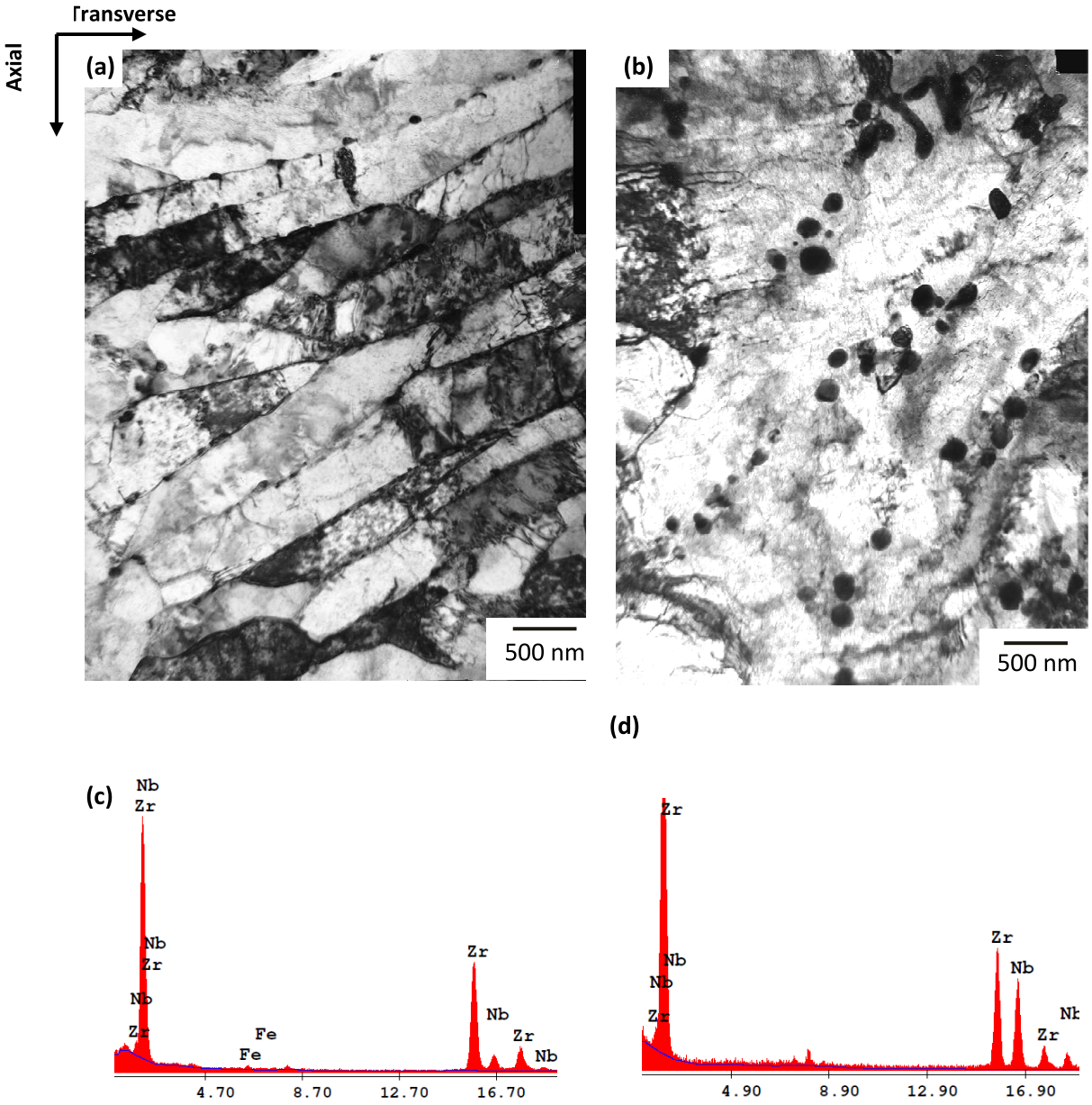

Elements	Wt%	At%
Zr	86.0	86.6
Nb	14.0	13.4

Elements	Wt%	At%
Zr	55.9	56.3
Nb	44.1	43.7

Figure 4.8: Bright field TEM micrographs of Zr-2.5%Nb alloy pressure tube after intermediate annealing showing β phase (a) as stringer between α/α interface and (b) as globulized particles and their composition from EDS analysis in (c) and (d) respectively.

Table 4.2: Morphological features of α grains

Route	Location	Aspect Ratio	α Length (μ)	α Thickness (μ)
As extruded pressure tube condition				
A (low ER)	Leading	1:4:30	6-15	0.2-1.0
	Trailing	1:4:40	10-20	0.2-0.6
B (High ER)	Leading	1:5:40	15-22	0.2-0.5
	Trailing	1:6:55	15-23	0.2-0.4
Final pressure tube condition (autoclaved)				
Double pass pilgered				
A	Leading	1:4:35	5-12	0.2-0.4
	Trailing	1:5:40	8-13	0.1-0.3
F	Leading	1:4:30	8-10	0.1-0.3
	Trailing	1;5:45	6-11	0.1-0.3
Single pass pilgered				
B	Leading	1:6:55	12-18	0.2-0.4
	Trailing	1:5:45	14-22	0.1-0.4
C	Leading	1:6:60	10-14	0.2-0.5
	Trailing	1:5:50	12-19	0.1-0.4
D	Leading	1:5:50	14-21	0.2-0.5
	Trailing	1:5:60	12-20	0.2-0.6
E	Leading	1:10:65	25-30	0.4-0.5
	Trailing	1:10:70	25-32	0.35-0.45

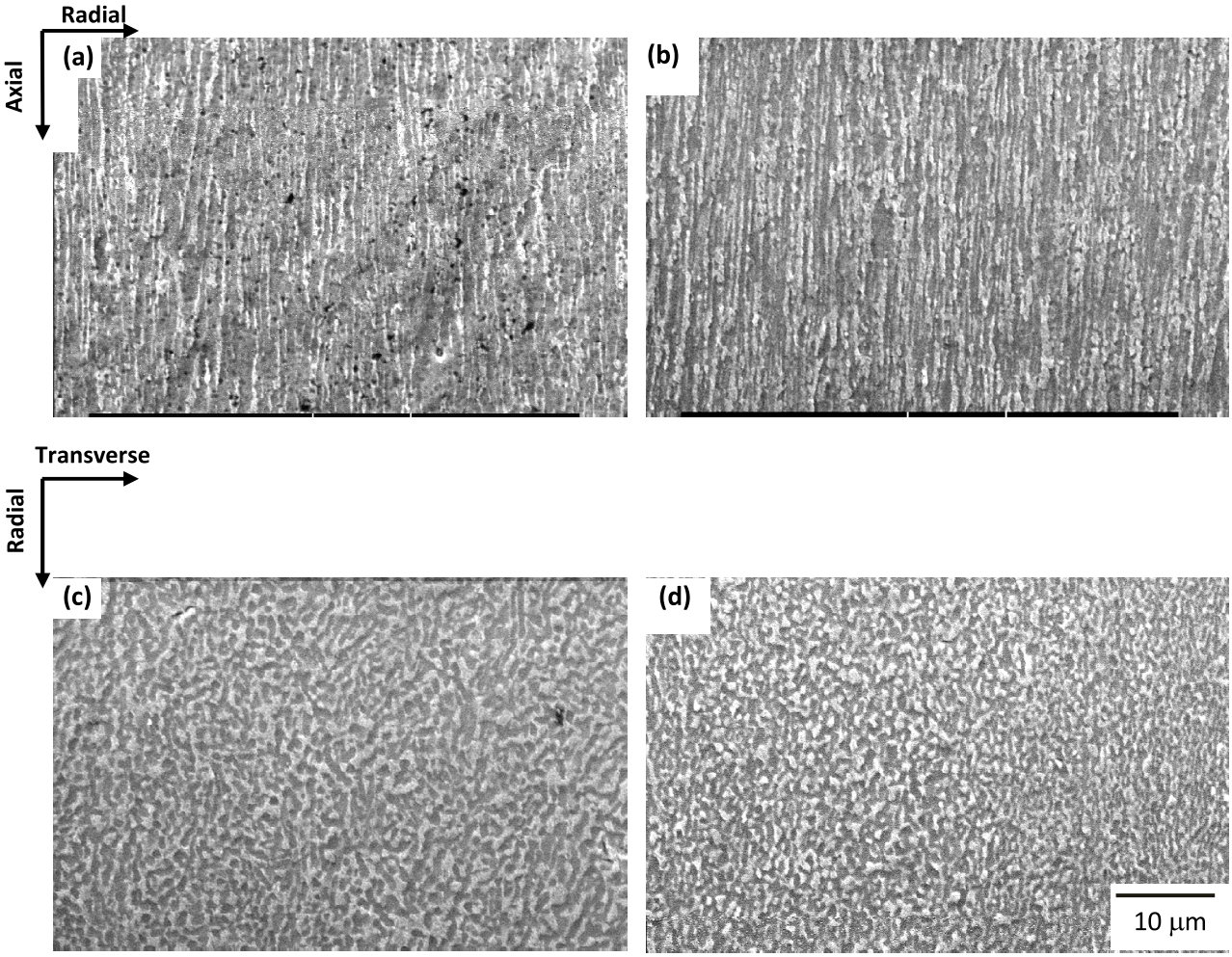

Figure 4.9: Secondary electron SEM micrographs of pressure tube after double radial forging, extrusion of blank with extrusion ratio (12.75:1) and 20% cold reduction by pilgering (route E); (a) and (b) leading and trailing ends respectively of longitudinal section (c) and (d) are transverse sections of (a) and (b) respectively.

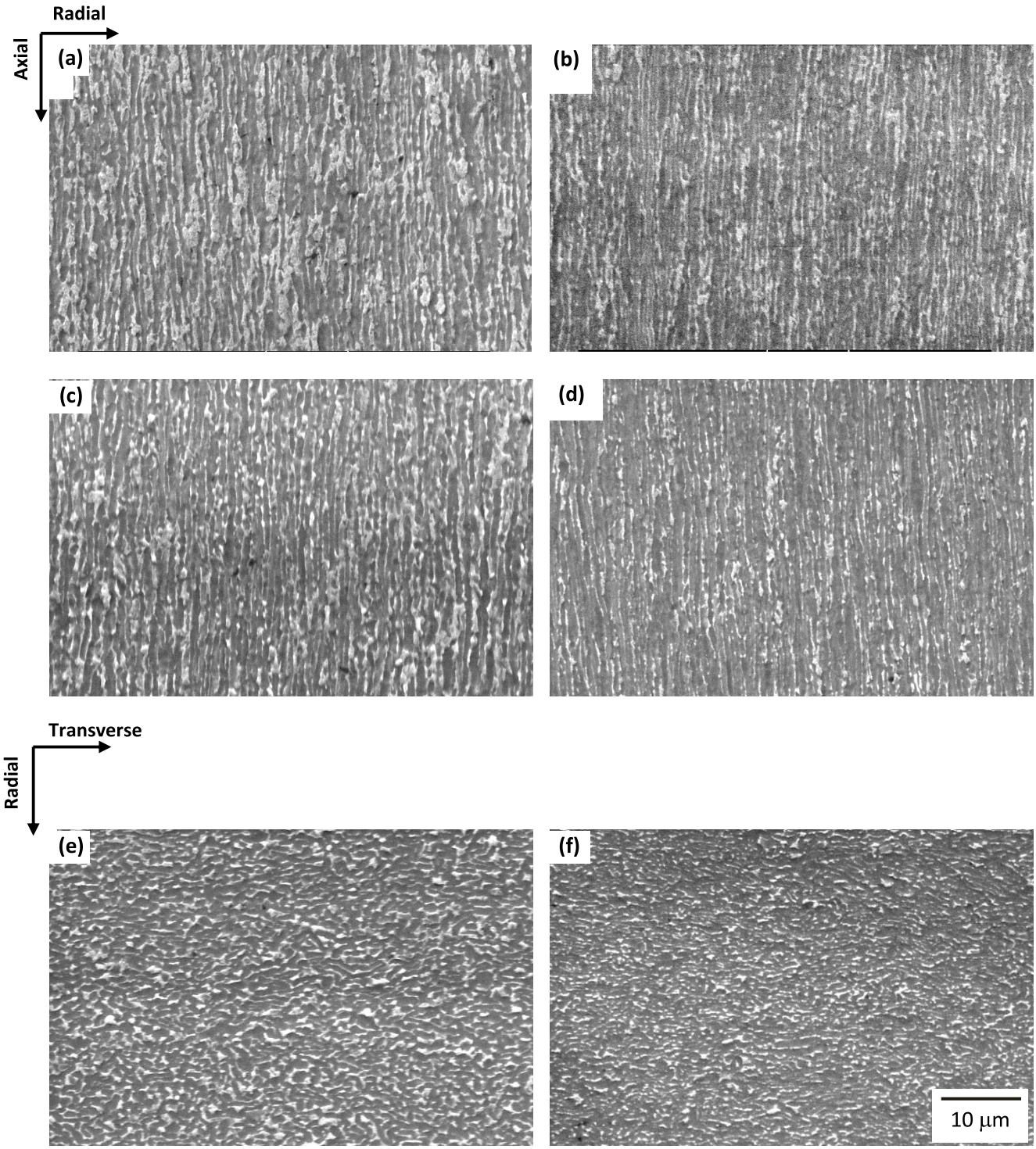

Figure 4.10: (a) and (b) Secondary electron SEM micrographs of leading and trailing ends of pressure tube after breaking of cast structure by single extrusion, tube blank extrusion with low ER (7.3:1), double pass pilgering with intermediate annealing followed by autoclaving (route F), (c) and (d) Secondary electron SEM micrographs of leading and trailing ends of longitudinal section of pressure tube after breaking of cast structure by double radial forging, tube blank extrusion with high ER (12.75:1), single pass pilgering followed by autoclaving (route E), (e) and (f) transverse section of (c) and (d) respectively.

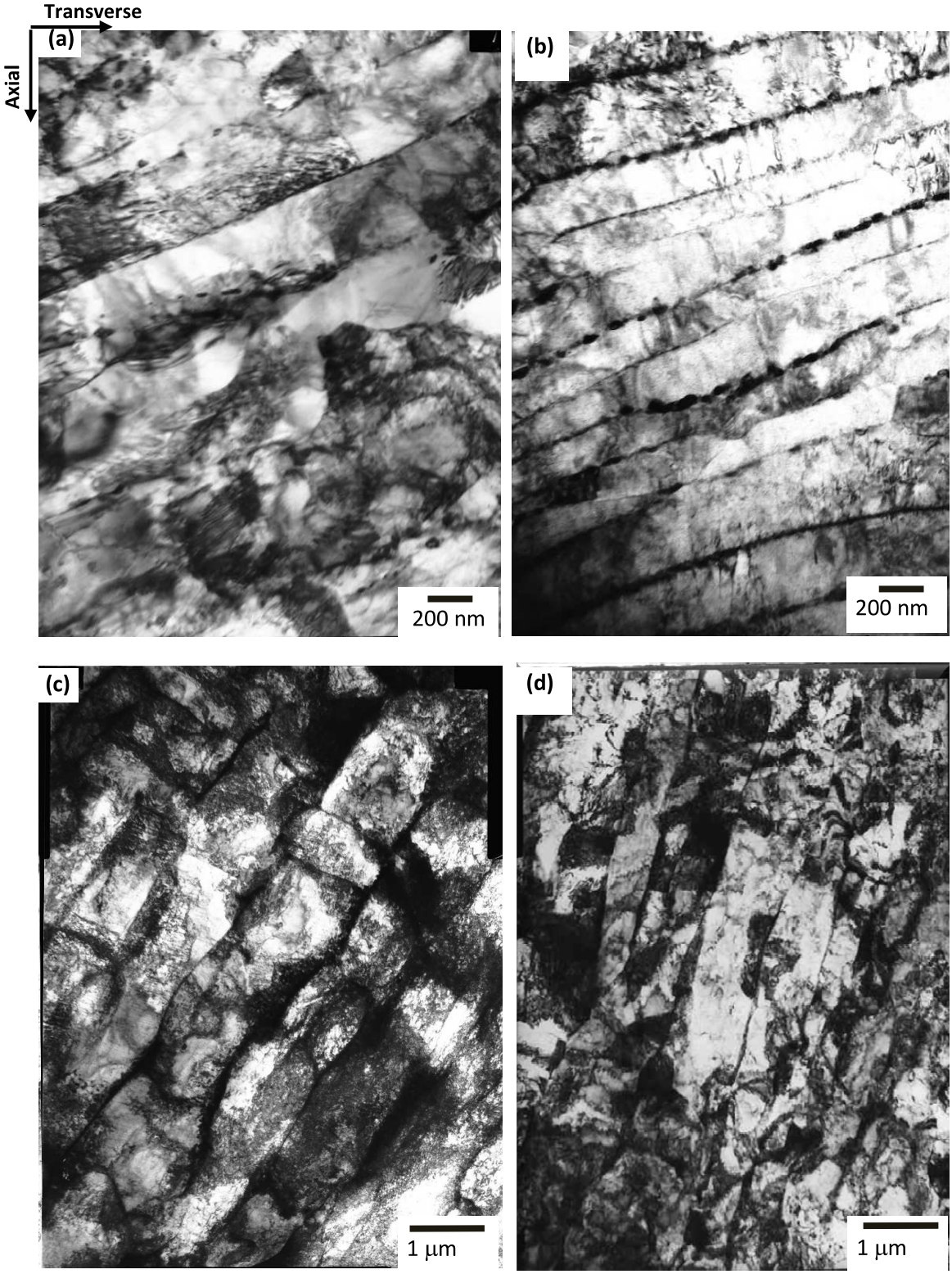

Figure 4.11: Bright field TEM micrographs; (a) leading and (b) trailing end of pressure tube manufactured through double pass pilgering with intermediate annealing(route F), (c) leading and (d) trailing end of pressure tube manufactured through single pass pilgering (route E).

Textural evolution

The texture components of the pressure tubes manufactured with different routes are presented in Table 4. 3. The salient observations are summarized below:

Table 4.3: Basal pole texture variations between the leading and trailing ends of Zr-2.5%Nb pressure tube manufactured from various routes.

Fabrication Route	Location	f_r	f_t	f_a	$f_t - f_r$
Double pass pilgered					
F	Leading	0.33	0.62	0.05	0.29
	Trailing	0.36	0.59	0.05	0.23
A	Leading	0.34	0.62	0.04	0.28
	Trailing	0.35	0.61	0.04	0.26
Single pass pilgered					
B	Leading	0.27	0.68	0.05	0.41
	Trailing	0.26	0.71	0.03	0.45
C	Leading	0.29	0.61	0.10	0.32
	Trailing	0.28	0.66	0.06	0.38
D	Leading	0.26	0.69	0.05	0.43
	Trailing	0.25	0.69	0.06	0.44
E	Leading	0.26	0.68	0.06	0.42
	Trailing	0.28	0.68	0.04	0.40

In general all routes have yielded a similar textural distribution (on a gross scale) with the majority component being f_t and the minority component being f_a. Such texture is expected when the majority of the deformation occurs in the hexagonal alpha phase. Basal plane normals tend to align themselves parallel to principal compressive stresses during the deformation of the α phase, thus making the f_a component very small. The fact that the gross

textural distribution is very similar in all of the cases, agrees with the earlier observations that texture of the pressure tube is governed chiefly by the texture developed during the hot extrusion step (subsequent to the β quenching operation) [52, 79]. It may be noted that all of the routes considered in the present study did involve one common hot extrusion step subsequent to β quenching. The final textures observed are essentially determined during this particular hot extrusion stage only. The routes that involved a higher ER (routes B, C, D and E) and the single cold stage of deformation, however, showed relatively higher f_t values compared to the routes having the lower ER and two stages of cold work (routes A and F). This observation agrees well with earlier work which reported higher f_t values as the extrusion ratio is increased. Some of the chief mechanisms attributed for the high f_t component during the extrusion are (a) rapid growth of appropriately oriented α grains which can make basal pole normals to rotate along the transverse direction during the hot extrusion, and (b) a combination of phase boundary sliding and stress induced phase transformation (β→α). Phase transformation, if it takes place without the constraints of the external stress and neighboring grains, in general leads to weakening of texture (in the present context, increases the f_a component). Since, in the present case, high external stresses are active during the hot extrusion, a considerable degree of variant selection is expected and the results indicate that those variants, which result in the basal pole normal aligning in the transverse direction, are getting favoured during the phase transformation.

Cold work subsequent to hot extrusion did bring about some subtle changes in the texture although the gross nature of texture produced during the hot extrusion was retained. Single pass (pilgering) route was found to give significantly high f_t and $f_t - f_r$ values in comparison to the routes involving double pass pilgering. In other words, changes in texture from the hot extrusion stage were minimal when only one pass of cold pilgering was involved. It may be pointed out that such a texture (with high f_t and lower f_r) is expected to be beneficial from the point of view of diametrical creep during the service life [9, 24].

Double pass pilgering, with one additional intermediate annealing however, resulted in the decreased f_t component in the final texture. This observation is also in line with the known understanding that annealing results in the rotation of basal poles.

The differences in texture values from leading end to trailing end seem to be less pronounced for routes that had forging as their principal step for breaking the cast structure. This may be attributed to better homogeneity of deformation and efficient break up of cast structure achieved in forging than the extrusion process. In addition, routes involving the

higher ER were found to have minimal differences in texture along the length of the tubes. The reason for this increased textural homogeneity at the higher extrusion ratio can be expected due to increased temperature homogeneity at the higher ER.

Mechanical properties

Table 4. 4 shows the mechanical properties of the tubes produced from the various fabrication routes after the autoclaving operation. In essence the variation in the mechanical properties among tubes produced from different routes is not found to be significant. However, it can be noticed that the forging route samples are showing slightly higher ductility. The rest of the properties were nearly the same in all the pressure tubes produced with the different routes. Further, the properties obtained by modified routes do meet the existing specifications for the pressure tube. Based on these observations of satisfactory mechanical properties, and improved microstructural and textural properties, of the double radial forged route with higher extrusion ratio followed with single cold reduction by pilgering (route E) seems to be a promising modification to the existing practice of pressure tube manufacturing at NFC.

Table 4.4: Mechanical properties of pressure tubes produced with different fabrication routes

Routes	Room Temperature			300°C		
	UTS (KSI)	YS (KSI)	% EL	UTS (KSI)	YS (KSI)	% EL
SPECIFICATION (540 MWe PHWR)	-	<85	-	67 (min)	47 (min)	14 min)
Double pilgered						
A	114.4	81.4	18.0	76.4	57.4	18.0
F	111.6	79.8	18.1	78.6	56.9	22.0
Single pilgered						
B	106.8	76.3	20.0	72.7	54.6	21.3
C	106.7	78.7	18.0	72.9	61.4	18.4
D	119.1	86.0	15.5	80.5	62.8	19.1
E	115.0	89.0	16.0	84.3	62.8	20.7

4.3. Conclusions

- The forging process, in particular double radial forging, resulted in more effective and uniform breakage of cast structure in comparison to the extrusion process.
- The higher extrusion ratio (followed by single pass pilgering) results in longer α grains with a higher aspect ratio and a relatively more continuous β phase along the α/α interface. The microstructure and texture is more uniform from leading end to trailing end. In addition, the higher extrusion ratio was observed to result in higher f_t and $f_t - f_r$ values.

- The intermediate annealing in the double pass pilgering route results in globulization and discontinuous beta phase and these are enriched with niobium up to 45 wt.%.
- In general, mechanical properties were very similar among all the routes that were employed in the present study.
- In general, the double radial forging based route led to a better (i) homogeneity in microstructure and texture along the entire length i.e., from the leading to the trailing end of the tube, (ii) higher aspect ratio of the alpha grain which is reported to be beneficial for diametral creep, and (iii) moreover, it led to a substantial increase in the ft and ft–fr values of the basal pole texture.

Chapter 5
Microstructural Studies of Heat Treated Zr-2.5 Nb Alloy for Pressure Tube Applications

5.1. Introduction:

As explained in the previous chapters, irradiation creep and irradiation growth are two important limiting factors for the life of the pressure tube in PHWR reactors. These phenomena are known to depend on the initial microstructure, texture of the pressure tube. Hence, there has been continuous efforts towards improving the resistance to irradiation induced creep and growth through the modification of the microstructure of the pressure tube material to achieve longer life of the pressure tube in next generation reactors [8]. Many researchers have studied the change in microstructure and its effect on the properties by altering the conventional route of pressure tube fabrication.

The fabrication of pressure tubes involves a large number of thermomechanical treatments, and the final microstructure developed as a result of these fabrication steps determines the long-term and short-term properties of these tubes. It is important to understand the influence of each of these fabrication steps on microstructure and crystallographic texture in order to optimize the pressure tube fabrication. This requires an in depth understanding of the mechanisms of microstructural evolution during these processing steps of the materials. In this study, an attempt is being made to develop heat treated (quenched and aged) pressure tube with improved properties in comparison to the conventional fabrication route adopted for the cold worked (pilgered) route, practiced in Nuclear Fuel complex, Hyderabad. The aim is to develop a heat treatment route that produces operating temperature mechanical properties that are better than those of current pressure tubing, which is in the cold-worked plus stress-relieved condition, and that will have enhanced microstructural stability during high temperature irradiation

The objective of the present part of the thesis is to optimize the fabrication processing parameters with special reference to the quenching and aging treatments. In this study the microstructural evolution at different stages of fabrication as a function of fabrication parameters have been characterized. The mechanical properties and texture of relevant samples have been evaluated.

5.2. Experimental:

Zr-2.5 Nb alloy ingots of 350mm diameter were produced in a consumable vacuum arc melting furnace. The quadruple melting was carried out to reduce the impurity elements (mainly interstitials such as hydrogen, chlorine and phosphorus). The chemical composition of the alloy is given in Table 5.1. In order to break the cast structure, these ingots were further extruded to billets of 230 mm diameter size. Hollow machined billets were subsequently water quenched to achieve compositional and microstructural homogeneity. The quenched billets were soaked at 800^{o}C for 1hr followed by extrusion with an extrusion ratio of 7.3:1. The hot extruded blank of Zr-2.5 Nb alloy was further subjected to cold deformation of 41% by pilgering. This pilgered tube formed the starting material in the present study for various heat treatments in $\alpha+\beta$ phase field as detailed in the Figure 5.1. The heat treatment conditions were determined after establishing the $\beta/\beta+\alpha$ continuous cooling transus temperature for this composition. In the present study, a quenching dilatometer has been used for this purpose. The temperature measurement in the dilatometer was calibrated using the curie temperature of pure Nickel. Samples were initially soaked at 400^{o}C for 30 minutes in dilatometer to relieve the residual stresses. On the basis of the quenching dilatometer studies, various heat treatment conditions (Soaking temperature and cooling rate) were selected.

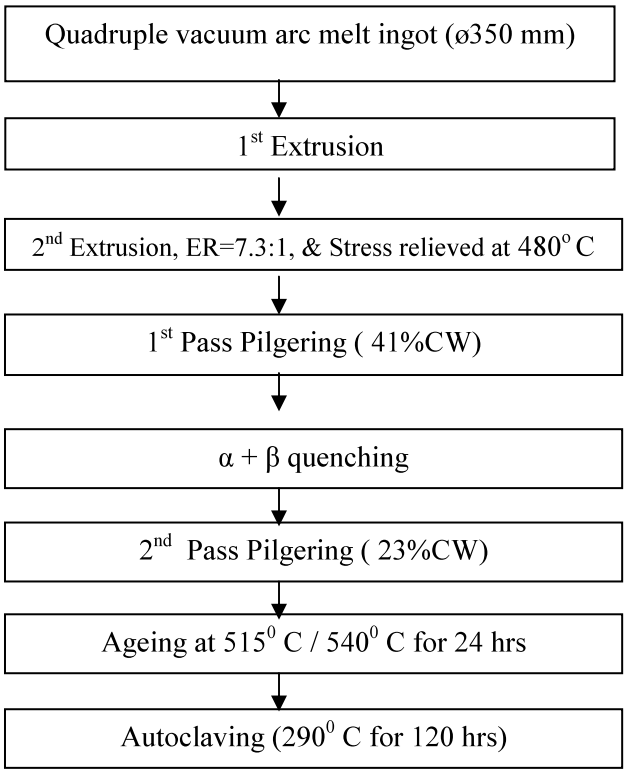

Figure 5.1: Fabrication flow sheet for Heat Treated Pressure Tube

Samples subjected to various quenching treatments were further cold worked to the extent of 23% by pilgering. These samples were finally given ageing treatment at two different temperatures (540 and 515^{o}C) for duration of 24 hrs. These samples were then autoclaved at 290^{o}C for 120Hrs.

Table 5.1: Chemical Composition of material used for the trials

Element	Wt. % / ppm
Niobium	2.68
Oxygen	1137
Nitrogen	28
Iron	650
Tin	25

5.3. Results and Discussion

5.3.1 Determination of $\beta \rightarrow \alpha+\beta_{Zr}$ continuous cooling transus temperature

In order to determine the heat treatment temperature to achieve the desirable phases with appropriate composition and volume fraction, it is important to know the accurate phase transition temperatures. $\beta \rightarrow \alpha+\beta_{Zr}$ continuous cooling transus temperature is known to depend on the concentration of oxygen content in addition to the niobium concentration in the alloy [101]. In the present study $\beta \rightarrow \alpha+\beta_{Zr}$ continuous cooling transus temperature was determined using quenching dilatometer. The samples were cooled from the beta phase field at different cooling rates. The variation in the slope of the change in length (Δl) vs temperature curve indicates the phase transition event (temperature). The first and second inflection points of the cooling curves (Δl vs temperature) correspond to $\beta \rightarrow \alpha+\beta_{Zr}$ and $\beta_{Zr} \rightarrow \alpha+\beta_{Nb}$ transition temperatures. Figure 5.2 shows the trace of such points for Zr-2.5%Nb pressure tube material of the present investigation. From this study, β, ($\alpha + \beta_{Zr}$) and ($\alpha + \beta_{Nb}$) phase fields have been demarcated and shown in Figure 5.2. It can be observed that the ($\alpha + \beta_{Zr}$) regime starts at 891^{o}C for the sample cooled at the slowest cooling rate. Thus the highest $\beta \rightarrow \alpha+\beta_{Zr}$ continuous cooling transus temperature, 891^{o}C, for this alloy has been taken as the transition temperature. Therefore, heat treatment temperature was selected above and below this temperature for quenching from β and $\alpha+ \beta$ phase field respectively.

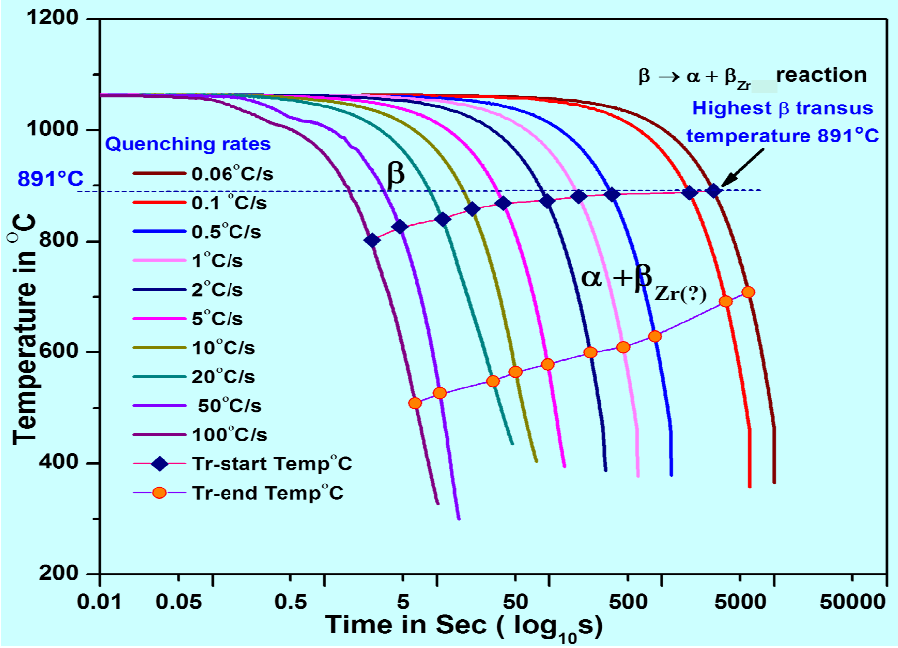

Figure 5.2: Cooling curve obtained from quenching dilatometer

5.3.2 Microstructural evolution

Microstructure after 1st extrusion

The extrusion process was performed at 800°C with an extrusion ratio of 2.3:1 to break the cast structure of the ingot and achieve homogeneity in structure and composition. 350mm dia ingot was reduced to 230 mm dia size billet. The resulting microstructure is shown in Figure5.3. Optical micrograph obtained from the longitudinal and transverse section of the extruded billet exhibited packets of lamellar α grains randomly oriented in all direction similar to those observed in the widmanstatten structure. The average width of the alpha grain was 1.5-2 micron and average length of a grain along axial-circumferential section was 200-300 μ and 100-150 μ in section defined by radial and circumferential directions. Beta phase was present at the α/α interface. TEM micrographs obtained at higher magnification showed β phase distribution more clearly. Microstructure also suggested dynamic recrystallization of the α grain. Refined and uniform microstructure suggested that cast structure was completely removed during hot extrusion process.

β quenched microstructure

Zr-2.5Nb alloy billets were heated at 1000°C and quenched in water to obtain fine α grain and homogeneity in composition, microstructure and texture. Optical micrograph showed fine needle like structure within the prior beta grains (Figure 5.4). Bright field TEM micrograph showed martensitic microstructure consisting of coarse lath martensites (Figure 5.4). The laths were oriented in certain crystallographic directions as observed in earlier studies [33,

71, 72]. The microstructure obtained confirmed that beta quenching achieved the objectives of this fabrication step.

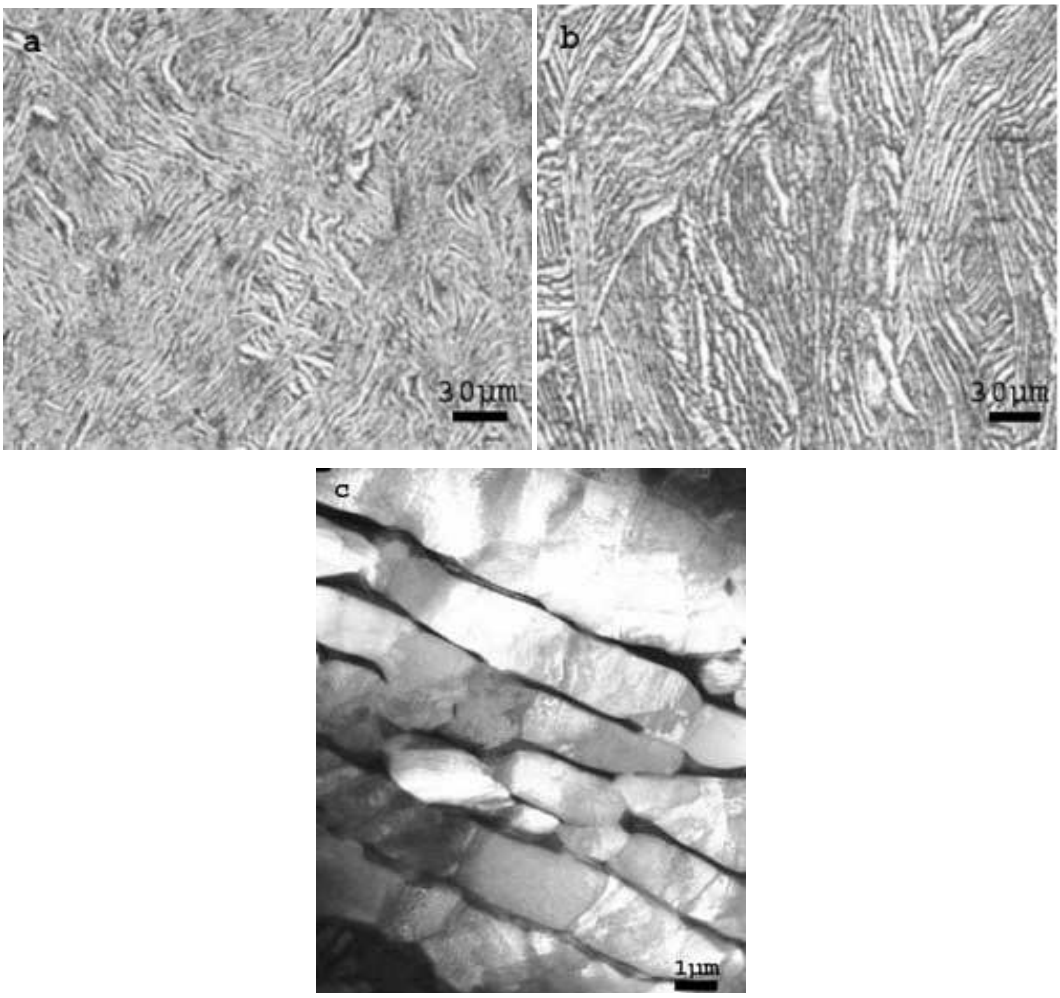

Figure 5.3: Micrograph after first extrusion (a) optical-longitudinal (b) optical-transverse (c) TEM-longitudinal

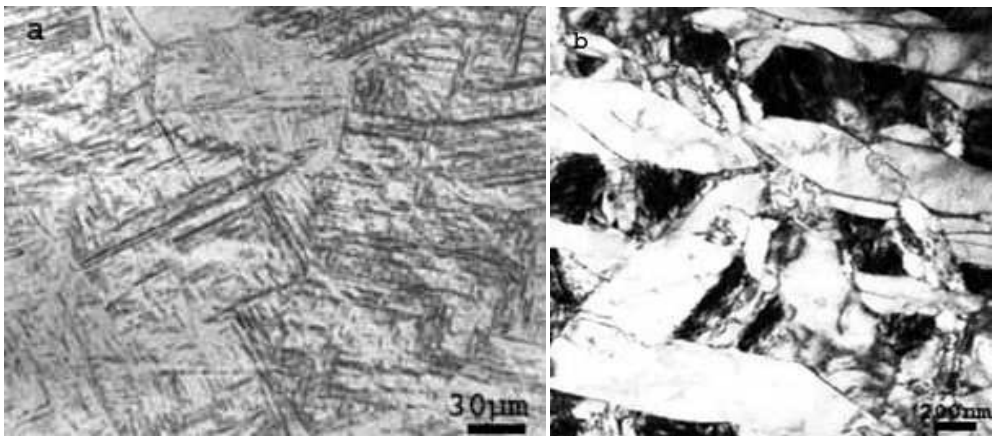

Figure 5.4: Microstructures after beta quenching (a) optical (b) TEM

Microstructure after second hot extrusion

Zr-2.5 Nb alloy tube is extruded at 800^{o}C, with an extrusion ratio of 7.3:1, from the billet in this fabrication step. The secondary electron micrograph images obtained from the longitudinal and transverse section in SEM is shown in Figure 5.5. During the extrusion process, the α grains become elongated in the axial direction of the tube and gets thinned in the radial direction. The longitudinal section exhibited α phase of lamellar morphology aligned along the extrusion direction. Transverse section exhibited α lamellae, whose width and thickness were not same. The average length, width and thickness of α lamellae were in the range of 15-20μm, 1-2.5μm and 0.3-0.5μm respectively. Beta phase was present as thin wafer between two α lamellae having average thickness of 0.02-0.05 μm. TEM micrograph of the longitudinal section revealed further finer details of microstructure (Figure 5.5). The α lamellae were found to consist of dynamically recrystallized α grains stacked in the extrusion direction.

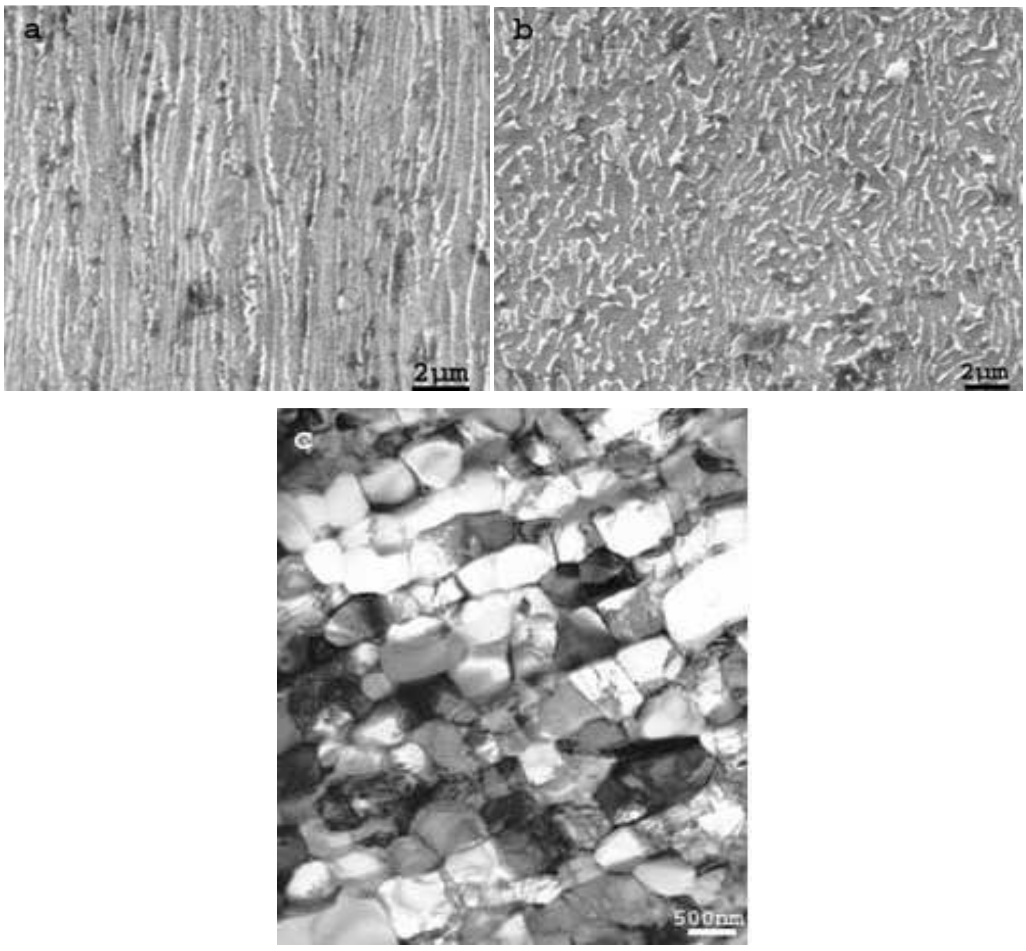

Figure 5.5: Microstructures after second extrusion (a) SEM-longitudinal (b) SEM-transverse (c) TEM-longitudinal

Microstructure after first cold deformation

The aim of this process was to reduce the wall thickness as well as OD (outer diameter) of the tube. Pilgering was used to impart 41% of cold work. SEM micrographs of the two cross sections of the tube are shown in Figure 5.6. Due to high amount of deformation, the microstructure could not be revealed clearly. However lamellar structure of the phase is still retained. The TEM micrograph also revealed presence of high dislocation density after this operation.

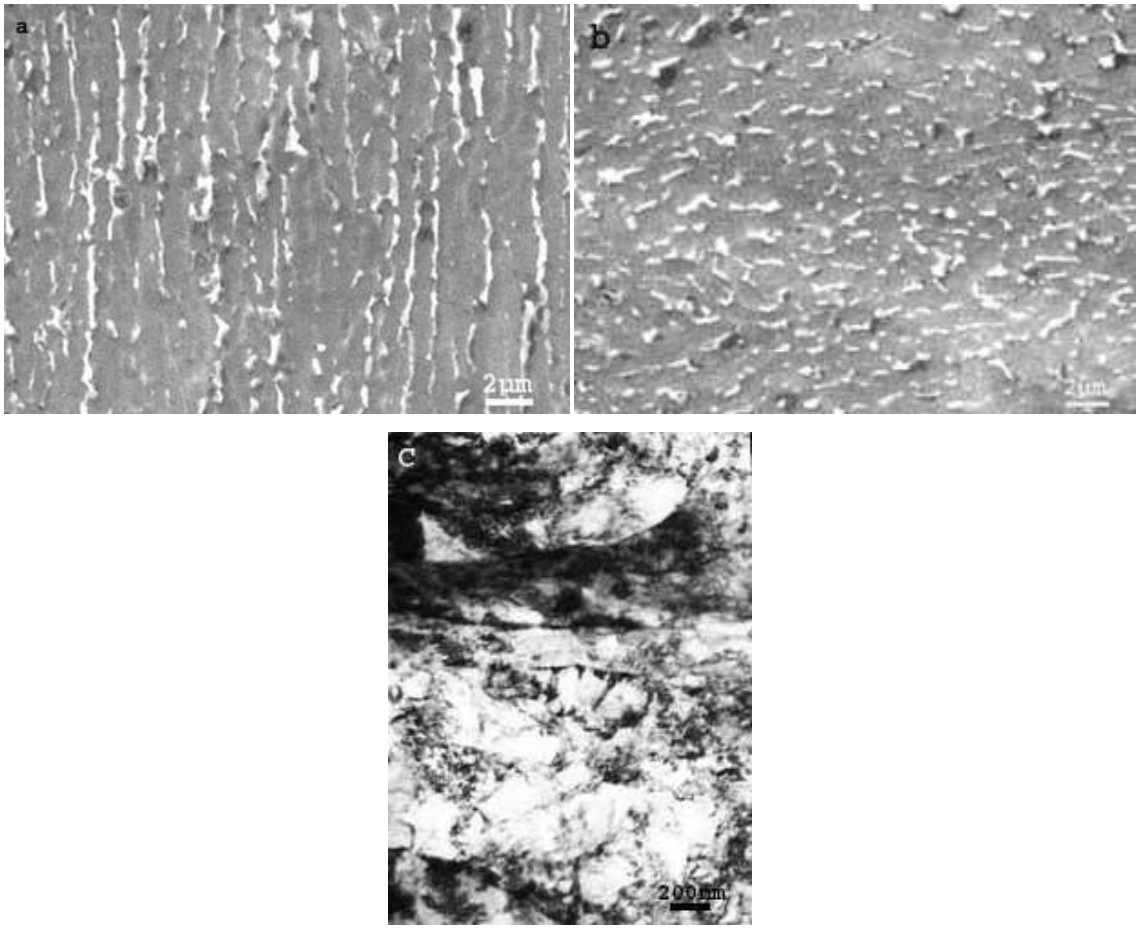

Figure 5.6: Microstructures after first pilgering (a) SEM-longitudinal (b) SEM-transverse (c) TEM-longitudinal

α+β quenched microstructure

One of the aims of the present study was to investigate the influence of quenching rate in determining the nature of transformation (diffusional and/or displacive) and resulting morphology of the products. Quenching treatments were carried out in a controlled fashion, using quenching dilatometer, to study the evolution of microstructures as a function of different cooling rates. It may be noted that, transformation from β phase field at different cooling rates has been reported in literature by many workers [33, 71, 101]. However, systematic studies on transformation from α+β phase field as a function of cooling rate are

far from being extensive in the open literature. In addition to cooling rate, effect of soaking temperature in the α+β phase field has been also examined in the present study.

The bright field TEM micrographs of samples cooled from 883°C at different cooling rates in argon are shown in Figure 5.7. All the samples showed primary α and transformed β phases. Samples cooled at the rate of 100°C/ sec and 50°C/sec showed predominantly martensitic transformation. At higher cooling rate of 100°C/sec, internally twinned martensite plates were observed, where as internally slipped martensite were the major features observed in samples subjected to relatively lower cooling rates of 50°C/s together with a minor fraction of primary α phase. The martensite plates were seen to have formed in self accommodating morphologies (see Figure 5.7), thus reducing the transformation strain energies.

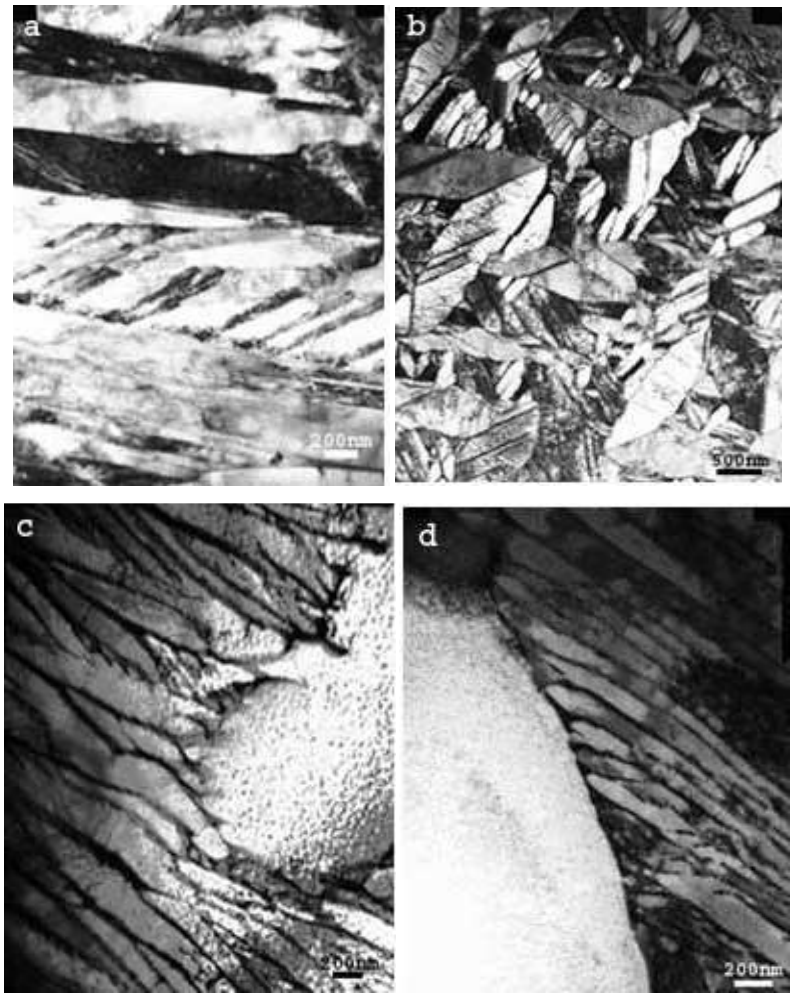

Figure 5.7: Microstructures after (α+β gas quenching from 883°C (soaked for 30 min) and quenching with cooling rates (a) 100°C/sec (b) 50°C/sec (c) 25°C/sec and (d) 10°C/sec

Below this cooling rate, transformed β product was observed to be Widmanstatten α +β. The β phase was present between the Widmanstatten lamellae. With decrease in the

cooling rate the width of the Widmanstatten plates became larger and their morphology progressively changed from being sharp straight lamellae to more irregular shaped lamellae. The morphological features are summarized in Table 5.2.

Table5.2: function of cooling rate (when cooled from 883°C)

Cooling rate (°C/sec)	phase	Microstructural features
100 50	α + Internally twinned martensite α +Internally slipped martensite	(sample quenched at 100°C/sec) Grain size prior β ~10-15 μm Grain size □α ~1-3 μm Primary α percentage ~ 3% Martensite plates 0.5-3 μm
25 10 0.5	α +Widmanstatten α +Widmanstatten α +Widmanstatten	(sample quenched at 0.06°C/sec) Grain size prior β ~10 μm Grain size α ~1-3 μm Primary α percentage = 5-8% Widmanstatten plates dimensions : Length = 10 to 20μm Width ~ 1-2μm

Figure 5.8 shows various microstructures obtained from gas quenching at 870^{o}C. As expected, the volume fraction of primary α phase increased with the lowering of soaking temperature. This effect was more pronounced in samples cooled with lower cooling rate. Comparison of Figure 5.7 and Figure 5.8 reveal that the probability of martensitic transformation is higher with lowering of soaking temperature for a given cooling rate. This may be attributed to higher Nb content in the β phase at the lower soaking temperatures which increases the driving force for the martensitic transformation. Martensite could be obtained even at 25^{o}C/sec cooling rate. This is also true for observation of higher incidence of internally twinned martensite. Since martensite was forming at lower temperature matrix became stronger and hence promoted the formation of internally twinned martensite. The widmanstatten α plates became finer with lower soaking temperature and all the other observations were similar to those observed at 883^{o}C. The summary of microstructural observations is given in table 5.3. On the basis of these observations it may be concluded that

in order to obtain primary α and martensitic microstructure after α+β quenching, a minimum cooling rate is required which is a function of soaking temperature.

It was shown in earlier reports [7, 8, 29] that the properties of fabricated tube (crystallographic texture, mechanical etc) are strong functions of the amount of primary α (after quenching treatment) phase present in the microstructure, which in turn is dependent on the soaking temperature in the α+β phase field. In the present study, amount of primary or retained α phase has been determined through SEM in the gas quenched and water quenched samples, after soaking at different temperatures and the details are given in Table 5.2 and 5.3.

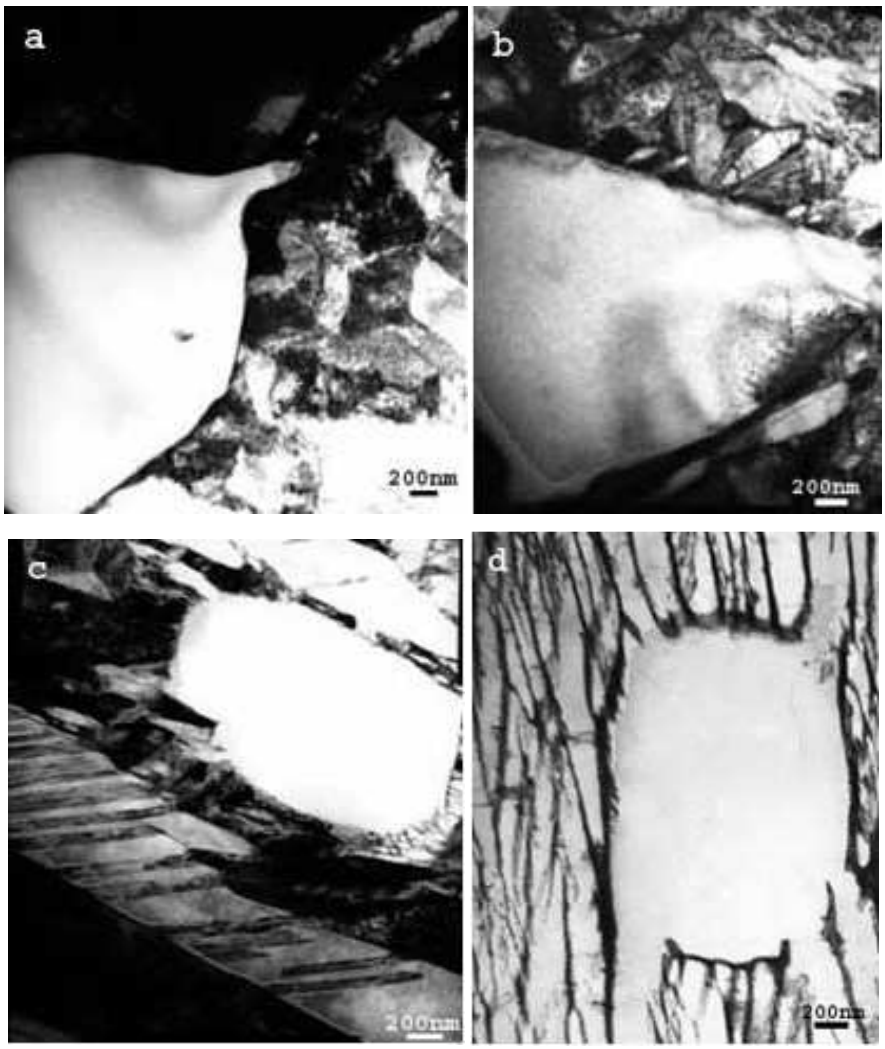

Figure 5.8: Microstructures after (α+β) gas quenching from 870°C (soaking for 30min) and quenching with cooling rates (a) 100°C/sec (b) 50°C/sec (c) 25°C/sec and (d) 10°C/sec

Table 5.3: Microstructure details as a function of cooling rate (when cooled from 870°C)

Cooling rate (°C/sec)	phase	α vol. frac (%)
100	α + Internally twinned martensite	15-20
50	α +Internally slipped martensite	15-20
25	α + slipped martensite	15-20
10	α +Widmanstatten	15-25

On the basis of the results obtained during controlled heat treatment performed in quenching dilatometer, 883°C was selected as soaking temperature and water as quenching medium for α+β quenching operation for large dimension tube (100 mm OD X 4.5 mm WT X 500 mm length). Quenching was performed after heating in a horizontal furnace. The SEM and TEM micrographs of the quenched sample are shown in Figure 5.9. From SEM micrograph the primary α volume fraction was found in the range of 20-25%. The primary alpha volume fraction was expected to be around 5% under controlled quenching conditions as per the dilatometer study. However, the observed higher values can be attributed to the larger volume of material compared to the sample size in dilatometer and also longer transfer time from the furnace to the quenching medium resulting in lowering of quenching temperature. TEM micrographs obtained at higher magnification revealed the transformed β microstructure. It could be seen that all β phase has transformed to the lath martensite. α+β quenched microstructure consisting of fine martensite phase along with 20-25% primary α volume fraction were used for further processing as described in the fabrication flow chart (Figure 5.1).

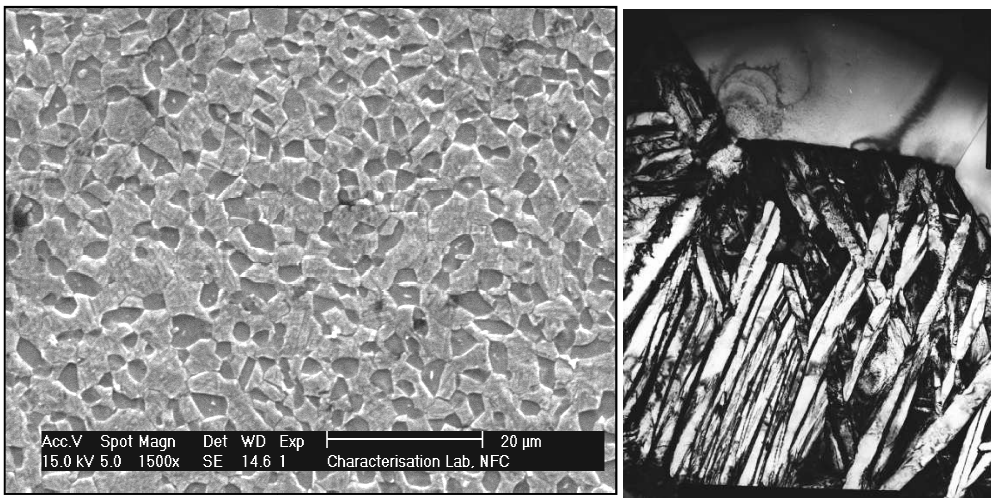

Figure 5.9: Microstructures after (α+β) quenching of first pass pilgered Tubes (a) SEM micrograph and (b) TEM micrograph

Microstructure after 2nd stage deformation

The α+β quenched samples were cold deformed (by pilgering) to the extent of 23%. The objective of this cold deformation process was to achieve the final dimension of the tube of acceptable quality. Additionally during this fabrication stage a complex network of dislocations is introduced in both primary α and martensitic phases in α +β quenched sample. TEM micrograph revealed the presence of such defect structure (Figure 5.10).

Figure 5.10: TEM longitudinal micrograph after second pass pilgering

Microstructural evolution during aging

One of the consequences of above two thermomechanical treatments (quenching and deformation) is the creation of a large number of nucleation sites for fine precipitation of β_{Nb} phase. Interfaces of fine martensitic microstructure provided large volume fraction of nucleation sites. Cold deformation of martensitic microstructure resulted in considerable increase in the dislocation density and dislocation substructure. These resulted in dislocation enhanced diffusion by pipe diffusion mechanism, thus leading to precipitation of β_{Nb} from the supersaturated martensitic phase during subsequent aging process. Therefore an ageing treatment was given below monotectoid temperature (610^{o}C) to obtain fine β precipitates having composition close to equilibrium along with retained primary α. Two different ageing temperatures (540^{o}C and 515^{o} C) below the recrystallization temperature were used in the present study after the 2nd pilgering operation (See Figure 5.1). The microstructures are presented in figure 5.11 and 5.12. Some of the salient observations from theses microstructures are (a) no recrystallization of the microstructure at 515 as well as 540^{o} C (b) Fully recovered structure at 540^{o}C for 24h where as only partial recovery (60 to 70%) at 515^{o}C for 24h (c) complete tempering of martensite at 540^{o}C, while partial tempering of the same at 515^{o}C (d) in the case of sample aged at 515^{o}C for 24h, small β precipitates (size less

than 15nm) were observed only at the α/α lath interface (e) no appreciable precipitation of β particles within primary α at both aging temperatures of 540^{o}C and 515^{o}C.

Compositional analysis of the β phase was carried out by Energy Dispersive Spectroscopy (EDS) in TEM. The average composition in sample aged at 515^{o}C was showing 40-50wt%Nb whereas, samples aged at 540^{o}C was showing 75-80%Nb. This study thus shows that a temperature of 540^{o}C is required to attain equilibrium concentration of Nb (85%) in β precipitates during aging for a period of 24Hrs. In other words, aging treatment at 515^{o}C for 24 Hrs, may lead to higher probability of compositional and associated microstructural changes under reactor operating conditions.

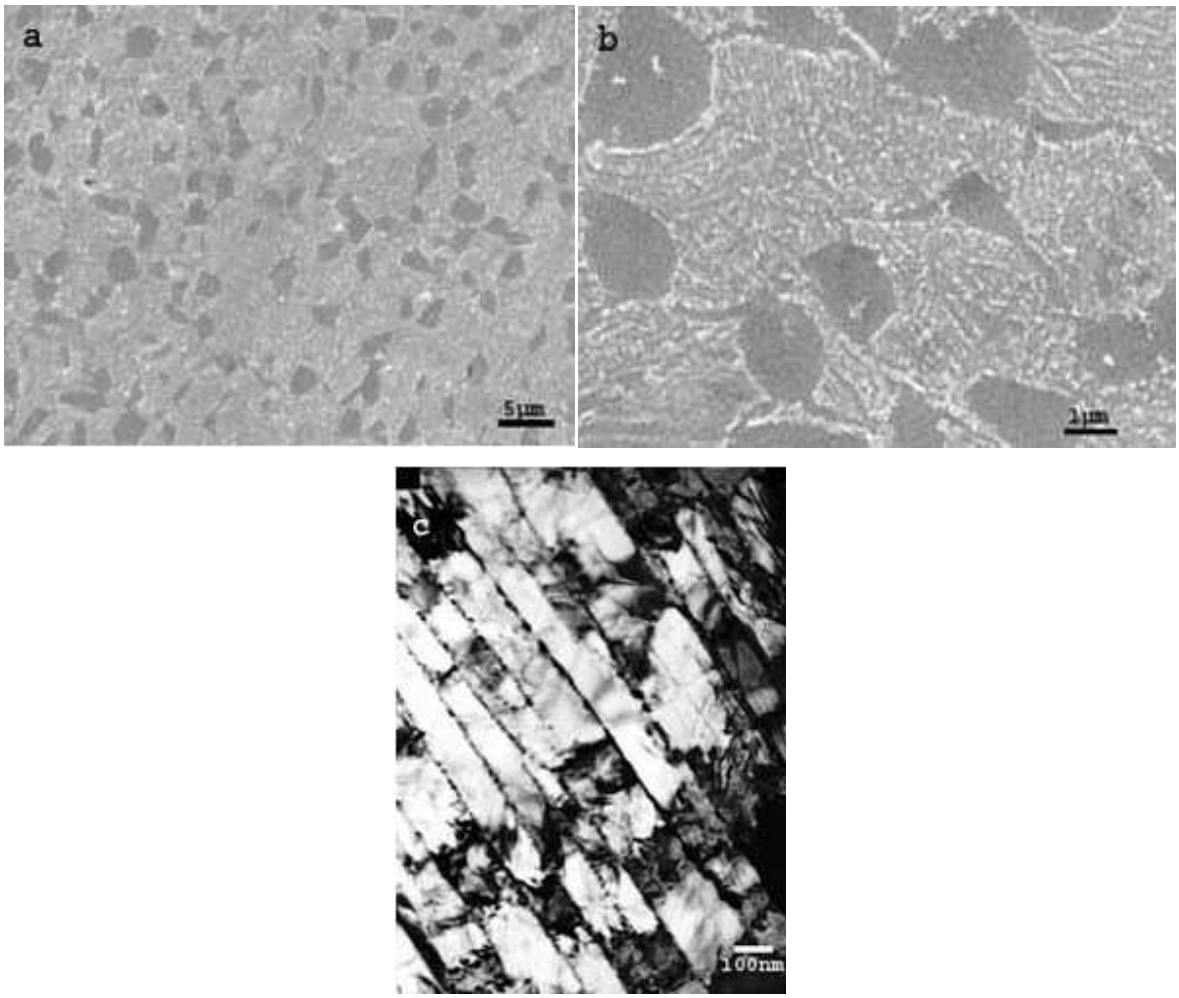

Figure 5.11: Micrographs after water quenching from 883°C (soaked for 30 min) and aged at 515°C (24 hrs) (a) SEM-longitudinal (b) SEM-transverse (c) TEM-longitudinal

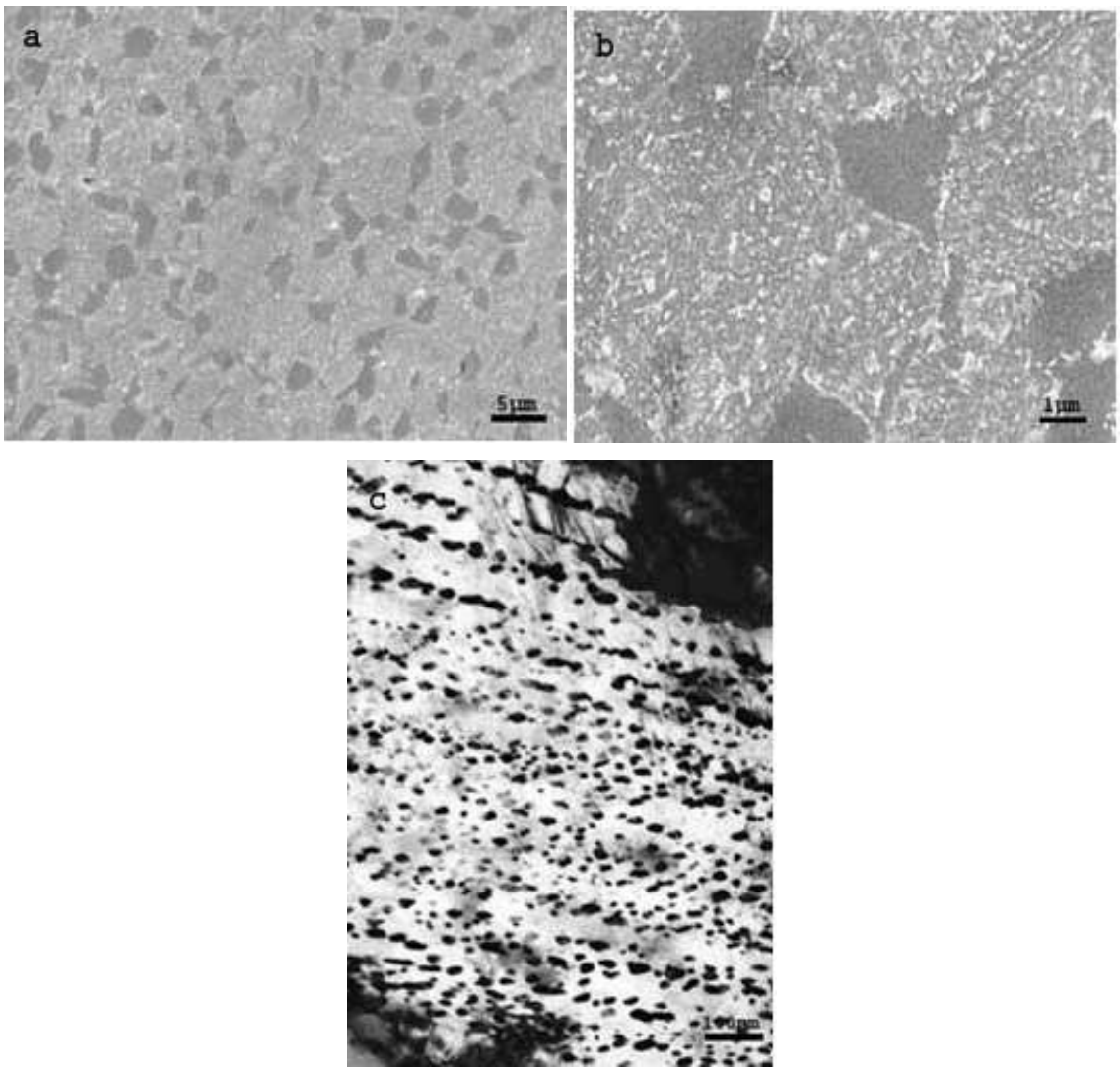

Figure 5.12: Micrographs after water quenching from 883°C (soaked for 30 min) and aged at 540°C (24 hrs) (a) SEM-longitudinal (b) SEM-transverse (c) TEM-longitudinal

Finally autoclaving treatment was carried out at 290^{o}C for 120 hrs, which did not modify the microstructure to any noticeable extent (figure 5.13).

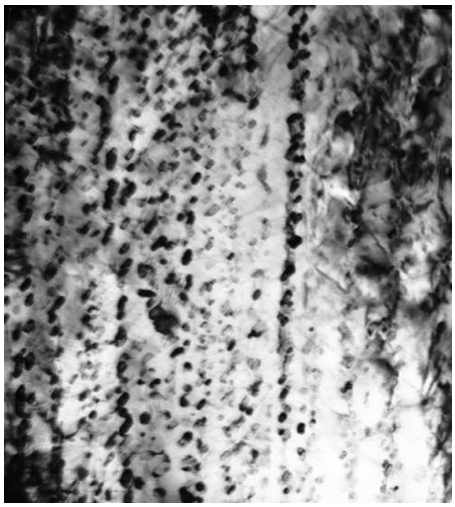

Figure 5.13: TEM micrographs after Autoclaving (2900C/120 hrs)

5.4. Mechanical properties

Table 5.4 shows the mechanical properties of the final tubes that were processed by water quenching followed by cold work and ageing (Figure 5.1). The mechanical properties were evaluated for the two ageing conditions. Comparing these with the cold worked pressure tube (table 5.4), it can be seen that mechanical properties in all the three cases are nearly in the same range. The only exception being the higher YS value at 300^{o}C in the case of tube aged at 540^{o}C for 24hr.

Table 5.4: Mechanical Properties of Full Scale Heat Treated Pressure Tube Spools (90.25mm OD X 3.8mm WT)

Tube Condition/Mech properties		**UTS(MPa)**		**YS(Mpa)**		**% EL**	
		RT	HT (300^{0} C)	RT	HT (300^{0} C)	RT	HT (300^{0} C)
HT	Ageing						
883^{0} C/30m	540^{0} C/24 h	749	494	581	468	10	18
883^{0} C/30m	515^{0} C/24 h	770	497	560	377	13	18.5
CWSR PRESSURE TUBES (TYPICAL VALUE)		735	502	553	383	16	23.8

In case of sample aged at 515°C the UTS value is noticeably higher than the sample aged at 540° C. This observation may be explained in following manner. The aged microstructure in both cases would have well dispersed dislocation structure in both cases (though their density might be larger in case of partially recovered 515°C aged sample) so that they are expected to have nearly similar YS at RT (room temperature) (which indicates onset of plastic flow). However, the fine distribution of small β particles act as effective dislocation sources in case of 515°C aged sample thus leading to higher work hardening rate in comparison to 540°C sample and giving rise to higher UTS value.

At higher temperature (300°C), thermally assisted movement of dislocations overcoming obstacles (β particles) would determine the mechanical properties. The resistance to the movement would be weaker when the size of the particle is small. Thus, sample aged at

515°C having smaller β particles would show lower YS. In the case of sample aged at 540°C due to larger particle size and higher particle density, initial dislocation motion is rather difficult thus accounting for the observed higher YS. However, for the similar reasons with the progress of the deformation dislocation multiplication would become the dominant factor in sample aged at 515°C. This would result in more strain hardening eventually leading to similar UTS value as that of sample aged at 540°C.

Thus aim of the present study to produce fine grained microstructure with fine precipitates of equilibrium β_{Nb} phase with similar mechanical properties could be achieved.

5.5. Textural evolution

Table 5.5 lists the crystallographic textural evolution as characterized by Kearns orienation parameter (f), which represents the fraction of basal poles of hcp alpha phase oriented in a given direction. The texture after second extrusion was predominantly basal poles oriented in the transverse direction as reported in the earlier studies [53, 102, 103]. In the present study, effect of quenching rate on the texture evolution has been examined. The tubes were soaked at 883^{o}C, and quenched using argon gas and water. Water quenching was performed in horizontal as well as vertical type of furnaces. In the case of former, sample transfer time was longer and effective cooling rate was lower than the vertical furnace. The texture results for all the three differently quenched samples are given in table 5.5.

Table 5.5:Texture coefficient in three principle directions of the tube

Condition	f_R	f_T	f_L
After second extrusion	0.29	0.61	0.10
As (α+β) water quenched (883^0 C/30 Mins) (effective higher cooling rate)	0.30	0.33	0.37
As (α+β) water quenched (883^0 C/30 Mins) (effective lower cooling rate)	0.38	0.49	0.13
As (α+β) Argon quenched (883^0 C/30 Mins)	0.43	0.47	0.10
As aged 540^{0}C/24 Hrs, (after WQ)	0.36	0.50	0.14
As aged 515^{0}C/24 Hrs, (after WQ)	0.37	0.51	0.12
Cold worked pressure tube	0.28-0.32	0.60-0.65	0.07-0.012

In the case of gas quenched and water quenched tubes in the horizontal furnace it could be seen that (α+β) quenching had resulted in some rotation of the basal poles about the axial direction to make transverse and radial fraction of the basal poles nearly similar with low fraction of the basal poles oriented along the axial direction. Considerable difference in texture in the above two cases could not be observed. Lack of significant differences in the textural developments between water (horizontal furnace) and gas quenched samples, although the former one showed martensitic structure and later one showed Widmanstatten structure, suggested that mode of transformation (displacive in case of water quenching and largely diffusional in case of gas quenching) has minimum role in the determination of the quenched texture. A recent study has shown that irrespective of the cooling rate, the orientation relationship between parent β and product α phase is strictly burgers[104]. Hence it is expected that cooling rate alone may not affect the resulting texture. However, it can be observed that tube quenched with higher effective cooling rate (quenched in vertical furnace) exhibited nearly random texture. The major difference between the previous two cases and this one is the volume fraction of the primary α phase (25 to 30%, in gas quenched and horizontal furnace quenched and 5 to 10%, in water quenched in vertical furnace). This observation shows that some degree of basal poles alignment along axial direction happens during quenching with lower primary alpha volume fraction sample. This is equivalent to quenching from higher soaking temperatures. This observation is in line with the results of the previous study [80, 105]. This has been attributed to the presence of higher amount of β phase at the higher soaking temperature and subsequent to quenching produces randomly oriented α', giving rise to bulk random texture.

However, further deformation and aging treatments of the water quenched samples (horizontal furnace) did not change the texture substantially. The tubes aged in two different conditions (540°C and 515°C) exhibited nearly similar texture values. This suggested that deformation as well as aging treatment did not modify texture significantly.

5.6. Conclusions

A modified heat treated fabrication route for the production of pressure tube was explored. Effect of the process parameters on the microstructure was studied. Some of the important conclusions reached in the present study are summarized below:

- The first extrusion process produces uniform structure and completely breaks the cast structure. Second extrusion produces fine ($\alpha+\beta$) lamellar structure.
- During $\alpha+\beta$ quenching the soaking temperature determines the primary α volume fraction. Required cooling rate to obtain martensitic microstructure increases with soaking temperature.
- Ageing at 540^{o}C resulted in fine β_{Nb} precipitates of equilibrium composition, whereas the β_{Nb} phase composition did not attain the equilibrium composition after ageing at 515^{o}C.
- Mechanical properties of the finished heat treated pressure tube (aged at 515C/24h) produced with the present route were similar to the cold work pressure tube. Tube produced with 540C/24h aging exhibited substantially higher YS value at reactor operating temperature (300C)
- The bulk texture at different stages of fabrication was evaluated. The effect of quenching rate and the retained primary α volume fraction was studied. The effect of the later was found to be more dominant. Further cold working and ageing resulted in insignificant modification of texture of the pressure tube.

Chapter 6
A numerical study of the effect of extrusion parameters on the properties of extruded Zr-2.5Nb pressure tubes

6.1. Introduction

Typically, textural and microstructural control [10, 25, 26] in pressure tubes is achieved by appropriate thermo- mechanical fabrication processing [5-11, 34, 56, 77, 106, 107]. In case of Zr 2.5Nb pressure tubes fabrications, one of the most important fabrication steps that has a high bearing on the final properties of the tube is hot extrusion [84, 108, 109]. Previous studies show that the crystallographic texture produced during the hot extrusion stage largely remains unaltered even after further cold work [110]. In addition, morphology and distribution of the alpha and beta phases also get greatly influenced during this hot extrusion stage only. These microstructural and textural features are influenced by the actual temperature and stress distribution during the hot extrusion process. In addition, extruded product quality in terms of variation from leading end to tailing end, surface cracks, ovality, etc also depend on the presence of steep temperature gradients during the hot extrusion. Hence a detailed knowledge of the role of process parameters such as billet preheat temperature, extrusion speed, extrusion ratio etc. on the temperature and stress distribution during the hot extrusion process can help tailor the process [8, 24, 52, 78]. However, the design and control of the experiments to acquire such information during hot extrusion process is rather difficult [78, 80, 81].

An alternative approach could be application of computational/numerical analysis of the extrusion process for the process optimization. In the recent past the three-dimensional finite element analysis for hot extrusion is being pursued in case of aluminium based materials [111-115]. Such studies in case of the Zr based alloys seem to be rather limited in the open literature, forming the motivation to present study. Some of the key parameters of the extrusion process such as ram velocity, billet pre-heat temperature, fillet radius and reduction ratio, have been studied for their role in determining the overall temperature distribution during hot extrusion, requirement of ram force etc.

6.2. Hot extrusion model

The three main types of FE methods that are utilized in extrusion simulation are Lagrangian, Eulerian and Arbitrary Lagrangian Eulerian (ALE). The ALE method is essentially an arbitrary combination of the Lagrangian and Eulerian methods and attempts to bring the advantages with both Lagrangian and Eulerian formulations together. In an ALE formulation the displacements of material and mesh are decoupled and the mesh can move independently of the material. The ALE formulation is ideally suited for modeling of fluid-structure interaction and motion of free surfaces in fluid mechanics. Since the heavy plastic deformation involved in extrusion resembles fluid flow, ALE method is well suited for extrusion simulations. The present work uses HyperXtrude®, a commercial simulation software module dedicated to simulation of extrusion process using the ALE approach. The models were prepared using a structured mesh with appropriate biasing to maintain accuracy and continuity across the faces of different elements. Figure 6. 1 shows the geometry of the model along with the various boundaries and the way interactions with surrounding are modeled. As can be seen, the model is made up of different zones representing the container portion, die cavity, die land and exit region. The interaction of the billet material with the surroundings is modeled through appropriate heat transfer and friction boundaries as show in the figure. Error in heat balance and mass balance at successive simulation time steps were kept below 5% and 1% respectively in order to achieve good convergence in a reasonable time frame.

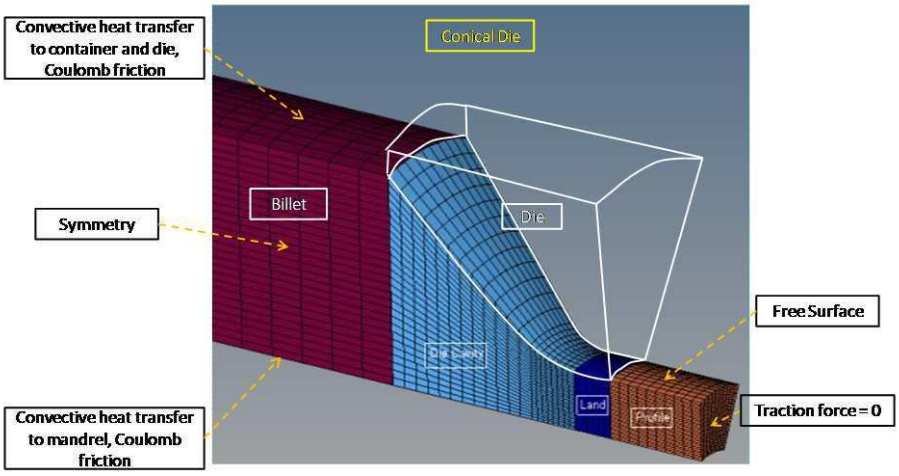

Figure 6.1: Schematic explaining the meshing scheme, various components of the model geometry and various interactions of the model with the bounding surfaces.

6.2.1. Mathematical formulation

The fundamental equations that govern flow and heat transfer of incompressible viscous fluids are derived from principles of conservation of mass, momentum, and energy. These equations are written in terms of primitive variables (velocity, pressure, and temperature) with reference to an Eulerian frame, i.e., a space-fixed system of coordinates through which the fluid flows.

$$\nabla \cdot U = 0 \tag{1a}$$

$$\rho (U \cdot \nabla) U = \nabla \cdot (\sigma) \tag{1b}$$

$$\rho C_P \, U \cdot \nabla T = \nabla \cdot q + \varphi \tag{1c}$$

Where, U is the velocity vector, σ is the total stress tensor, T is the temperature, ρ is the mass density, C_P is the specific heat of the fluid at constant pressure, q is the heat flux vector, and φ represents internal heat generation rate due to viscous dissipation.

6.2.2. Constitutive model

For viscous incompressible fluids, the components of total stress tensor (σ), can be represented as the sum of viscous stress tensor (the deviatoric part of the stress tensor) (τ), and a spherical hydrostatic pressure (P).

$$\sigma = \tau - P \tag{2}$$

The material behavior is specified by the constitutive relations for the viscous stress tensor, (τ) and the heat flux vector (q) by the following equations [28].

$$\tau = 2\mu\gamma \tag{3a}$$

$$\gamma = [(\nabla U) + (\nabla V)]^T \tag{3b}$$

$$q = -k\nabla T \tag{3c}$$

In the above equations, μ is the viscosity, and k is the isotropic thermal conductivity of the material. This viscosity is a function of strain rate and temperature of the material and described using sine-hyperbolic inverse relation:

$$\mu = \frac{\sigma}{\sqrt{3}\dot{\varepsilon}} \tag{4a}$$

$$\varepsilon = \frac{2}{3}[\gamma : \gamma]^{\left(\frac{2}{3}\right)} \tag{4b}$$

Where, σ is the flow stress, and $\dot{\varepsilon}$ is the effective strain rate, α is stress multiplier, n is stress component, Z is Zener-Hollomon parameter, Q is Activation Energy, R is Universal Gas Constant and θ is the temperature. The flow stress for any metal depends on an internal state variable representing the material microstructure. An accurate

description of the flow stress requires solving an evolution equation, which governs the internal state variable. In case the flow stress values cannot be fit into a single constitutive equation, as is the case for Zr-2.5Nb alloys, tabulated experimental data for flow stresses at different temperatures, strains and strain rates has to be utilized as explained in section 6.2.3.

Following are the boundary conditions assigned to various regions of the simulation model (see figure 6. 1):

- Convective Heat Transfer boundary: All tool face boundaries are assigned convective heat transfer boundary, i.e., heat removal from these faces is through convection.
- Friction Boundary: When shear stress over contact surfaces exceeds critical shear stress, material starts to flow.
- Inflow Boundary: A constant velocity and temperature boundary condition is assigned at billet ram face.
- Free Surface Boundary: Free surface boundary is assigned at profile surface. This boundary is assigned an insulated boundary i.e. q (heat flux) = 0.
- Outflow Boundary: This boundary is assigned to profile face.
  Traction forces = 0 (as the extrudate is not pulled out of the die),
  Displacement = 0 (as extrudate is free to expand),
  Heat Flux = 0
- Symmetric Boundary: This is assigned to symmetric faces.

Mathematically, these are expressed as:

Billet-Ram Interface :

$$U = U_{Ram}\,;\, T = T_{Ram} \tag{6}$$

Billet-Container Interface :

$$\tau_S = \mu\sigma_N\,;\, T = T_{Container} \tag{7}$$

Die Face :

$$\tau_S = C(U\text{-}U_{Tool})\,;\, T = T_{Container}\,; \tag{8}$$

Bearing Surface :

$$\tau_S = C(U\text{-}U_{Tool}) \tag{9}$$

Free Surface :

$$\sigma \cdot n = 0 \tag{10}$$

6.2.3. Material properties used for simulations

The accuracy of the results of numerical simulations is determined by the extent to which the subject material and the environment are accurately represented in the model. The main inputs to any deformation modeling code are material properties and boundary conditions. As for the mechanical properties of the material, the flow stress data as a function of strain, strain rate and temperature have to be introduced to the FEM software. Conventionally, constitutive equations such as power law or sine-hyperbolic inverse law are utilized by fitting the experimental flow property data to suitable equations[116]. In the present case of Zr-2.5Nb alloys, flow stress values were experimentally determined for a range of strains, strain rates and temperatures. However, these flow stress values could not be fitted to any single constitutive equation. This is on account of the fact that, within the range of temperatures of interest, complications due to phase transformation, variation of relative amounts of phase with respect to temperature render fitting mechanical properties to a single equation difficult. Hence, a Look-Up Table (LUT) was used which had experimentally measured flow stress values for compression tests at a number of temperatures, strains and strain rates (see table 6.1).

Table 6.1: Look-Up Table (LUT) showing different experimental flow stress values for different temperatures, strains and strain rates. Flow stress values for only one strain value are shown here.

`Flow stress (MPa) at temperature (°C)								
Strain	**Strain rate**	**650**	**700**	**750**	**800**	**850**	**900**	**950**
0.5	0.001	72.7	50.3	33.5	15.1	13.8	10.9	8.1
	0.01	122.3	80.8	61.8	36.5	27.8	18.2	16
	0.1	143	118.4	75	66.4	44.2	30.2	25.8
	1	332.8	180.1	129.7	92.7	60.4	45.7	39.3
	10	303.1	234.6	179.6	120.5	88.1	78	70.7
	100	286.3	264.1	222.4	151.2	120	100.7	87.3

These experiments were carried out on a Gleeble Thermo-mechanical Simulator. Uniaxial compression tests on homogenized cylindrical samples were conducted over a range of temperatures 650-950°C (with a step of 50°C) and strain rates 0.001-100 s^{-1} using a compression test rig. The compression rig consists of high thermal conductivity grips. The sample was heated by direct resistance heating leading to uniform temperature throughout the sample. A graphite lubricant was used to minimize barreling and obtain a

uniform distribution of strain. The flow stress values for any intermediate values of temperature, strain and strain rate were calculated by trilinear interpolation scheme. The extrusion force required was plotted against the ram displacement. Such load profiles from simulations were compared to those obtained from actual experimental shop-floor data. The shop-floor ram-force data is recorded by an electronic data acquisition system. The set of friction and heat transfer coefficient values which showed the best fit to the experimental ram force profile (see figure 6.2) was chosen for further simulations.

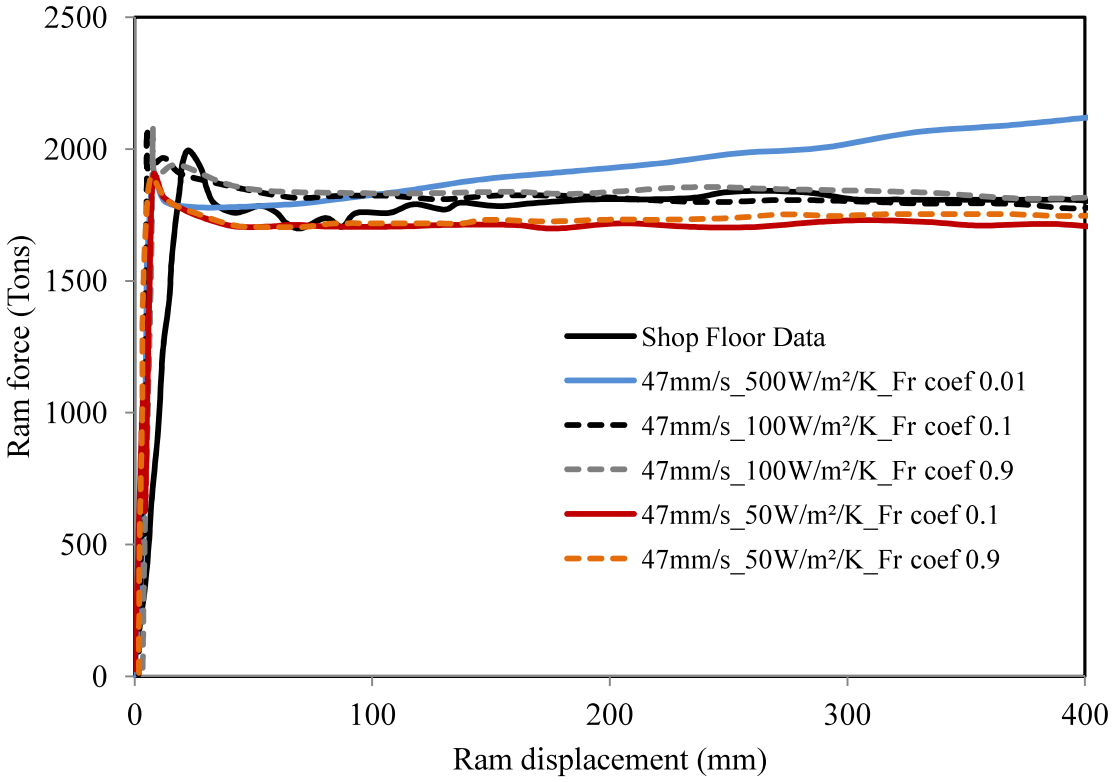

Figure 6.2: Optimizing convective heat transfer and friction coefficients to conform to experimental ram force curve represented by solid black line, "Shop Floor Data"

6.3. Simulations

The geometry of the extrusion die, punch and billet used for simulations is shown in figure 3. The dimensions of the billet were chosen to correspond to that of the one used in the actual pressure tube fabrication process at NFC, Hyderabad. In order to systematically bring out the role of the important process parameters (such as extrusion temperature, extrusion ratio, ram velocity, etc.) on the overall temperature distribution and hence the expected variability introduced across different regions (e.g., leading end and tailing end), simulations were carried out by varying these process parameters to cover

values both above and below values reported in literature [78, 80]. Since only one out of all the chosen process parameters can be varied to understand its influence, one has to choose a set of fixed values for remaining parameters. These fixed values were chosen based on the general values reported in the literature. These values are, ram velocity 30 mm/s, billet preheat temperature of 815°C (two phase region), included die angle of 90°C, reduction ratio of 14.44 and fillet radius of 10 mm. For every simulation run, the other invariant independent parameters were kept at the actual shop-floor values as mentioned above.

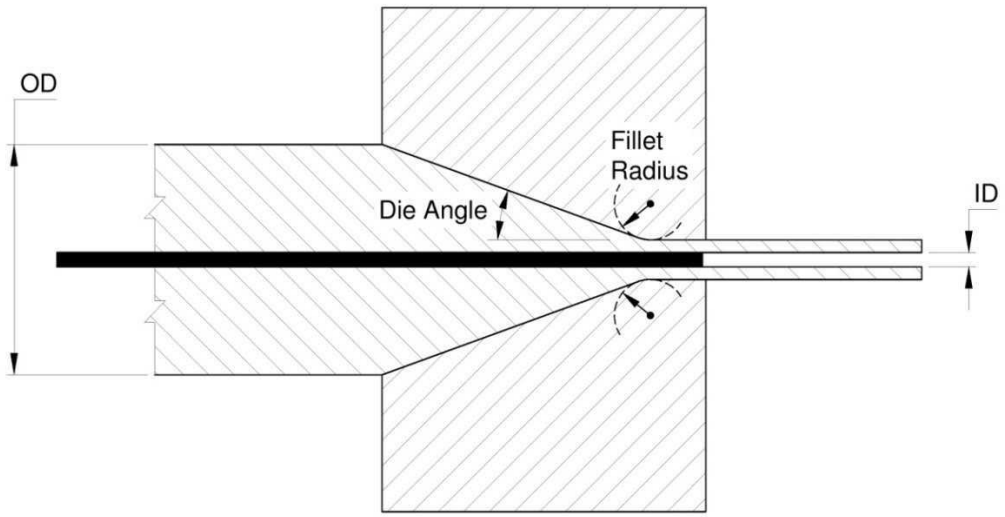

Figure 6.3: Schematic geometry of extrusion setup showing billet, mandrel, die angle, fillet radius, outer diameter (OD), inner diameter (ID), wall thickness (WT).

- Effect of ram velocity : OD 119 mm, WT 6 mm, billet preheat temperature 815°C, included die angle 90°, fillet radius of 10 mm, reduction ratio 14.44, ram velocities : 20 mm/s, 47 mm/s, 75 mm/s, 125 mm/s.
- Role of reduction ratio: OD 119 mm, ram velocity 30 mm/s, fillet radius of 10 mm, Billet preheat temperature 815°C , included die angle 90° reduction ratios: 6, 8, 10, 12, 14.44, 20.
- Effect of preheat temperature: OD 119 mm, WT 6 mm, ram velocity 30 mm/s,

included die angle 90°, fillet radius of 10 mm, reduction ratio 14.44, billet pre-heat temperatures 775 to 855°C at intervals of 10° C.

- Effect of fillet radius: OD 119 mm, WT 6 mm, ram velocity 30 mm/s, included die angle 90°, billet preheat temperature 815°C, reduction ratio 14.44, fillet radii: 1 mm, 5 mm, 10 mm, 20 mm.

Regions along the length of the tube were classified as leading and tailing ends. This was done based on the time based variation of temperature at the point of highest temperature (figure 6.4). The fillet region corresponds to the highest variation in temperature and subsequently highest variation in microstructure and thereby, properties. So, the temperature profile (mandrel to die, radially) at the fillet region is plotted at two time instants: once at the beginning of extrusion and once just before the end of extrusion. These represent the temperatures experienced by the leading end and the tailing end of the extrudate respectively. These temperature profiles are shown in figures 6.6, 6.13 and 6.15 for variations in ram velocity, pre-heat temperature and fillet radius respectively.

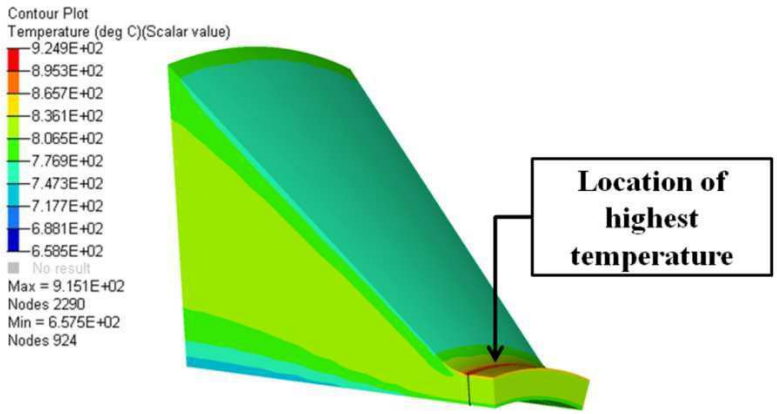

Figure 6.4: The temperature contours in a typical simulation. The location of the region of highest temperature is shown. The variation of this temperature with time is used to judge the expected variation in the leading and tailing end of the resulting extrudate.

6.4. Results and discussion

6.4.1. Effect of variation in ram velocity

Figure 6.5 shows the ram force variation with ram displacement for different values of constant ram velocities (30, 47, 75 and 125 mm/s), other parameters remaining constant at shop-floor values. For each ram velocity, the billet preheat temperature was kept at

815°C and the fillet radius was kept 10 mm. The required ram force, as expected, is seen to increase with the increase in the ram velocity (Figure 6. 5). It can be observed from the figure that peak ram force varied from 1836 tons for 20 mm/s ram velocity to 2337 tons for a ram velocity of 125 mm/s, an increase of 27% in peak ram force, signifying the importance of the ram velocity on the overall extrusion load requirements. Further, the experimentally measured force is observed to be reasonably closer to the simulated curve for a ram speed corresponding to 47 mm/s, particularly in terms of the peak force and steady state force, with a deviation less than 5% and 4% respectively. The measured force versus displacements curve does show some oscillations during transition from the peak force to steady state force mainly due to the variations introduced in the ram velocity under practical conditions of the extrusion which are rather difficult to incorporate in the simulations. Nevertheless, reasonably close predictions of the simulations for the two characteristic loads of the extrusion process (i.e., peak and steady state ram force) enable us apply the simulation results for the analysis of temperature profiles across billet during the extrusion process. The observed ram force versus velocity curves for this set of simulations, are the reflection of balance achieved between the two competing factors governing the force requirement. One is requirements of higher force arising out of application of higher strain rate deformation (for higher ram velocities) and the other is decreased force requirement resulting from increased temperature due to higher strain rate deformation corresponding to higher ram velocities, and lower heat losses due to lower residence time. Since the first factor dominates during the initial stage of the extrusion, one would expect more change in ram force as a function of ram velocity. This is clearly brought by the simulations which predict 27% of change in the peak rams force, in comparison to 17% of change in the steady state force requirement for the same change in the ram velocities. Apart from ram force variation, ram velocity is expected to influence the overall temperature distribution significantly. More importantly differences between the temperature profiles across a given cross section, can also be influenced which are important from the point of view of structural homogeneity and residual stresses. Figure 6. 6, is the depiction of the temperature profile across fillet region, at different times corresponding to the leading end and trailing end of the extrusion. As can be observed from the figure, as the ram velocity increases, the temperature profiles of leading end and tailing end tend to converge. Such a convergence implies the presence of a more homogeneous structure along the length of the tube / extrudate, since temperature is the defining parameter for microstructure development, stress state being nearly constant. But,

at the same time, this convergence comes at the cost of increasing ΔT , i.e., the temperature difference, across the cross section of the tube (mandrel to die). This may introduce heterogeneity across the thickness of the tube.

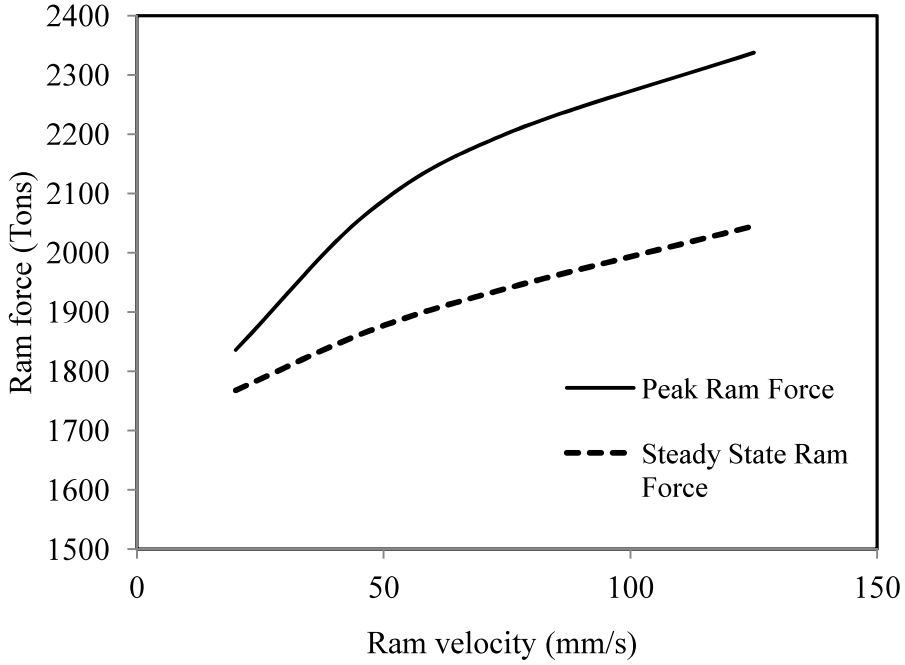

Figure 6.5: Ram force variation for various ram velocities.

Figure 6. 6 shows that higher ram velocities give rise to steeper temperature gradients across the cross section of a tube and the range of temperature difference between the front end and back end at any given cross section was found to be in the range of 100 to 140 K for the ram velocities considered in the present work. Conversely, simulations predict lower ram velocities should result in lower temperature and hence microstructural variations across any given cross section. In fact, low or negligible temperature and microstructural variations across tube cross section have been reported in literature [80] at low ram velocities, which is in direct agreement with our present simulation results. However, lower ram velocities also result in more pronounced chilling effect of ram and container coupled with decreased adiabatic heating as a consequence of lower strain rate deformations. It may be pointed out that previous works have reported a drop in ram side temperature of the work piece to the extent of 300K, at ram velocities of the order of $3 mms^{-1}$ using a work piece much shorter than what is being considered in the present study. This data when extrapolated to work piece of dimensions of the present study indicates a similar chilling effect of ram (see figure 6. 7). Two main points emerge out of the present discussion. (a) The temperature variation across the length is much more than across section at lower ram velocities coupled with higher residence time for

the work piece at any given temperature (b) In contrast, at higher ram velocities, temperature variation across cross section dominates that of the one across length, with much lower residence time of the work piece at any given temperature.

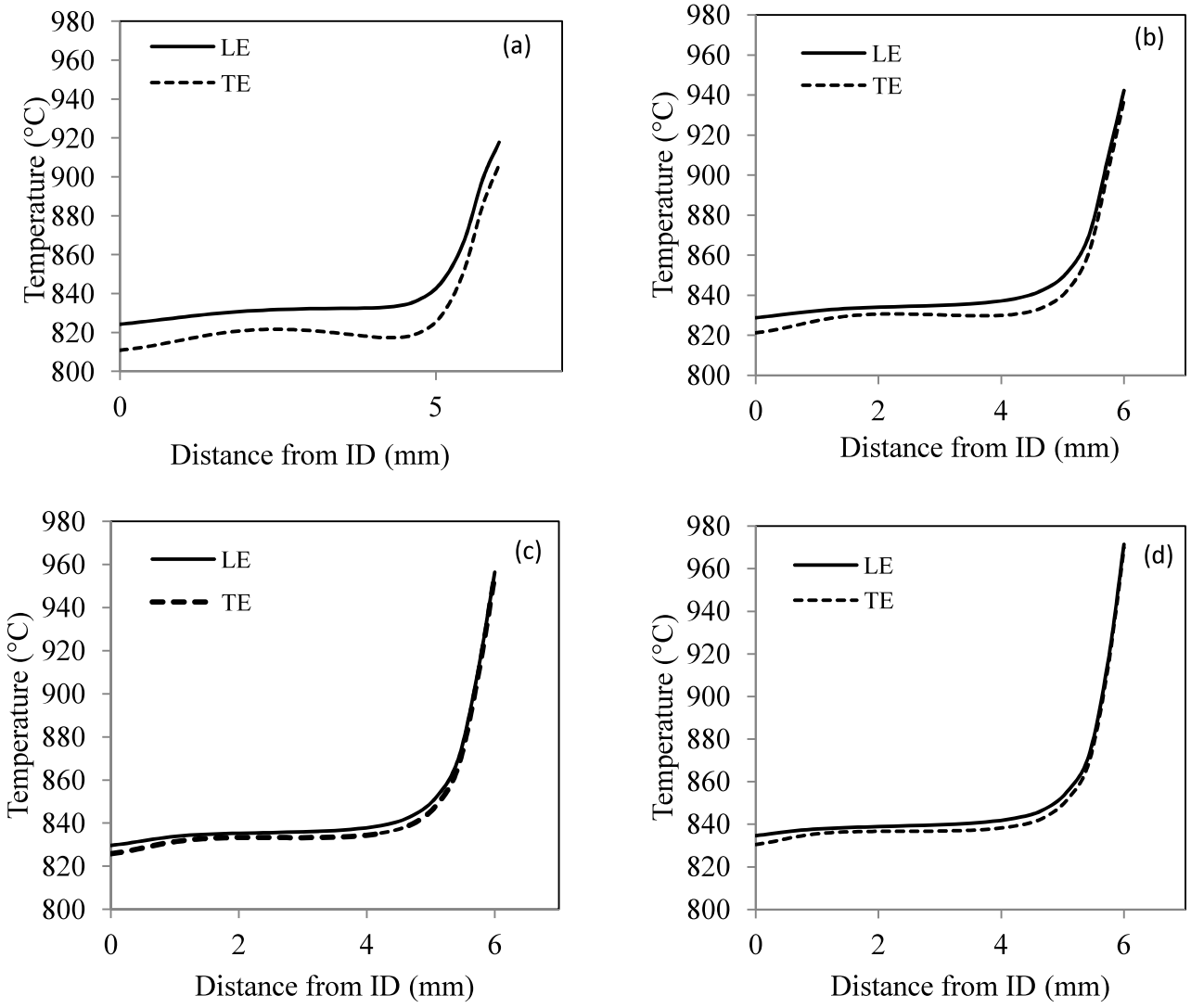

Figure 6.6: The leading (LE) and tailing end (TE) temperature profiles for ram speeds of (a) 20 mm/s, (b) 47 mm/s, (c) 75 mm/s and (d) 125 mm/s.

These observations, when viewed in the context of a well known sluggishness of $\alpha \rightarrow \beta$ transformation, point out that higher temperature variations across a given cross section resulting from higher ram velocities, may not translate in wide microstructural variation, due to small residence time available for microstructural changes. On the contrary, significant temperature variations across the length of the work piece at lower ram velocities may result in appreciable microstructural and textural changes across length of the extrudate. Experimental evidence from previous works also supports this premise. In

view of the detrimental effects of cross sectional heterogeneity on the performance of pressure tubes, imposition of low ram velocities seems advisable. However, ram stroke also contributes to adiabatic heat generation, i.e., heat generation due to plastic deformation. Also, the ram acts as a heat sink. Hence, very low ram velocities will contribute to chilling of the billet. This effect will be most dominant in the trailing end of the tube on account of longer residence time in the container. The microstructural effects of this leading end to trailing end temperature variation have been demonstrated in another study [80]. The present simulations show that hot extrusions carried out at higher ram velocities (20-125 mm/s) show much smaller variations from leading end to trailing end (see figure 6. 6). Though higher ram velocities lead to larger cross section variation, this variation is mitigated by the small residence time in the dies (≈15 sec).

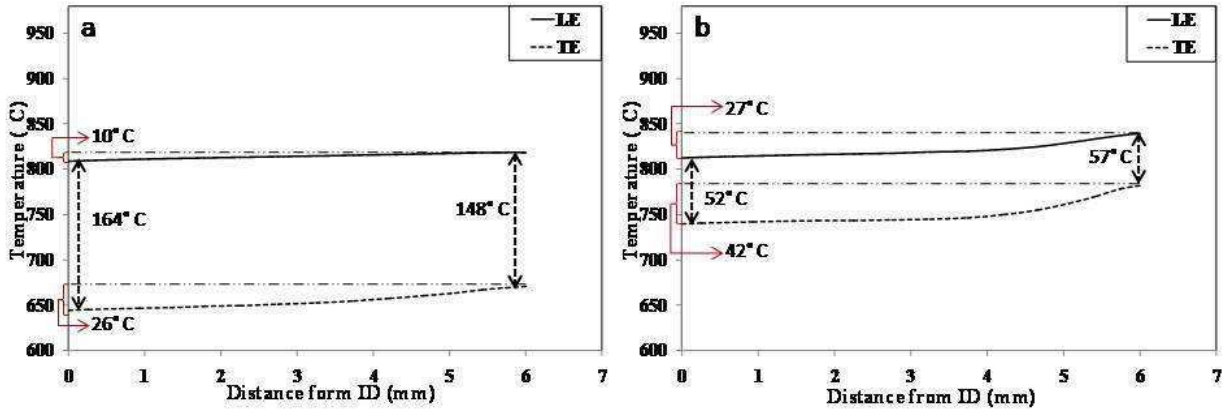

Figure 6.7:The leading and trailing end cross sectional temperature profiles at low ram velocities of (a) 1mms−1 and (b) 3mms−1 . At low ram velocities, the chilling effect of ram dominates the deformation heating, leading to larger temperature gradients along the length as compared to those across the cross section

6.4.2. Effect of variation in reduction ratio

Reduction ratio effectively denotes the amount of deformation that the work piece is subjected to during extrusion. Since, deformation work is the most energy intensive part of hot extrusion; one would expect that reduction ratio should have significant influence on the required extrusion force [117]. Figure 6. 8 brings out this strong dependence of ram force on the extrusion ratio. Though the application of a larger reduction ratio can give a thinner extrudate section (see figure 6. 9), large deformations have certain undesirable effects too. As shown in figure 6. 10, there exists a temperature gradient from the ID (mandrel) to OD (Die) cross section. In case of hot extrusion, two competing phenomena of heat transfer are in play. Firstly, the dies and the mandrel absorb heat from the billet / work piece; and secondly, the work- piece gets locally heated due to deformation work done and

frictional effects.

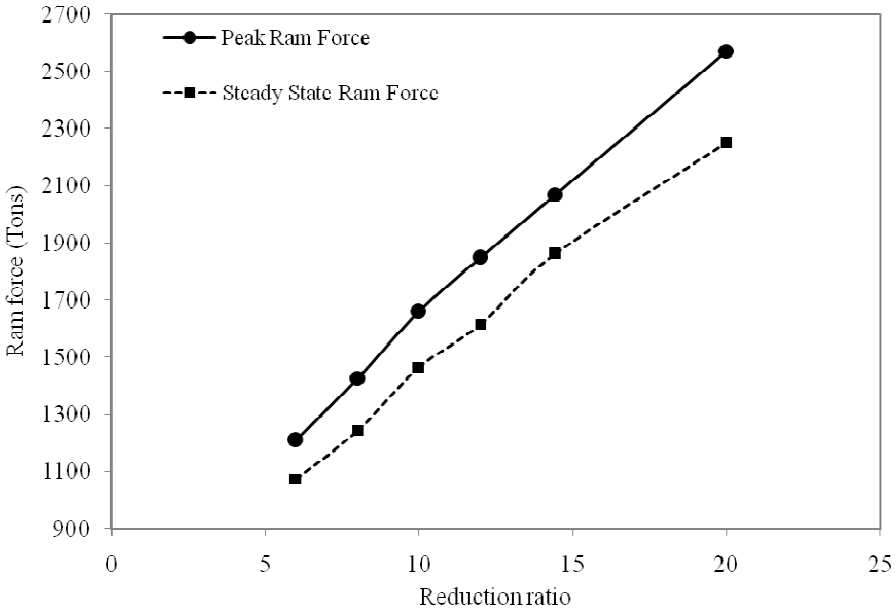

Figure 6.8:Ram force variation for different reduction ratios.

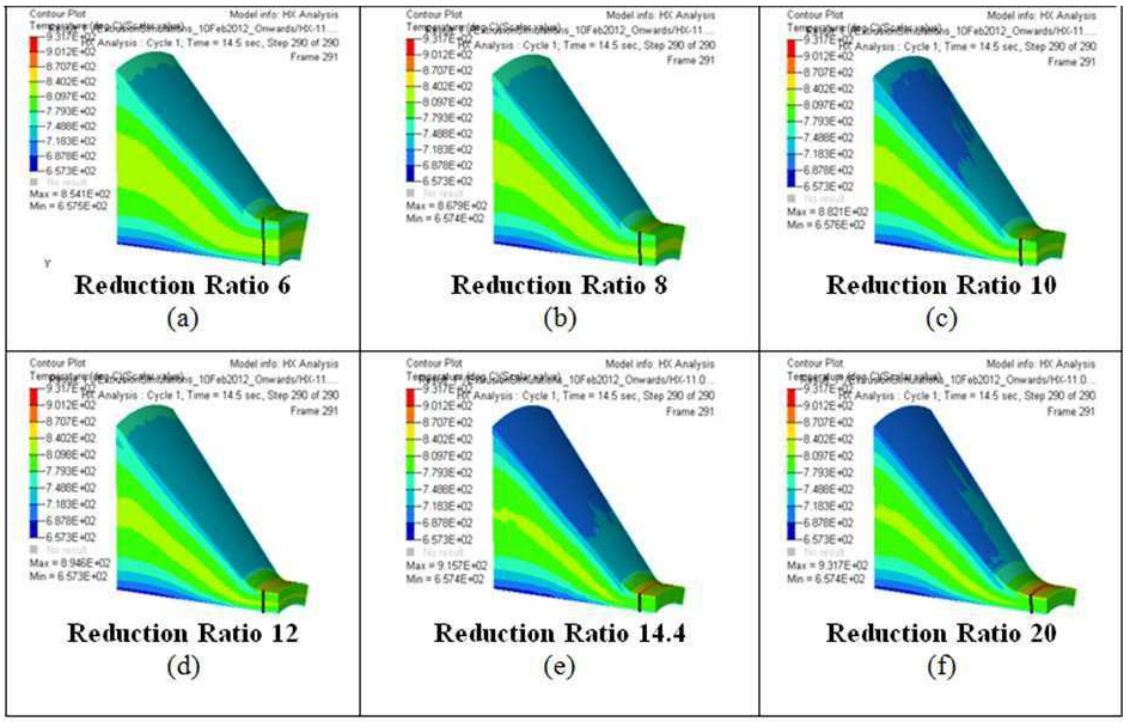

Figure 6.9: Sequence of extrudate profiles for reduction ratios of (a) 6, (b) 8, (c) 10, (d) 12, (e) 14.4 and (f) 20.

Figure 6. 10 (a) shows that there is a drop in temperature (from the preheat temperature of 815°C) near the mandrel, whereas near the fillet region, there is a sharp

rise. The flow velocity of the work piece near the mandrel remains axial throughout the length of the die cavity. On the other hand, the velocity near the die surface experiences a sudden change near the fillet region. Such sudden velocity change translates into high strain rate and corresponding rise in temperature. Thus, an inherent heterogeneity exists in the extrudate cross section. However, the undesirable effects of such a temperature profile can be alleviated if the temperature gradients are smooth and not steep. As shown in figure 6. 10, larger reduction ratios generate very steep temperature gradients across the cross section (ID to OD). Such steep gradients can be precursors to high residual stresses, which may lead to surface cracks. In the domain of present study, it is seen that lower reduction ratios are desirable on account of lower temperature gradients (figure 6. 11).

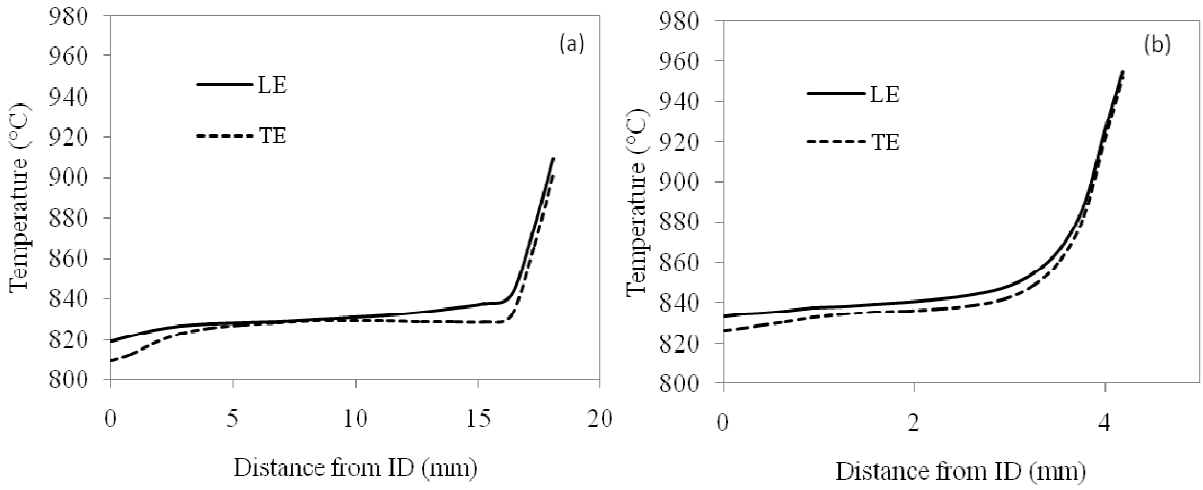

atios of (a) 6 and (b) 20.

6.4.3. Effect of preheat temperature

Figure 6. 12 shows ram force variation with ram stroke or displacement, for preheat temperatures ranging from 755 to 855°C at intervals of 10°C. Increasing the pre-heat or soaking temperature lead to a decrease in the required ram force as expected. A closer observation of the temperature profiles across a given region, shown in figure 6. 13, reveal that, a given increase in the preheat temperature will not result in same amount of increase in the peak temperature attained in that region. For example, a change of 60°C in preheat temperature (between case of 795°C to a case of 855°C) resulted in the peak temperature to increase by an amount of 40°C. This translates into lower temperature variations across a given cross section, a beneficial effect in terms of achieving microstructural homogeneity. This benefit is in combination with the advantage of reduced ram force requirement. Thus present analysis indicates that using higher pre heat temperatures within the temperature domain considered is beneficial for overall

homogeneity across cross section of the extrudate.

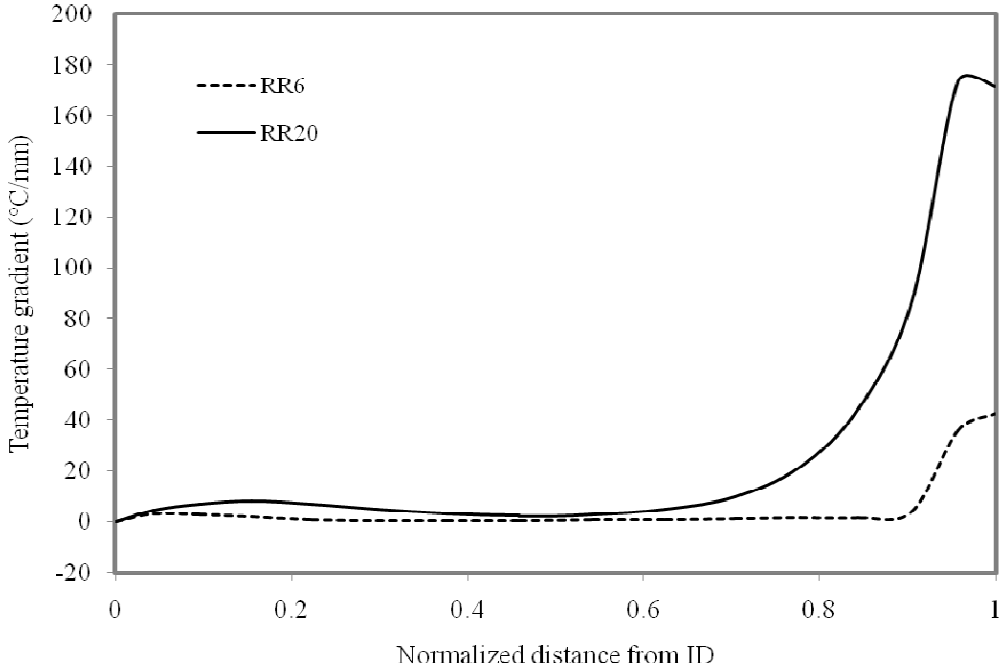

Figure 6.11: The temperature gradient profiles for Reduction Ratios of (a) 6 and (b) 20.

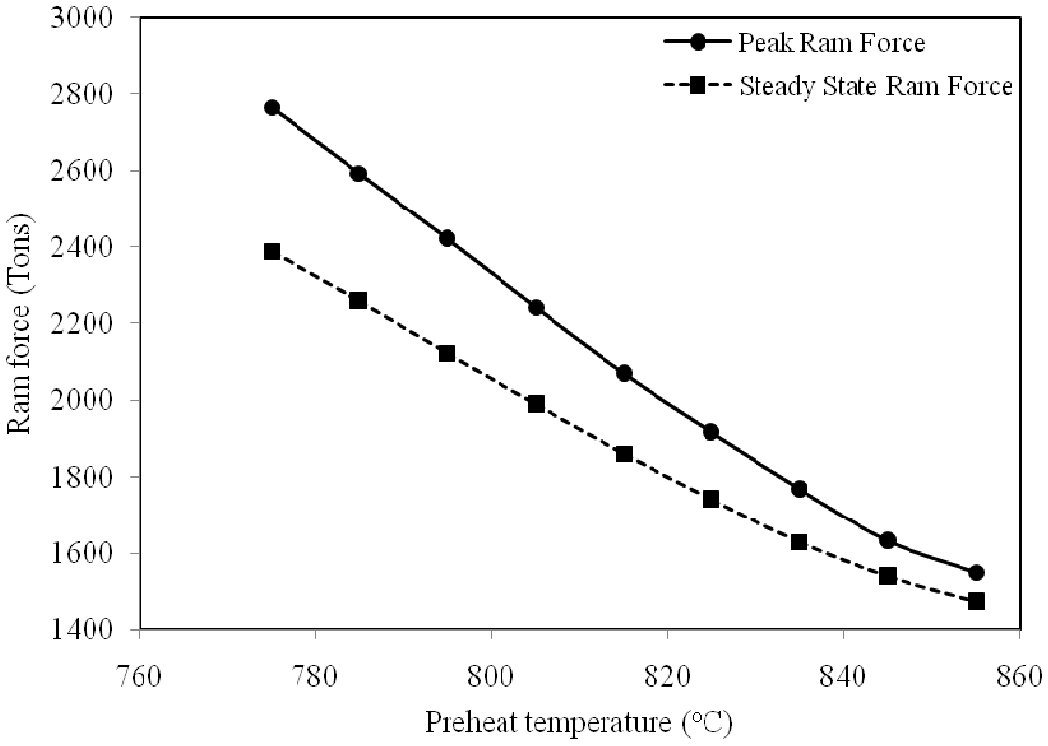

Figure 6.12: Ram force variation for different values of preheat temperatures.

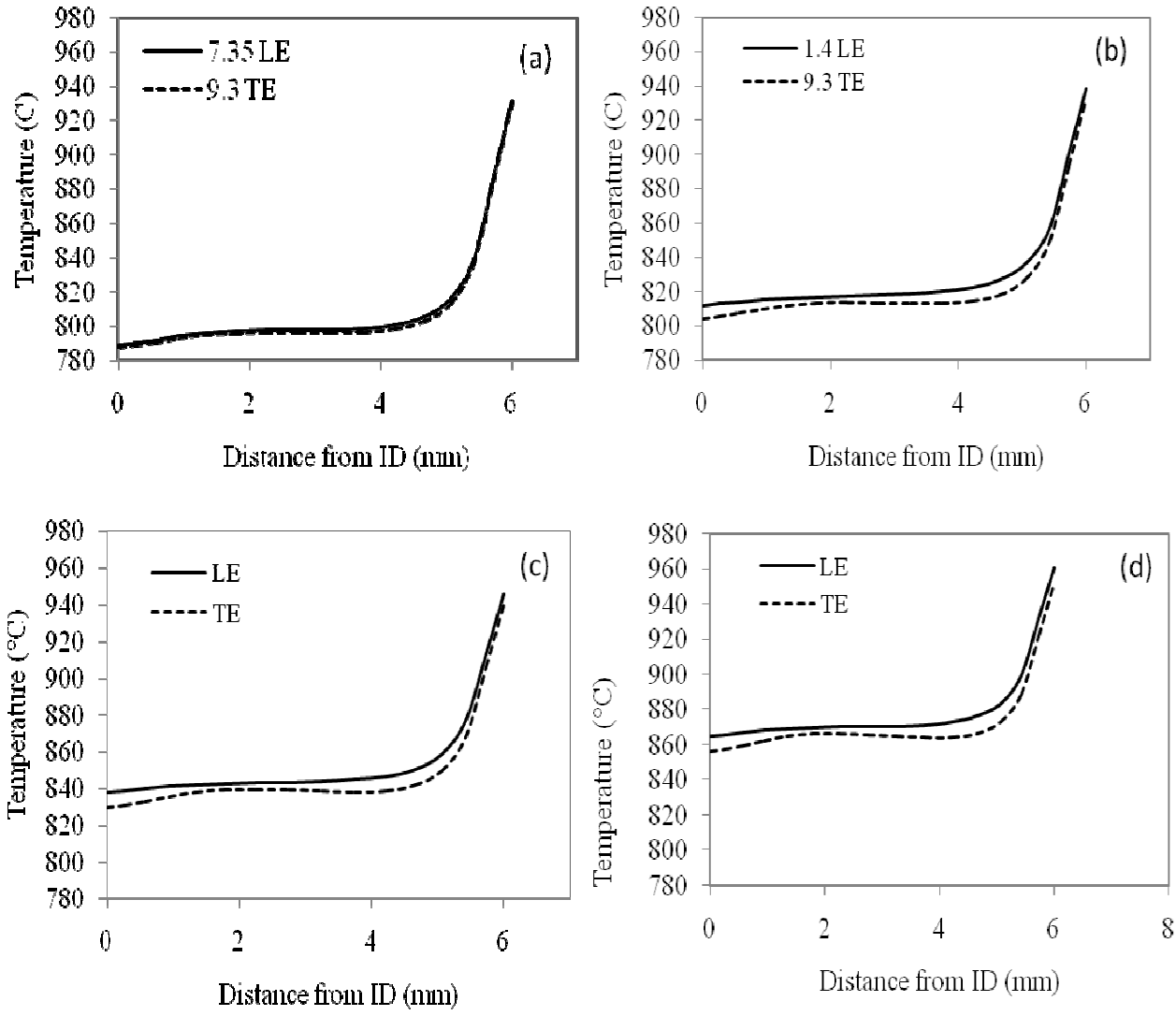

temperatures of (a) 785°C,

Effect of variation in fillet radius

Fillets are introduced in the die to soften steep flow velocity gradients. That is, fillets are expected to lower strain rates, which are generated due to sharp or sudden changes in material flow direction in any setup. These ensure a streamlined flow of material and prevent damage to dies / flow channels. Also, these ensure homogeneity in the finished product by virtue of uniform filling up of dies. Hence, a systematic variation in fillet radii was simulated to capture the effect of changing the fillet radii on the extrusion process. As fillet radius was increased, the ram force required increased (see figure 6. 14). This is seen as elevation in the ram force profile curves for larger radius of fillet. Although, increased ram force was observed for the increase in the fillet radii, the changes in the temperature profiles with the changing fillet radii are seen to be confined to the surface near to fillet. In other words, increasing fillet radius led to a temperature rise in the region directly in

contact with the die (fillet) while the temperature near the mandrel remained virtually unaffected (see figure 6. 15).

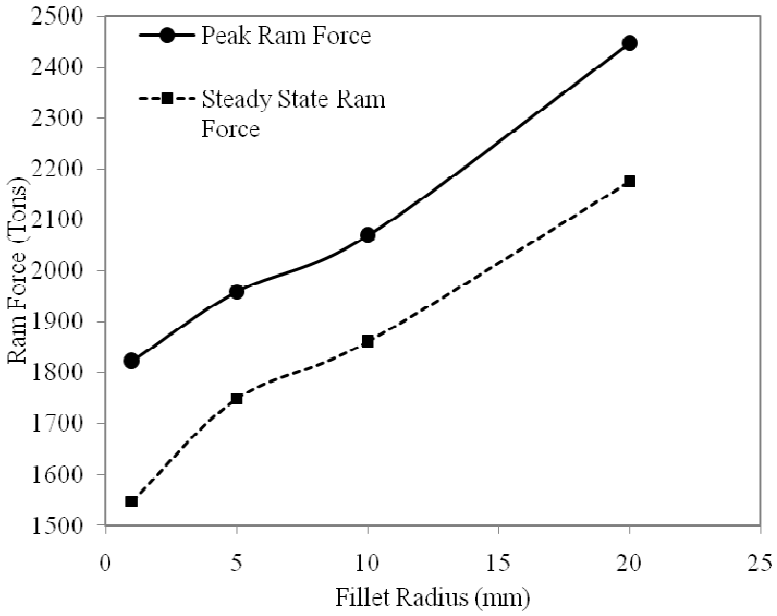

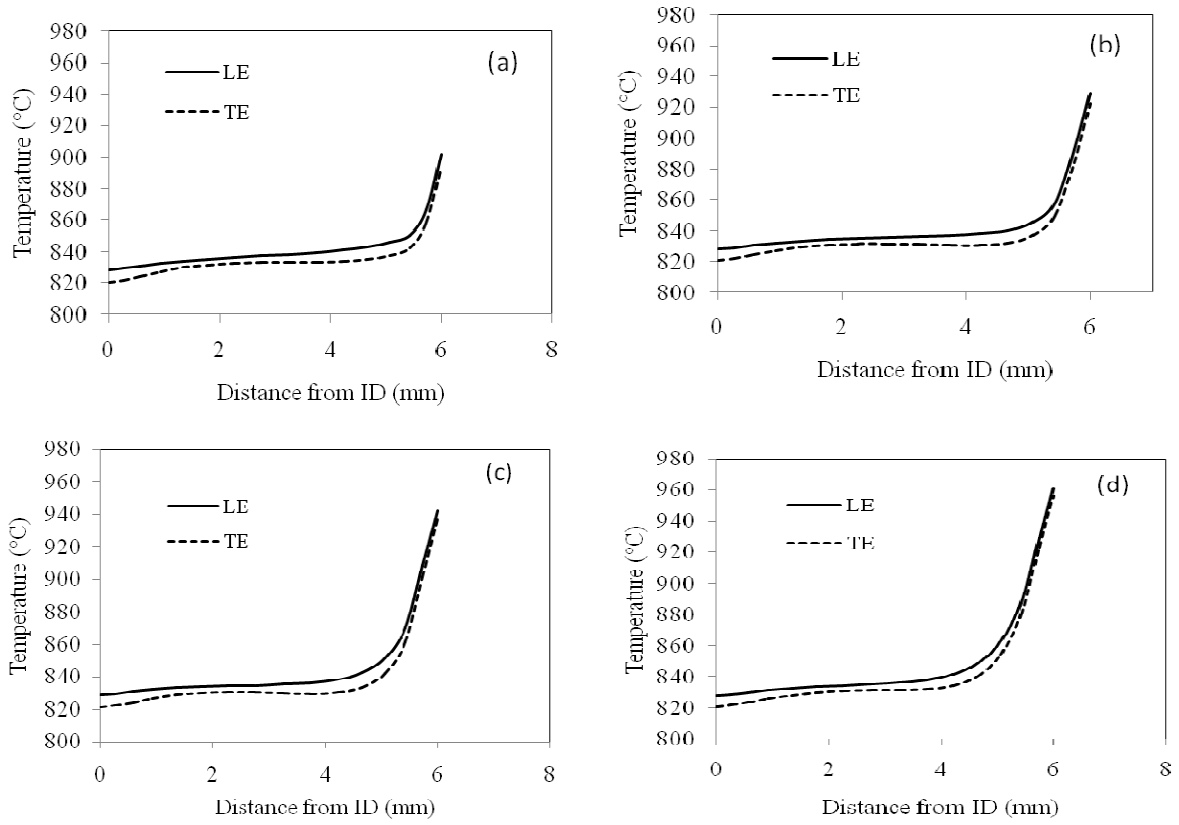

Figure 6.15: The leading (LE) and tailing end (TE) temperature profiles for fillet radii of (a) 1 mm, (b) 5 mm, (c) 15 mm and (d) 20 mm.

This significant increase in temperature near the fillet surface, can be attributed to an increase in the surface area, when the fillet radius is increased. The increased surface area leads to increased frictional drag causing localized temperature rise. Except for the rise in the temperature near the region in contact with the fillet, the temperature profile across a given cross section in the fillet region remained reasonably unaffected for all of the other fillet radii considered in the present work.

6.5. Summary

In the present work, a systematic parametric study of various extrusion parameters has been conducted using a 3-dimensional finite element analysis. The results have brought out the role of various process parameters on the zone specific temperature distributions, and overall extrusion force requirements. Analysis of temperature gradient arising out of variation in various process parameters, have thrown light on possible extent of inhomogeneity introduced during the hot extrusion process. The results of the simulation can be summarized as:

1. Lower ram velocities were found to result in appreciable temperature loss at trailing end thus giving rise to more leading end to trailing end variation while higher ram velocities were found to increase the variation across the thickness.
2. Higher reduction ratios were found to increase the temperature gradients across the thickness due to increased strain gradients at die profile side.
3. Frictional heating at the die profile was found to be more substantial than the temperature drop due to mandrel chilling effect.
4. Simulations showed that peak force of extrusion is stronger function of the ram velocity than the steady state force.
5. Simulations indicate that using of higher preheat temperature will have beneficial effect in terms of overall homogeneity.

Chapter 7

Summary

The present thesis dealt with the effect of thermo mechanical processing parameters on the evolution of microstructure, texture and mechanical properties in Zr-2.5Nb alloy, which is used as the pressure tube material in the PHWRs. The life of the pressure tube determines the life of the reactor as the replacement of the pressure tube involves large down times of the reactor in addition to huge costs. It is known that the life of this structural component is determined by its dimensional stability during service in the reactor. The detailed literature survey has shown that the dimensional stability is a function of the microstructure and texture of the component in as fabricated condition. The Zr-2.5Nb alloy is a two phase alloy and there can be variety of phase transformations product from the high temperature beta phase by controlling the beta phase composition and cooling rate. Thus, it is possible to generate a range of microstructure and texture by suitable heat treatment methods. The fabrication of the pressure tubes is quite complex and involves hot deformation (forging and extrusion), heat treatment (β quenching, annealing, autoclaving etc) and cold deformation (pilgering or drawing). In this research work, pressure tube material fabricated through two distinct routes which are generically known as cold work route and heat treated route, have been studied in detail. The influence of process parameters associated with hot deformation, heat treatments and cold deformation has been systematically studied. Unlike cold worked pressure tube, in depth understanding about the mechanisms of microstructural evolution in heat treated pressure tube during heat treatment processing steps of the materials has been studied for the first time in detail. The brief description of the main findings of the thesis are summarized below.

The cold work fabrication route for pressure tube involves three major stages of the fabrication schedule, which are expected to have significant effect on the pressure tube properties, in particular, its mechanical properties and microstructure. These effects have been studied in detail. These stages are mainly primary breakdown of the cast ingot, extrusion to tubular blank and cold work subsequent to the extrusion to achieve final dimension of the pressure tube. The results on full industrial scale (used for manufacturing 6.4m long pressure tube) have been obtained. The detailed study on evolution of microstructure, texture and mechanical properties as a function of the process parameters led to the following important inferences in the present study.

- The forging process, in particular double radial forging, resulted in more effective and uniform breakage of cast structure in comparison to the extrusion process.
- The higher extrusion ratio (followed by single pass pilgering) results in longer α grains with a higher aspect ratio and a relatively more continuous β phase along the α/α interface. The microstructure and texture are more uniform from leading end to trailing end. In addition, the higher extrusion ratio was observed to result in higher f_t and $f_t - f_r$ values.
- The intermediate annealing in the double pass pilgering route results in globulization and discontinuous beta phase and these are enriched with niobium up to 45 wt.%.
- In general, mechanical properties were very similar among all the routes that were employed in the present study.
- In general, the double radial forging based route led to a better (i) homogeneity in microstructure and texture along the entire length i.e., from the leading to the trailing end of the tube, (ii) higher aspect ratio of the alpha grain which is reported to be beneficial for diametral creep, and (iii) moreover, it led to a substantial increase in the ft and ft–fr values of the basal pole texture. These are considered beneficial modifications and hence are desirable.

The study on heat treated fabrication route for Zr-2.5 Nb pressure tubes constituted next part of the thesis. Particular emphasis has been given to the (α+β) quenching and ageing treatments. Quenching dilatometer study was performed to establish the transus temperature for the alloy used in this study. On the basis of the present studies on quenched microstructure, cold deformed and subsequent aged microstructure as a function of process parameters, optimized fabrication flowsheet to manufacture heat treated Zr-2.5 Nb alloy tube could be established. The texture and mechanical properties of the finished heat treated pressure tube and bulk texture at different stages of fabrication have been assessed in this study. The salient findings of this study on heat treated fabrication route are as follows

- The first extrusion process produces uniform structure and completely breaks the cast structure. Second extrusion produces fine (α+β) lamellar structure.

- During $\alpha+\beta$ quenching the soaking temperature determines the primary α volume fraction. Required cooling rate to obtain martensitic microstructure increases with soaking temperature.
- Ageing at 540^{o}C resulted in fine β_{Nb} precipitates of equilibrium composition, whereas the β_{Nb} phase composition did not attain the equilibrium composition after ageing at 515^{o}C.
- Mechanical properties of the finished heat treated pressure tube (aged at 515C/24h) produced with the present route were similar to the cold work pressure tube. Tube produced with 540C/24h aging exhibited substantially higher YS value at reactor operating temperature (300C)
- The bulk texture at different stages of fabrication was evaluated. The effect of quenching rate and the retained primary α volume fraction was studied. The effect of the later was found to be more dominant. Further cold working and ageing resulted in insignificant modification of texture of the pressure tube.

Hot extrusion stage is the most important step in the fabrication of the pressure tube manufacturing. This deformation step determines the microstrucre in terms of the phases present, their volume fraction, their morphology and most importantly the final texture of the tube. In the present thesis, FEM simulation of hot extrusion process has been carried to understand the role of extrusion temperature, extrusion ratio, ram velocity and profile of die on the extrusion process for obtaining desirable temperature, strain and strain rate distribution across the work piece. This FEM analysis has effectively shown quantification of the extent of differences in temperature distribution between leading and trailing end and also across a given cross section, which has implication in the final product quality. Analysis of temperature gradient arising out of variation in various process parameters, have thrown light on possible extent of inhomogeneity introduced during the hot extrusion process. The results of the simulation can be summarized as:

- Lower ram velocities were found to result in appreciable temperature loss at trailing end thus giving rise to more leading end to trailing end variation, while higher ram velocities were found to increase the variation across the thickness.
- Higher reduction ratios were found to increase the temperature gradients across the thickness due to increased strain gradients at die profile side.
- Frictional heating at the die profile was found to be more substantial than the temperature drop due to mandrel chilling effect.

- Simulations showed that peak force of extrusion is stronger function of the ram velocity than the steady state force.
- Simulations indicate that using of higher preheat temperature will have beneficial effect in terms of overall homogeneity.

References

[1] R. Krishnan, M. K. Asundi, "Zirconium alloys in nuclear technology," *Proc. Ind. Acad. Sci.* **4**, pp. 41–56, 1981.

[2] P. B. Daitch, "Reactor Physics," *Science*, **154**, pp. 1638–1638, 1966.

[3] J. A. Robertson, "The CANDU Reactor System: An Appropriate Technology.," *Science*, **199**, pp. 657–664, 1978.

[4] D. G. Cacuci, "*Handbook of Nuclear Engineering", Springer*, 2010.

[5] S. S. Bajaj and A. R. Gore, "The Indian PHWR," *Nucl. Eng. Des.*, **236**, pp. 701–722, 2006.

[6] B. Cheadle, C. Coleman, and H. Licht, "CANDU-PHWR pressure tubes: their manufacture, inspection, and properties," *Nucl. Technol*, pp. 413-425, 1982.

[7] G. Bickel and M. Griffiths, "Manufacturing variability and deformation for Zr-2.5 Nb pressure tubes," *J. Nucl. Mater*., pp. 9-13, 2008.

[8] C. Coleman, M. Griffiths, V. Grigoriev, V. Kiseliov, B. Rodchenkov, and V. Markelov, "Mechanical Properties of Zr-2.5Nb Pressure Tubes Made from Electrolytic Powder," *J. of ASTM Int*, **4**(10), 2007.

[9] T. Alam, M. K. Khan, M. Pathak, K. Ravi, R. Singh and S. K. Gupta, " A review on the clad failure studies". Nuclear Engineering and Design, 241(9), pp-3658–3677, 2011

[10] B. Cox, "Some thoughts on the mechanisms of in-reactor corrosion of zirconium alloys," *J. Nucl. Mater.,* **336**, no. 2–3, pp. 331–368, 2005.

[11] D. O. Northwood and U. Kosasih, "Hydrides and delayed hydrogen cracking in zirconium and its alloys," *Int. Met. Rev*., **28**, pp. 92–121, 1983.

[12] D. D. K. Rodgers, C. E. C. Coleman, M. Griffiths, G. Bickel, J. R. Theaker, I. Muir, A. Bahurmuz, S. St. Lawrence, M. R. Levi, and M. Resta Levi, "In-reactor performance of pressure tubes in CANDU reactors," *J. Nucl. Mater*., **383**, pp. 2–7, 2007.

[13] M. Griffiths, "A review of microstructure evolution in zirconium alloys during irradiation," *J. of Nucl. Mater.,* **159**. pp. 190–218, 1988.

[14] E. Ibrahim and R. Holt, "Anisotropy of irradiation creep and growth of zirconium alloy pressure tubes," *J. Nucl. Mater.,* pp-311-321, 1980.

[15] R. Kishore, R. "Effect of hydrogen on the creep behavior of Zr–2.5%Nb alloy at 723K", J. Nucl. Mater.,385 (3), pp-591–594, 2009.

[16] R. A. Holt, "Effect of Microstructure on Irradiation Creep And Growth Of Zircaloy Pressure Tubes In Power Reactors," *J. Nucl. Mater.*, **82**, pp. 419–429, 1979.

[17] R. J. Patel, R. Ranjon, S. Battacharyya, and G. Sharma, "Monitoring of Axial and Radial Creep of Coolant Channels in Operating PHWRs," *Procedia Eng.*, **55**, pp. 463–469, 2013.

[18] S. A. Aldridge and B. A. Cheadle, "Age hardening of Zr-2.5 wt % Nb slowly cooled from the (α +β) phase field", *J. Nucl. Mater.*,**42**, pp. 32-42, 1972.

[19] R. J. Patel, R. Ranjon, S. Battacharyya, and G. Sharma, "Monitoring of Axial and Radial Creep of Coolant Channels in Operating PHWRs". Procedia Engg., 55, pp-463–469, 2013.

[20] P. V. Sivaprasad, S. Venugopal, C. H. J. Davies and Y. V. R. K. Prasad, "Identification of optimum process parameters for hot extrusion using finite element simulation and processing maps", Modell. Simu. Mater. Sci. Engg., 12(2), 285–291, 2004.

[21] S.H. Hsiang and C.S. Liao, "Study on hot extrusion of tubes," *J. Mater. Processing Tech.*, **63**. pp. 254–259, 1997.

[22] F. Chinesta, E. Cueto, P. T. Moe, S. Stören, and H. Huetink, "Hot Metal Extrusion," *Adv. Mater. Forming*, pp. 207–223, 2007.

[23] G. Sabol, "ZIRLO — An Alloy Development Success," *J. ASTM Int.*, **2**, no. 2, p. 12942, 2005.

[24] E. Tenckhoff, "Review of Deformation Mechanisms, Texture, and Mechanical Anisotropy in Zirconium and Zirconium Base Alloys," *J. ASTM Int.*, **2**, p. 12945, 2005.

[25] K. L. Murty and I. Charit, "Texture development and anisotropic deformation of zircaloys," *Prog. Nucl. Energy*, **48**, (4), pp. 325–359, 2006.

[26] R. Haddad, and B. Cox, " On the initiation of cracks in Zircaloy tubes by I2 and Cs/Cd vapours". *J. Nucl Mater.*, **138**(1), pp-81–88., 1986..

[27] K. Kargol, J. Stevens, J. Bosma, J. Iyer, and G. Wikmark, "Modern fuel cladding in demanding operation - ZIRLO in full life high lithium PWR coolant," in *American Nucl. Soc. - 2007 LWR Fuel Performance/Top Fuel*, pp. 169–175, 2007.

[28] R. L. Tapping, "Materials performance in CANDU reactors: The first 30 years and the prognosis for life extension and new designs," *J. Nucl. Mater.,* **383**, pp. 1–8, 2008.

[29] R. A. Holt, "In-reactor deformation of cold-worked Zr–2.5 Nb pressure tubes," *J. Nucl. Mater*.,, **372** , pp. 182-214, 2008.

[30] R. G. Fleck, E. G. Price, and B. A. Cheadle, "Pressure Tube Development For Candu Reactors.," *Zirconium in the Nuclear Industry ASTM STP 824*, pp. 88–105, 1984

[31] G. Y. Chin, "Competition Among Basal, Prism, and Pyramidal Slip Modes in HCP Metals", *Metall. Mater. Trans. B*., **1,** pp. 357–361, 1970.

[32] E. Tenckhoff, "Deformation mechanisms, texture, and anisotropy in Zirconium and Zircaloy," in *ASTM STP 966* Philadelphia PA, p. 3, 1988.

[33] S. Banerjee and P. Mukhopadhyay "Phase Transformations - Examples from Titanium and Zirconium Alloys", **12**. Pergamon, 2007.

[34] K. V. M. Krishna, A. Sain, I. Samajdar, G. K. Dey, D. Srivastava, S. Neogy, R. Tewari, S. Banerjee, "Resistance to hydride formation in zirconium: An emerging possibility," *Acta Mater*., **54**, (18), pp. 4665–4675, 2006.

[35] M. Sattari, R. A. Holt, and M. R. Daymond, "Phase transformation temperatures of Zr alloy Excel," *J. Nucl. Mater*., **435**, (1–3), pp. 241–249, 2013.

[36] P. Mukherjee, P. M. G. Nambissan, P. Barat, P. Sen, S. K. Bandyopadhyay, J. K. Chakravartty, S. L. Wadekar, S. Banerjee, S. K. Chattopadhyay, S. K. Chatterjee, and M. K. Mitra, "The study of microstructural defects and mechanical properties in

proton-irradiated Zr–1.0%Nb–1.0%Sn–0.1%Fe," *J. Nucl. Mater*., **297**, no. 3, pp. 341–344, 2001.

[37] G. K. Dey and S. Banerjee, "Decomposition of the β-Phase in Zr-20%Nb," *J. Nucl. Mater*., **125** (2), pp. 219–227, 1984.

[38] C. E. Ells, "Hydride precipitates in zirconium alloys (A review)," *J. of Nucl. Mater*., **28** (2) pp. 129–151, 1968.

[39] K. Nuttall and A. J. Rogowski, "Some fractographic aspects of hydrogen-induced delayed cracking in Zr-2.5 wt% Nb alloys," *J. Nucl. Mater*., **80** (2), pp. 279–290, 1979.

[40] R. N. Singh, R. Kishore, S. K. Singh, T. K. Sinha, and B. P. Kashyap, "Stress-reorientation of hydrides and hydride embrittlement of Zr–2.5 wt% Nb pressure tube alloy," *J. Nucl. Mater*., **325** (1), pp. 26–33, 2004.

[41] R. J. McCabe, E. K. Cerreta, A. Misra, G. C. Kaschner, and C. N. Tomé, "Effects of texture, temperature and strain on the deformation modes of zirconium," *Philos. Mag*., **86**, pp. 3595–3611, 2006.

[42] E. Tenckhoff, "The development of the deformation texture in zirconium during rolling in sequential passes," *Metall. Trans*. A, **9** (10), pp. 1401–1412, 1978.

[43] R. E. Smallman, "Modern Physical Metallurgy and Materials Engineering.", Sixth Edition, *Butterworth Heinemann*, 1999

[44] G. W. Greenwood, "Modern physical metallurgy," *International Materials Reviews*, **30**, pp. 302–302, 1985.

[45] O. T. Woo, G. J. C. Carpenter, and S. R. MacEwen, "Dislocations in Zirconium Alloys," *J. Nucl. Mater*., **87** (1), pp. 70–80, 1979.

[46] J. E. Bailey, "Electron Microscope Studies of Dislocations in Deformed Zirconium," *J. Nucl. Mater*., **7** (3) pp. 300–310, 1962.

[47] J. Wang, I. J. J. Beyerlein, J. P. P. Hirth, and C. N. Tomé, "Twinning dislocations on {10-11} and {10-13} planes in hexagonal close-packed crystals," *Acta Mater*., **59** (10), pp. 3990–4001, 2011.

[48] J. Christian and S. Mahajan, "Deformation twinning," *Prog. Mater. Sci*., **39**, pp.1-157, 1995.

[49] D. G. Westlake, "Twinning in zirconium," *Acta Metall.*, **9** (4), pp. 327–331, 1961.

[50] H. Abdolvand, M. R. Daymond, and C. Mareau, "Incorporation of twinning into a crystal plasticity finite element model: Evolution of lattice strains and texture in Zircaloy-2," *Int. J. Plast*., **27** (11), pp. 1721–1738, 2011.

[51] S. K. Sahoo, V. D. Hiwarkar, I. Samajdar, and P. Pant, "Deformation twinning in zircaloy 2," *Mater. Sci.*, **702**, pp. 838-841, 2010.

[52] P. Zhao and R. A. Holt, "Microstructural Evolution and Micro-Texture in Zr-2.5Nb Tubes," *Mater. Sci. Forum*, **475–479**, pp. 1421–1424, 2005.

[53] B. A. Cheadle, C. E. Ells, and W. Evans, "The development of texture in zirconium alloy tubes," *J. Nucl. Mater*., **23** (2), pp. 199–208, 1967.

[54] H.-R. Wenk, I. Lonardelli, and D. Williams, "Texture changes in the hcp→bcc→hcp transformation of zirconium studied in situ by neutron diffraction," *Acta Mater*., **52** (7), pp. 1899–1907, 2004.

[55] V. Fidleris, “The irradiation creep and growth phenomena”, *J. Nucl. Mater,* **159**. pp. 22–42, 1988.

[56] R. A. Holt and E. Ibrahim, “Factors affecting the anisotropy of irradiation creep and growth of zirconium alloys,” *Acta Metall*., **27**, pp. 1319-1328, 1979.

[57] J. Wilkinson and T. Ben Britton, “Strains, planes, and EBSD in materials science,” *Materials Today*, **15**. pp. 366–376, 2012.

[58] F. J. Humphreys, “Characterisation of fine-scale microstructures by electron backscatter diffraction (EBSD),” *Scr. Mater.,* **51**, pp. 771–776, 2004.

[59] B. D. Cullity, Elements of X-ray Diffraction, 2nd Edn., *Addison-Wesley Publishing*, 1978.

[60] H. Stanjek and W. Häusler, “Basics of X-ray Diffraction,” *Hyperfine Interact.,* **154**, pp. 107–119, 2004.

[61] P.P. Ewald, “The Principles of X-ray Diffraction”, *Springer*, 1962.

[62] C. Hannon, “Neutron Diffraction, Instrumentation,” in *Encyclopedia of Spectroscopy and Spectrometry*, 2010, pp. 1766–1778.

[63] G. Thomas, “Transmission electron microscopy of metals”, *Wiley*, 1962.

[64] L. E. Murr, “Introduction to Conventional Transmission Electron Microscopy,” *Materials Characterization*, **51**. p. 201, 2003.

[65] K. D. Vernon-Parry, “Scanning electron microscopy: An introduction,” III-Vs Rev., **13**, pp. 40–44, 2000.

[66] P. Chapellier, R. K. Ray, and J. J. Jonas, “Prediction of transformation textures in steels,” *Acta Metall. Mater.,* **38**, (8), pp. 1475–1490, 1990.

[67] J. J . Kearns, “On the relationship among ‘f’ texture factors for the principal planes of zirconium, hafnium and titanium alloys,” *J. Nucl. Mater.,* **299** (2), pp. 171–174, 2001.

[68] J. Anderson, R. B. Thompson, and C. S. Cook, “Ultrasonic measurement of the kearns texture factors in zircaloy, zirconium, and titanium,” *Metall. Mater. Trans*. A, **30**, pp. 1981–1988, 1999.

[69] Teodoro, J. E. Rosa, L. A. A. Terremoto, A. Teixeira, G. Lucki, and M. D. A. Damy, “Comparison Of The Mechanical Properties And Corrosion Resistance Of Zirlo And Other Zirconium Alloys,” in *INAC* 2007, Santos, Brazil, pp. 1–6, 2007.

[70] M. K. Kumar, C. Vanitha, I. Samajdar, D. Srivastava and G. K. Dey, “Textural and microstructural developments during fabrication of Zr–2.5 Nb pressure tubes,” *J. Nucl. Mater*., **335** , pp. 48-58, 2004.

[71] D. Srivastava, G. Dey, and S. Banerjee, “Evolution of microstructure during fabrication of Zr-2.5 Wt pct Nb alloy pressure tubes,” *Metall. Mater. Trans*. A, **26,** pp. 2707-2718, 1995.

[72] R. Tewari, D. Srivastava, G. G. K. Dey, J. K. Chakravarty, and S. Banerjee, “Microstructural evolution in zirconium based alloys,” *J. Nucl. Mater.,* **383**, pp. 153–171, 2008.

[73] J. Haq, A. Haq, and S. Banerjee, “Effect of cold working and annealing on the texture of Zr-2.5Nb pressure tubes,” *Bull. Mater. Sci*., **15**, pp. 289-296, 1992.

[74] M. Griffiths, J. E. Winegar, and a. Buyers, “The transformation behaviour of the β-phase in Zr–2.5Nb pressure tubes,” *J. Nucl. Mater.,* **383**, pp. 28–33, 2008.

[75] B. J. S. Wilkins and K. Nuttall, “Secondary cracking in hydrided Zr-2.5 Wt% Nb alloys,” *J. Nucl. Mater.*, **75,** pp. 125–130, 1978.

[76] C. J. Simpson and C. E. Ells, “Delayed hydrogen embrittlement in Zr-2.5 wt % Nb,” *J. Nucl. Mater*., **52**, pp. 289–295, 1974.

[77] Y. S. Kim, Y. Perlovich, M. Isaenkova, S. S. Kim, and Y. M. Cheong, “Precipitation of reoriented hydrides and textural change of α-zirconium grains during delayed hydride cracking of Zr–2.5%Nb pressure tube,” *J. Nucl. Mater*., **297**, pp. 292–302, 2001.

[78] J. Gil Sevillano, P. Van Houtte and E. Aernoudt , “Large strain work hardening and textures”, *Prog. Mater. Sc.,* **25**, pp. 69–412, 1981.

[79] N. Saibaba, K. Vaibhaw, S. Neogy, K. V. Mani Krishna, S. K. Jha, C. Phani Babu and G. K. Dey, “Study of microstructure, texture and mechanical properties of Zr–2.5Nb alloy pressure tubes fabricated with different processing routes”, *J. Nucl. Mater.*, **44**0(1-3), pp. 319–331, 2013.

[80] Y. Li, R. Rogge, and R. A. Holt, “Development of local microstructure and crystallographic texture in extruded Zr–2.5Nb tubes,” *Mater. Sci. Eng*. A, **437**, pp. 10–20, 2006.

[81] R. A. Holt and P. Zhao, “Micro-texture of extruded Zr–2.5Nb tubes,” *J. Nucl. Mater*., **335**, pp. 520–528, 2004.

[82] S. S. Kim, S. C. Kwon, and Y. Suk Kim, “The effect of texture variation on delayed hydride cracking behavior of Zr–2.5%Nb plate,” *J. Nucl. Mater.*, **273**, pp. 52–59, 1999.

[83] M. Shahzad and L. Wagner, “Influence of extrusion parameters on microstructure and texture developments, and their effects on mechanical properties of the magnesium alloy AZ80,” *Mater. Sci. Eng.* A, **506**, pp. 141–147, 2009.

[84] J. Zhou, L. Li, and J. Duszczyk, “3D FEM simulation of the whole cycle of aluminium extrusion throughout the transient state and the steady state using the updated Lagrangian approach,” *J. Mater. Process. Technol.*, **134**, pp. 383–397, 2003.

[85] L. Li, J. Zhou, and J. Duszczyk, “Prediction of temperature evolution during the extrusion of 7075 aluminium alloy at various ram speeds by means of 3D FEM simulation,” *J. Mater. Process. Technol.,* **145**, pp. 360–370, 2004.

[86] Z. He, H. N. Wang, M. J. Wang, and G. Y. Li, “Simulation of extrusion process of complicated aluminium profile and die trial,” *Trans. Nonferrous Met. Soc*. China (English Ed., **22**, pp. 1732–1737, 2012.

[87] F. J. Zanner and L. A. Bertram, “Vacuum arc remelting: An overview,” in *NASA STI/Recon Technical Report* N, 1985, **86**, p. 16417.

[88] R. L. Boxman, D. M. Sanders, and P. J. Martin, “Handbook of vacuum arc science and technology: fundamentals and applications”, 1995.

[89] G. Scott and C. M. Scala, “A review of non-destructive testing of composite materials,” *NDT International*, **15**. pp. 75–86, 1982.

[90] G. Ngaile and T. Altan, “Simulation of Manufacturing Processes: Past, Present and Future” , *Proc. 7th ICTP, Yokohama*, Japan, 2002, p.271.

[91] P. Goodhew, F. Humphreys, and R. Beanland, “Electron microscopy and analysis,” *Taylor & Francis*, 2001.

[92] M. Suryanarayana and M. Grant Norton, "X-Ray Diffraction: A Practical Approach". *New York: Plenum Press*. pp-68-281 2001.

[93] H. Abe and M. Furugen, "Method of evaluating workability in cold pilgering," *J. Mater. Process. Technol.*, 212, pp. 1687–1693, 2012.

[94] D. Northwood and W. Fong, "Modification of the structure of cold-worked Zr-2.5 wt% Nb nuclear reactor pressure tube material," *Metallography*, **13**(2), 1980.

[95] H. Gegel, J. Malas, S. Doraivelu, and V. Shende, "Modeling techniques used in forging process design," *ASM Handbook*, **14**, p.425, 1988.

[96] M. De Graef, "Introduction to Conventional Transmission Electron Microscopy". Cambridge: *The Press Syndicate of the University of Cambridge*. pp.1-544, 2003.

[97] J. Chen, K. Chandrashekhara, C. Mahimkar, S. N. Lekakh, and V. L. Richards, "Study of void closure in hot radial forging process using 3D nonlinear finite element analysis," *The Intl. J. Adv. Manuf.Tech.*, 62, pp. 1001–1011, 2012.

[98] B. Verlinden, J. Driver, I. Samajdar, and R. Doherty, "Thermo-mechanical processing of metallic materials". *Oxford: Elsevier*. pp.1-491, 2007.

[99] S. Coryell, "Flow Behavior and Microstructural Evolution of INCOLOY 945 During High Temperature Deformation." Field report, Dept. of Met. and Mater. Engg., Colorado School of Mines, Golden CO.

[100] C. Hunt and P. Niessen, "The continuous cooling transformation behaviour of zirconium-niobium-oxygen alloys," *J. Nucl. Mater.*, 38(1), pp. 17-25, 1971.

[101] D. Srivastava, G. K. Dey, and S. Banerjee, "Evolution of Microstructure during Fabrication of Zr-2.5 Wt pct Nb Alloy Pressure Tubes," *Metall. Trans. A*, 26, pp. 2707–2718, 1995.

[102] T. Konishi, M. Honji, D. Franklin, and R. Adamson, "Zirconium in the Nuclear Industry: Sixth International Symposium," *ASTM STP 824*, 1984.

[103] K. V. M. Krishna, P. Tripathi, V. D. D. Hiwarkar, P. Pant, I. Samajdar, D. Srivastava, and G. K. Dey, "Automated reconstruction of pre-transformation microstructures in zirconium," *Scr. Mater.*, **62**(6), pp. 391–394, 2010.

[104] R. A. Holt and S. A. Aldridge, "Effect of extrusion variables on Crystallographic Texture of alloy for CANDU pressure tubes," *J. Nucl. Mater.*, **135**, pp. 246–259, 1985.

[105] J. Kearns and C. Woods, "Effect of texture, grain size, and cold work on the precipitation of oriented hydrides in Zircaloy tubing and plate," *J. Nucl. Mater.*, **20**(3), pp. 241-261, 1966.

[106] R. Ballinger, G. Lucas, and R. Pelloux, "The effect of plastic strain on the evolution of crystallographic texture in Zircaloy-2," *J. Nucl. Mater.*, **126**(1), pp. 53-69, 1984.

[107] L. Li, J. Zhou, and J. Duszczyk, "Determination of a constitutive relationship for AZ31B magnesium alloy and validation through comparison between simulated and real extrusion," *J. Mater. Process. Technol.*, **172**(3), pp. 372–380, 2006.

[108] M. Malpani and S. Kumar, "A feature based analysis of tube extrusion," *J. Mater. Process. Technol.*, **190**(1-3), pp. 363–374, 2007.

[109] K. V.M. Krishna, S. K. Sahoo, I. Samajdar, S. Neogy, R. Tewari, D. Srivastava, G. K. K. Dey, G. H. Das, N. Saibaba and S. Banerjee, "Microstructural and textural

developments during Zircaloy-4 fuel tube fabrication," *J. Nucl. Mater.*, **383**(1-2), pp. 78–85, 2008.

[110] D. Y. Yang and K. J. Kim, "Design of processes and products through simulation of three-dimensional extrusion," *J. Mater. Process. Technol.*, **191**(1-3), pp. 2–6, 2007.

[111] N. Bontcheva, G. Petzov, and L. Parashkevova, "Thermomechanical modelling of hot extrusion of Al-alloys, followed by cooling on the press," *Comput. Mater. Sci.*, **38**(1), pp. 83–89, 2006.

[112] C. M. Lee and D. Y. Yang, "Three-dimensional steady-state finite element analysis of square die extrusion by using automatic mesh generation," *Int. J. Mach. Tools Manuf.*, **40**(1), pp. 33–47, 2000.

[113] W. Xianghong, Z. Guoqun, L. Yiguo, and M. Xinwu, "Numerical simulation and die structure optimization of an aluminum rectangular hollow pipe extrusion process," *Mater. Sci. Eng. A*, **435**–**436**, pp. 266–274, 2006.

[114] C. Zhang, G. Zhao, Z. Chen, H. Chen, and F. Kou, "Effect of extrusion stem speed on extrusion process for a hollow aluminum profile," *Mater. Sci. Eng. B*, **177**(19), pp. 1691–1697, 2012.

[115] L. X. Li, K. P. Rao, Y. Lou, and D. S. Peng, "Hot deformation characteristics of Ti-6Al-4V," *Zeitschrift Fur Met.*, **94**(9), pp. 1006–1011, 2003.

[116] R. Y. Lapovok, M. R. Barnett, and C. H. J. Davies, "Construction of extrusion limit diagram for AZ31 magnesium alloy by FE simulation," *J. Mater. Process. Technol.*,**146**(3), pp. 408–414, 2004.

[117] H.J. McQueen, M. Myshlaev, M. Sauerborn, M. Mwembela, Flow stress, microstructures and modeling in hot extrusion of magnesium alloys, in: H.I. Kaplan, J. Hryn, B. Clow (Eds.), *Proc. Mag. Tech.*, The Mineral, Metals & Materials Society, pp. 355–362, 2000.